POLITECNICO DI TORINO

Collegio di Ingegneria Civile

Corso di Laurea Magistrale in Ingegneria Civile Geotecnica

Tesi di Laurea Magistrale

Shape effects in the dynamical response of flints/boulders during pile driving

Relatori:

Prof. Guido Musso

Dr. Emilio Nicolini

Candidato:

Ivan Terribile

Luglio 2019

Abstract

In the last decade, offshore wind industry has grown exponentially, especially in Europe where is installed more than 80% of the total power of the active offshore wind turbines.

In order to bring cost of wind power to a competitive level, dimension and capacity of the new wind turbines are increasing over the year, leading the foundations designers to new engineering challenges. In the offshore environment about 20% of the total cost of a wind turbine is represented by the foundation, which today is largely constituted by large diameter piles often larger than 6m.

The need to reduce the foundation cost and increase the pile diameter led to the installation of piles with an increasing diameter to pile wall thickness over the year. This expose in some case the pile toe to be damaged during the installation phase, due the impact with a boulder, widely encountered in glacial tills, or flint bands frequently found in chalk deposits, causing premature refusal.

This problem is becoming more and more a concern in the offshore industry and represents a very complex engineering challenge, due to the interaction of several elements.

Essentially, the problem can be divided in two main phenomena:

- the pile tip buckling;
- the dynamical behaviour of embedded flint/boulder.

This thesis is part of a wider research project, where the whole phenomena is numerically investigated. In particular, in this thesis the following of a previous numerical study of the static and dynamic reaction offered by a flint to the pile tip is presented. The work is mainly aimed to the exploration of the effect of the shape of the flint/boulder, taking into account the possibility of a non-centered impact between the pile toe and the encountered nodule element.

Contents

List of figures

List of symbols

Roman letters

A cross-sectional area of pile

C damping matrix

$\mathbf{C_1}$, $\mathbf{C_2}$ relaxation factor viscous boundaries

c wave speed in pile

D pile diameter

$\mathbf{D_R}$ damping value

d flint diameter – horizontal axis

E pile Young's modulus

$\mathbf{E_{oed}}$ oedometric modulus

$\mathbf{E_u}$ undrained elastic stiffness modulus

F force

f frequency

f normalized force

G shear modulus of soil

$\mathbf{I_e}$ target element dimension

IP index of plasticity

J damping factor

K stiffness matrix

$\mathbf{k_c}$ pile circular stiffness

k equivalent spring stiffness

L cylindrical flint length

l pile length

$\mathbf{M}$ mass matrix

$\mathbf{N_b}$ ball penetrometer factor

$\boldsymbol{N_c}$ T-bar factor

$\mathbf{N_{lim}}$ normal limit force

$\boldsymbol{n}$ porosity

$\boldsymbol{Q}$ quake

$\mathbf{r_c}$ relative element size

$\mathbf{R_{inter}}$ interface strength reduction factor

$\mathbf{R}$ flint radius

$\mathbf{R_s}$ static soil resistance

$\mathbf{R_t}$ total soil resistance

$\mathbf{S_u}$ undrained shear strength

$\mathbf{T_{lim}}$ tangential limit force

$\mathbf{t}$ pile thickness

UCS unconfined compressive strength

$\mathbf{u}$ displacement

$\dot{\mathbf{u}}$ velocity

$\ddot{\mathbf{u}}$ acceleration

$\mathbf{u_x}$ horizontal displacement

$\mathbf{u_y}$ vertical displacement

$|\mathbf{u}|$ total displacement

$\mathbf{V_p}$ P-wave velocity

$\mathbf{V_s}$ S-wave velocity

$\mathbf{x}$ normalized displacement

$\boldsymbol{Z}$ pile impedance=EA/c

Greek letters

$\boldsymbol{\alpha_N, \beta_N}$ Newmark coefficients

$\boldsymbol{\alpha_R, \beta_R}$ Rayleigh coefficients

$\boldsymbol{\gamma_{dry}}$ dry unit weight

$\boldsymbol{\gamma_{sat}}$ saturated unit weight

$\boldsymbol{\gamma_w}$ water unit weight

$\boldsymbol{\nu}$ Poisson's ratio

$\boldsymbol{\nu_u}$ undrained Poisson's ratio

$\boldsymbol{\rho}$ density

$\boldsymbol{\sigma_t}$ tensile strength

$\boldsymbol{\sigma_y}$ pile yield stress

1. Introduction

1.1. Scope and motivation

The long-term energy strategy set by the European Union foresees a reduction of 80%-95% of the 1990 gas emission levels by 2050. The achievement of this goal implies a radical change in the current European energetic system, highlighting the need for relevant investments in new low-carbon technologies and renewable energies. In this transitional period, wind energy plays a key role in the expansion of the renewable energies worldwide.

The significant development of onshore wind energy in the last decades, however, was held back by land-use and by the need for a reduction of noise and visual pollution, laying the groundwork for a greater growth of the offshore wind industry.

In particular, in Europe over the last decade, offshore wind has grown exponentially (Figure 1) moving from being a niche market to the largest low-carbon energy source, potentially capable of providing in the 2030 up to 25% of the European Union electrical total demand (BVG).

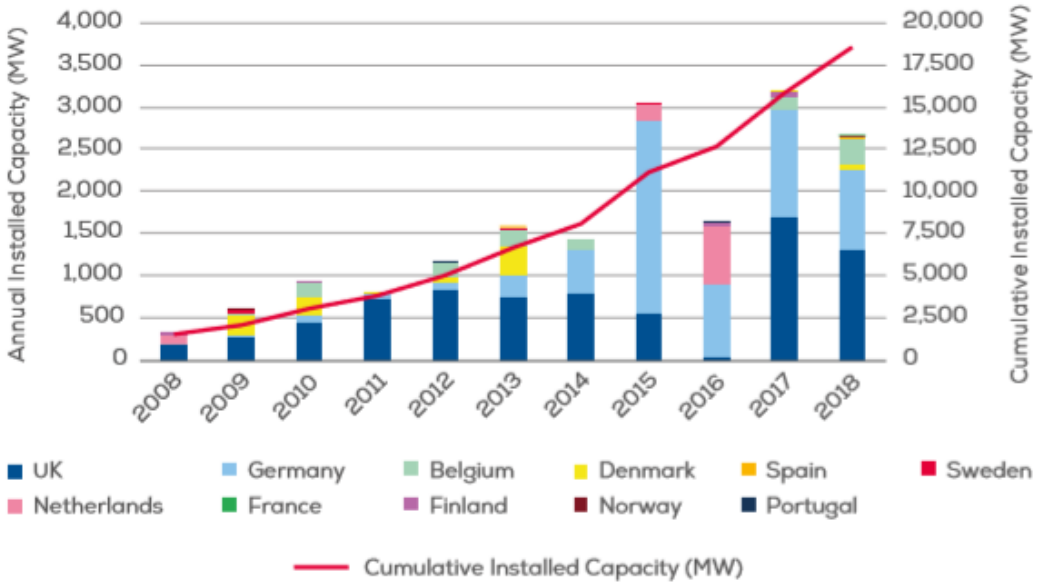

Figure 1 - Annual offshore wind installations and cumulative capacity (Wind Europe, 2019)

According to 4C Offshore (4C Offshore, 2018), in 2018 Europe provides 80% of the world installed capacity, with a total number of 4543 wind turbines connected and a cumulative capacity of 18.5 GW.

Due to the wind resources and the shallow water conditions, 70% of all offshore wind capacity in Europe is provided by wind turbines installed in the North Sea, followed by the Irish Sea with 16%, the Baltic Sea with 12% and the Atlantic Ocean with 2% (Wind Europe, 2019).

Despite the recent development, the offshore wind energy prices appears to be nearly twice as onshore wind power (Jiang, et al., 2017), pointing out the need for further technological advances in order to bring the cost of wind power to a competitive level. This has led over the years to a constant increase in dimension and capacity of the new wind turbines. At this time, the largest turbine in the world, installed in 2018 in the MHI Vestas Offshore Windfarm in United Kingdom, has a diameter of 164m and a capacity of 8.8MW.

However, the installation in offshore environment of turbines of such dimensions and the need to develop appropriate foundation systems, represents an engineering challenge.

In addition, it is necessary to consider that unlike the oil&gas industry where the foundations cost is modest with respect to the cost of the construction of the whole platform, the foundation of offshore wind turbines represents the 25% to 30% of the total cost (Snyder & Kaiser, 2008).

Consequently, the study and the development of economic and reliable foundations, represents a key point of research.

Among the different types of foundations used, monopiles are the most popular substructures, covering 81.5% of the total foundations installed in Europe. Monopiles diameters are today often larger than 6m, with 8m diameter piles becoming not so rare. With the need to reduce foundation costs and in parallel to increase its dimension to ensure adequate resistance, the diameter to pile wall thickness is increasing considerably, exposing in some cases the pile to be damaged during the installation phase.

A common risk faced during installation operations of this kind of foundations is the pile tip damage due to a boulder impact during pile driving in glacial tills. A similar problem can be identified during pile driving in chalk, where bands of flints are often encountered. In this case, the installation trend is to install piles with the so-called drive-drill procedure,

which requires the pile tip to be undamaged during the installation by driving, to allow the drilling tool to pass, clean the flint/boulder layer , and finally allow the continuation of driving without further damages.

Such events are becoming more and more a concern in the industry and represent a complex engineering issue which can be divided essentially in two main parts: the pile tip buckling and the dynamic behavior of the flint.

The main aim of this thesis is to explore the dynamic behavior of the flint/boulder, mainly focusing on the effects produced by dimension and shape, with the main objective of finding a relationship between the pile advancement and the potential pile tip damage.

1.2. Aim and objectives

This work presents a numerical study of the dynamical behaviour of flints embedded in chalk. Finite element analyses have been carried out with the objective of describing the response of the flint to the impact with the pile during pile driving. In particular, the reacting forces exerted by the flint to its displacement within the soil have been evaluated. The main aim of this work is to evaluate a relationship between the forces which arise at the pile-flint contact point and the vertical displacement (i.e. pile advancement) in order to provide an assessment of a limit penetration rate during pile driving, able to prevent potential pile tip damage where layers of flints are expected.

1.3. Structure of the document

The present work consists of the following main sections covering the basic topics of this Ms thesis.

Chapter 2 presents a literature review of the geological context in which the investigated phenomenon is frequently faced. In particular, chalk and flints are described in terms of characteristic, formation and distribution in the North Sea. Finally, an assessment of the engineering properties to be used in the numerical analyses is provided.

Chapter 3 contains a briefly description of the foundation structures commonly adopted to support offshore wind turbines.

Chapter 4 introduces the installation methods in offshore environment, focusing mainly on pile impact driving. In the same chapter, a literary review of the pile-boulder interaction and pile tip buckling phenomenon is presented.

Chapter 5 offers a detailed description of the performed 2D finite element analyses. Three different flint shapes have been investigated in plane strain conditions, by imposing a vertical displacement to the flint in different positions. Results have been obtained in terms of horizontal and vertical forces needed to produce a plastic displacement of the flint within the chalk.

Chapter 6 presents the results of the 2D dynamical finite element analyses performed with the aim of modelling the impact between the pile and the flint during pile driving. A dynamic load, obtained through a driveability analysis, has been applied to the flint, in order to evaluate a relationship between the resulting force at the contact point and the permanent vertical displacement. Finally, a safe driveability assessment is proposed.

Chapter 7 summarizes the findings of this study and suggests further developments of the present research.

2. Geological context

Chalk is a variety of limestone composed mainly of calcium carbonate, formed during the Late Cretaceous (145.5 million to 65.5 million years ago) in marine environment. Chalk deposits are often marked by the presence of flints, a siliceous cryptocrystalline rock which can occur as individual nodules or layers of masses. Flints are normally strong and highly abrasive, in contrast to the very weak embedding chalk. Due to the large distribution of chalk deposits in Europe, especially between the Thames and Paris basins, flints have been often intercepted during engineering projects, representing a relevant construction risk.

2.1. Chalk

2.1.1. Definition and engineering classification

Chalk is a sedimentary carbonate rock, characterized by soft friable material with a fine texture and high porosity, which make it different from the ordinary limestone. Its distinctive white colour is due to its mineral composition, mainly dominated up to 95% by calcite, a ionic salt called calcium carbonate, $CaCO_3$. In some cases, Chalk can be locally rich of different minerals such as glauconite and clay, which give to the material respectively a greyish or greenish colour.

According to CIRIA publication (Lord, et al., 2002), the old division of Upper, Middle and Lower chalk, should no longer be used. Over the years, several new markers have been used to define new and very precise biostratigraphy, in which chalk fossil play a significant role (Mortimore, 2010).

In chalk classification a big role is played also by flints. Flints bands and their geometrical characteristics have been used to define boundaries between the different formations by recognizing the stratigraphical sequence of different types of flint in field exposure.

From the engineering point of view, the effect of weathering represents a fundamental aspect in chalk classification. Chalk deposits may occur in different forms depending on the spacing and aperture of discontinuities, from a compact unit to a highly fractured condition. Usually, at shallow depths chalk is reduced to a structureless melange by the action of weathering (Lake, 1975).

Physical properties, particularly density and porosity, have been used to classify chalk as an engineering material. However, density is still the simplest way to characterize the intact material (Mortimore & Duperret, 2004). At present, according to CIRIA classification (Lord, et al., 2002), which represents the chalk classification system most widely adopted, the following factors are used to classify chalk for engineering purposes:

- intact dry density;
- discontinuity spacing and aperture.

Dry density represents the most easily measured property of chalk indicative of its mass behavior. A first distinction is made based on this parameter, subdividing chalk in four main categories, as reported in Figure 2.

Density scale	Intact dry density γ_d (Mg/m³)	Porosity n*	Saturation moisture content*
Low density	< 1.55	> 0.43	> 27.5%
Medium density	1.55–1.70	0.43–0.37	27.5–21.8%
High density	1.70–1.95	0.37–0.28	21.8–14.3%
Very high density	> 1.95	< 0.28	< 14.3%

* Based on the specific gravity of calcite $G_s = 2.70$ (see Section 4.2)

Figure 2 - Intact dry density scale of chalk (Lord, et al., 2002)

Chalk is then further separated in four grades based on typical discontinuity aperture (Figure 3). Chalk can be Structureless (Grade D), if reduced to a remoulded mélange by weathering, or Structured (Grade A, B and C) whose grade is characterized by the aperture of discontinuities.

Grade A	Discontinuities closed
Grade B	Typical discontinuity aperture < 3 mm
Grade C	Typical discontinuity aperture > 3 mm
Grade D	Structureless or remoulded mélange.

Figure 3 - Chalk classification by discontinuity aperture (Lord, et al., 2002)

Structured material may then be subdivided by adding a numerical suffix according to the discontinuity spacing (Figure 4).

Suffix	Typical discontinuity spacing
1	$t > 600$ mm
2	$200 < t < 600$ mm
3	$60 < t < 200$ mm
4	$20 < t < 60$ mm
5	$t < 20$ mm

Figure 4 - Subdivision of Structured Chalk by discontinuity spacing

Regarding the Structureless chalk, a further subdivision is usually made based on the engineering behavior (Figure 5), by adding the suffix “m” when the material behaves as a cohesive soil or the suffix “c” when the presence of clasts is dominating.

Suffix	Engineering behaviour	Dominant element	Comminuted chalk matrix	Coarser fragments
m	fine soil	matrix	approx > 35%	approx < 65%
c	coarse soil	clasts	approx < 35%	approx > 65%

Figure 5 - Subdivision of Structureless Chalk by engineering behavior

2.1.2. Distribution of chalk in Europe

Chalks deposits are presents in many parts of the world, including Europe (from Ireland to Russia), USA and Australia, within Mesozoic, Tertiary and Quaternary Systems.

In Europe, chalk is a conspicuous sediment across the European Platform north of the Alpine deformation front and within the Syrian Arc of the Afro-Arabian Platform (Mortimore, 2011). Focusing on North-West Europe, extensive chalk deposits occur across the North Sea, from south Sweden to England, whose characteristics are basically similar and different from the other European chalk, characterized by various secondary processes.

In England, chalk is traditionally divided in two main provinces (Figure 6), the Northern and Southern provinces, separated by an area of transitional succession (Mortimore & Wood, 1983), which presents some characters of both provinces and some unique features.

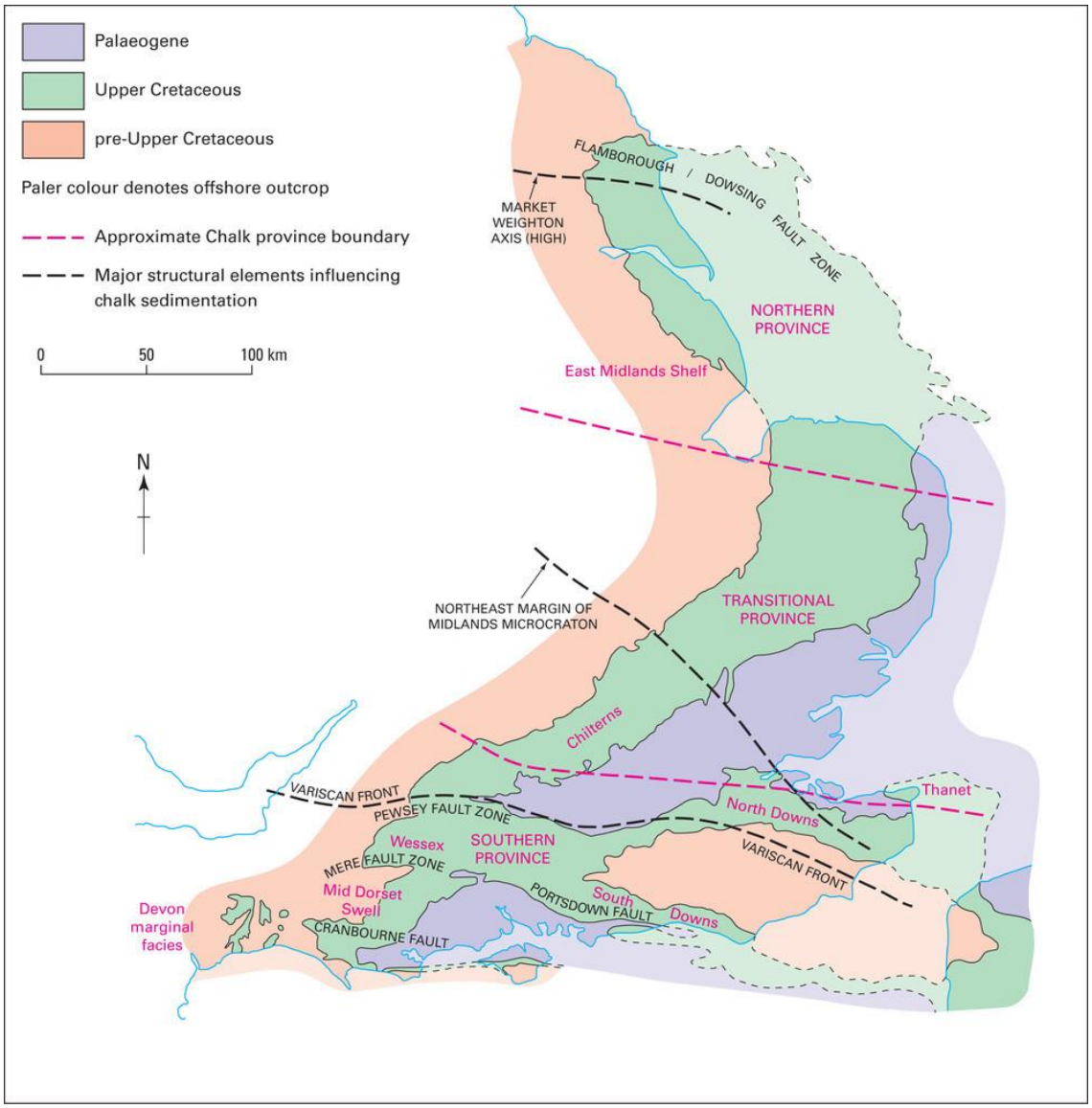

Figure 6 – Chalk group provinces in England (www.bgs.ac.uk)

The Northern Province involves the regions of Yorkshire, Lincolnshire, Humberside and the north Norfolk, while the Southern Province is located across the Anglo-Paris Basin.

In the Northern Province chalk is very consistent, hard and well-bedded, probably due to a deeper water origin with respect to the Southern Province Chalk (Mortimore, et al., 2001) which is characterized by a softer Chalk frequently interrupted by very large channel scouring.

Each major province is further divided in subgroups, based on numerous markers beds like flints, marl seams and fossils. Focusing on the White Chalk Subgroup, it is divided

into four formations in the Northern Province and seven formations in the Southern Province, due to the presence of more varied sediments (Figure 7).

Northern Province

Sub-group	Formation	Local informal names	Key references
White Chalk	Rowe Chalk		Wood and Smith (1978)
	Flamborough Chalk	Flamborough Sponge Bed	Whitham (1991, 1993)
	Burnham Chalk		**Key BGS memoirs**
	Welton Chalk		Hull and Brigg (1994)
Grey Chalk	Ferriby Chalk	Black Band, Nettleton Stone, Totternhoe Stone, Red Chalk or Hunstanton Red Rock	Grimsby and Patrington (1994)

Transitional Province

Sub-group	Formation	Local informal names	Key references
White Chalk	Norwich Chalk (informal)	Paramoudra Chalk, Beeston Chalk, Catton Sponge Bed, Weybourne Chalk, Pre-Weybourne Chalk, Basal mucronata Chalk	Peake and Hancock (1961, 1970)
	Portsdown Chalk		Ward *et al* (1968)
	Culver Chalk		Mortimore and Wood (1986)
	Newhaven Chalk		Wood (1988)
	Seaford Chalk		**Key BGS memoirs**
	Lewes Nodular Chalk		Leighton Buzzard (1994)
	New Pit Chalk	Brandon Flints	Norwich (1989)
	Holywell Nodular Chalk	Melbourn Rock, Plenus Marls	Hitchin (1955)
Grey Chalk	Zig Zag Chalk	Grey Chalk, Chalk Marl, Nettleton Stone, Totternhoe Stone, Glauconitic Marl, Cambridge Greensand	King's Lynn and The Wash (1994)
	West Melbury Marly Chalk		Great Yarmouth (1994)

Southern (or Anglo-Paris Basin) Province

Sub-group	Formation	Local informal names	Key references
White Chalk	Portsdown Chalk		Bristow *et al* (1997)
	Culver Chalk	Spetisbury Chalk Member, Tarrant Chalk Member	Mortimore (1986, 1997)
	Newhaven Chalk		Mortimore and Pomerol (1987)
	Seaford Chalk		**Key BGS memoirs**
	Lewes Nodular Chalk	Chalk Rock	Lewes (1987)
	New Pit Chalk	Melbourn Rock, Plenus Marls	Brighton and Worthing (1988)
	Holywell Nodular Chalk		Shaftesbury (1995)
Grey Chalk	Zig Zag Chalk	White Bed/Falling Sands Member JB Bed 7	
	West Melbury Marly Chalk	Glauconitic Marl	

Figure 7 - British Chalk mapping units (Lord, et al., 2002)

2.1.3. Formation

During the Late Cretaceous Epoch, between 65 and 100 million years ago, the separation of the supercontinents Laurasia and Gondwanaland led the oceans to reach depths never experienced before. This new geological contest, characterized by deep waters, high temperatures and a reduced level of oxygen in the water, created the environment conditions for chalk deposits formation.

Chalk is formed by millions submicroscopic algae, known as Coccolithophores, bloomed on the ocean's surface. This type of algae is characterized by a spherical skeleton, called Cocosphere, formed by calcareous discs, known as Coccoliths (Figure 8). When these organisms die, their skeletons accumulate on the ocean floor. Once deposited on the seabed, millions of these elements formed a lime mud, progressively subjected to pressure and heat by further sedimentation. This geological process, called lithification, removes water and compacts the sediments, transforming the lime mud into rock. Over the years, the depth at which chalk formed has been object of discussion. Absence of fragments of land-derived or volcanic rock and of some algae suggest that chalk is not a shallow water deposit (Mortimore, 2010). It is now agreed that chalk of the North Europe formed between 100m and 500m.

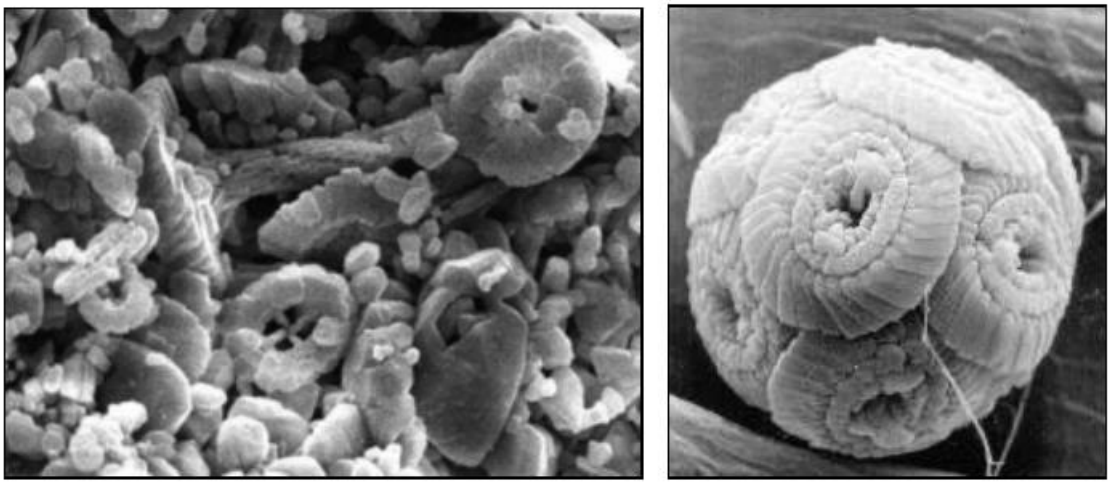

Figure 8 - Chalk coccoliths (www.discoveringfossils.co.uk)

2.1.4. Properties

Over the years, the physical properties of chalk have been used to classify chalk and provide an index of potential mechanical behavior. In particular dry density, being easy to evaluate and slightly sensitive to the measuring methods.

Mechanical behavior of chalk results related to the hydraulic environment. Especially its degree of saturation largely affects its mechanical and chemical behavior, making its response varied. If its composition preserves mainly the same characteristics, great deviations can be observed in terms of porosity. As a result, moisture content in chalk can vary from values bigger than the liquid limit to very low values, characteristic of a limestone.

Tests carried out by Mortimore (Mortimore & Duperret, 2004) on dry and saturated samples, show a good correlation between the intact dry density (IDD) and the uniaxial compressive strength (UCS). By observing the difference between dry and saturated sample, it is possible to notice how saturation produce a reduction of the strength, up to 50%.

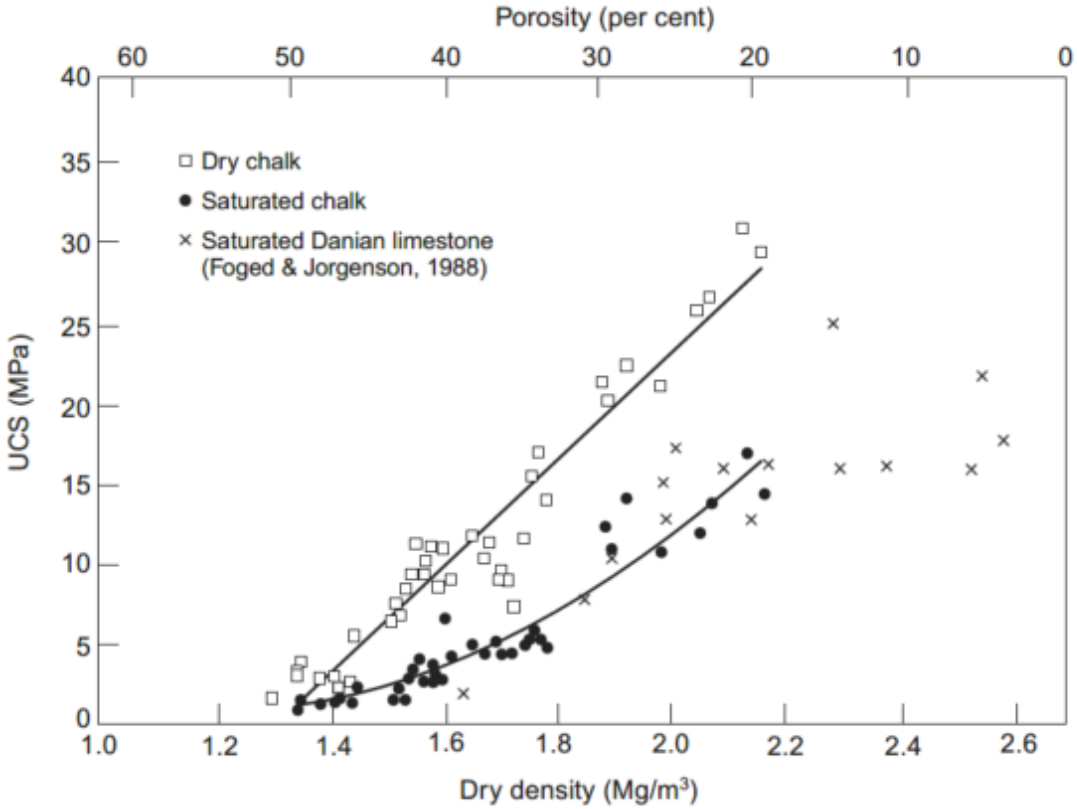

Figure 9 - Relationship between the intact dry density and the uniaxial compressive strength

Figure 10 shows the results of tests conducted by Lord et al. (Lord, et al., 2002). The high variability in the physical is reflected in the variability of the strength. However, it has to be considered that chalk of different grade (§2.1.1) have been tested, and this wide range of results is due not only to the different porosity and density, but it is also the result of different degree of fracturation and weathering.

Regarding the structureless material, investigations carried out by Puig (Puig, 1973) have revealed that the mechanical behavior of the sample is dominated by the puttified material when the it occupies more than 15% of the whole weight.

Property		Units	Range
Dry density	γ_d	Mg/m³	1.29–2.46
Porosity	n*	%	9–52
Voids ratio	e*	—	0.10–1.10
Saturated moisture content	m_{sat}	%	4–40†
Calcium carbonate content		%	55–99
Specific gravity	G_s	—	2.69–2.71
Liquid limit	w_L	%	18–53
Plasticity index	I_p	%	4–30
Liquidity index		—	-2.25–+2.50
Point load index	$I_{s(50)}$	MPa	0.01–1.15
Unconfined compressive strength⁺	q_u	MPa	0.7–40
Slake durability index	I_{d2}	%	13–96

* calculated from dry density assuming $G_s = 2.70$

† wet

Figure 10 - Typical range of index properties for Chalk

The undrained resistance of the structureless chalk is drastically reduced with increasing values of the moisture content, but with respect of clay, a pure undrained resistance results complex to be achieved. This material shows an increase in compressive strength with increases in confinement pressure, mainly due to the difficulty in obtaining a complete saturation of the sample. When a load is applied to a partially saturated sample characterized by a very high porosity, pore water migrates within the sample and the material densifies, resulting in a resistance increment. The pure undrained condition is achieved only once the material is completely saturated.

In literature, only values of undrained resistance obtained from laboratory tests conducted on structured material are reported. The main reason is related to the difficulty in encountering puttified chalk for onshore engineering works. Only with the increase of the offshore sector the behavior of the structureless chalk has been widely investigated.

During a recent project carried out in Cathie Associates, the mechanical behavior of this material has been fully investigated. Isotropically consolidated undrained triaxial tests lead to a resistance of about 100 kPa for a structureless material characterized by high porosity and dry density between 1.4 to 1.6 Mg/m^3.

This result appears in line with the range suggested by Lake (Lake, 1975) of 70kPa to 100 kPa, based on conducted on very weak natural chalk.

An evaluation of the undrained resistance of the structured chalk can be made by using the plot previously presented in Figure 9. For a low-density chalk, a UCS value of about 2 MPa can be considered. This value lead to an undrained resistance of 1 MPa which results in line with internal experience in Cathie Associates.

Regarding the soil unit weight, it is possible to evaluate it by using the following relationship (Lancellotta, 2012):

$$\gamma_{sat} = \gamma_{dry} + n\gamma_w \qquad \text{Equation 1}$$

By assuming a value of 15kN/m^3 for the dry unit weight and a porosity equal to 40%, a saturated unit weight of about 19 kN/m^3 is obtained.

Concerning the deformability parameters of the material, Matthews and Clayton (Matthews & Clayton, 1993) investigated a relationship between the elastic modulus and the porosity. The elastic modulus varies from 25 GPa for a low-porosity chalk (30%) to 5 GPa.

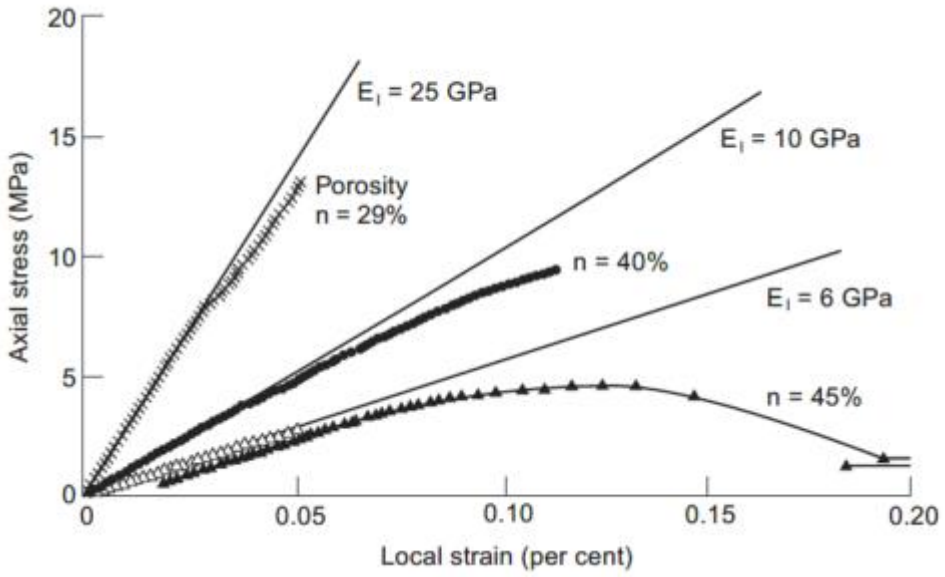

Figure 11 - Stress-strain curves from UCS tests

However, the presented results are related to tests conducted on structured chalk samples. For a structureless material, a ratio of E_u/S_u=1000, leading to an elastic modulus of about 1 MPa.

2.2. Flints

2.2.1. Definition

One of the most famous features of White Chalk in Europe is the presence of layers of black flints (Figure 12). Since the prehistoric age, men have used the hardness and durability of the flints to build various tools, like arrows for hunting or cutting tools. Only afterwards flints properties as a construction material have been recognize, leading to a large use of this material for road, wall and building.

Due to the large presence flints had interact with several engineering projects over the years. Being very stiff with respect to the embedding chalk and highly abrasive, flints represent a significant construction risk in the geotechnical environment, especially in drilling and excavation operations.

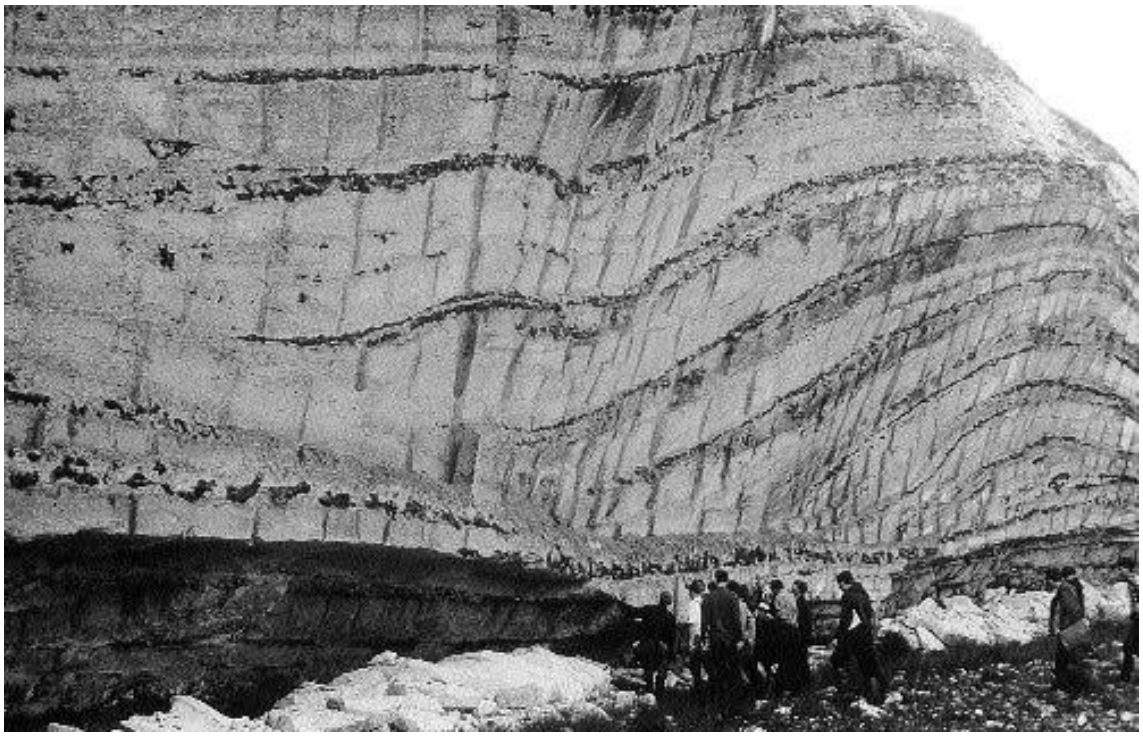

Figure 12 - Regular Flint bands on Chalk cliff (Lord, et al., 2002)

In contrast with chalk, flint is a high strength, fine graded, cryptocrystalline rock formed in chalk deposit. It consists mainly of silica, (87%-99%), with a reduced content of calcite and clayey minerals (Lawrence & Collier, 2017). Flints are not characterized by a specific color. The most common flints are dark grey with shades of different color, like brown or red. Color is typically subordinate to the presence of various metal oxides and hydroxides. Usually occurring in bands, flints are characterized by irregular shapes,

mainly describable as nodular (Figure 13), tabular o tubular. The shape can usually provide an idea of the permeability grade of the forming chalk deposit. Nodular flints reflect a high variability of the embedding chalk. Tabular masses, widely found in the Northen Province, have formed in high permeability chalk deposits. Regarding the rhythmic formation of layers of flint, it is the reflection of climatic change, causing variation in concentration of organic matter and pauses in sedimentation (Lord, et al., 2002).

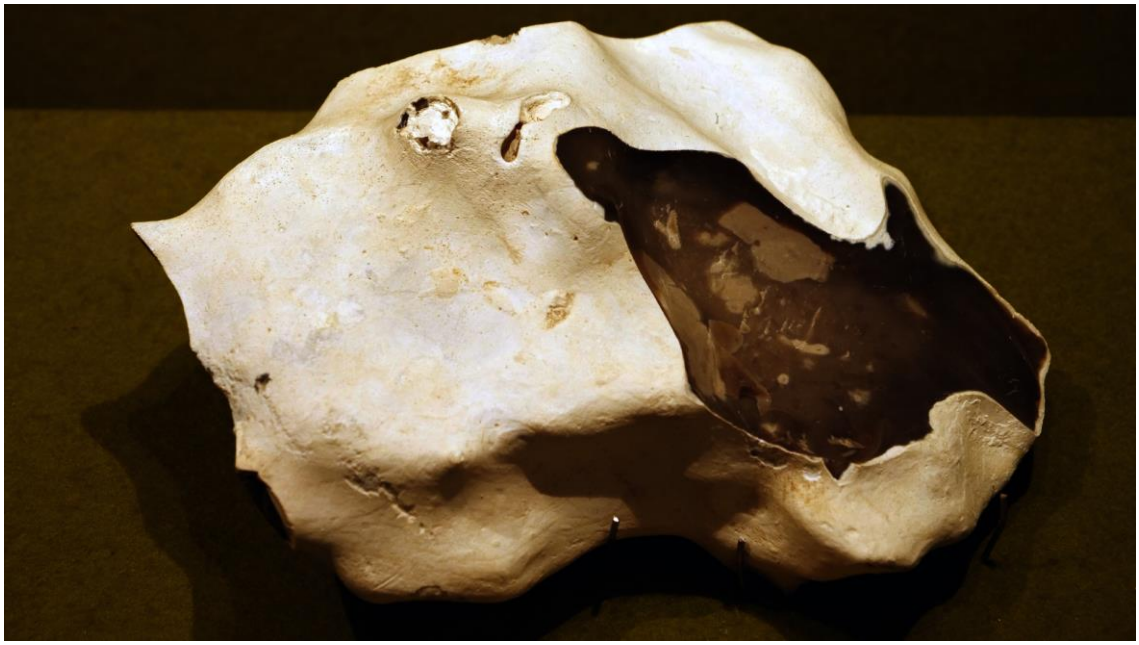

Figure 13 - Nodular flint (www.worthingmusemu.com)

2.2.2. Localization

Since the first classification of chalk, flints have been used as a lithological marker, because of the variability of their features and the stratigraphic distribution in the numerous regions characterized by the presence of chalk deposits.

In Europe, flints can widely be observed in the Cretaceous Chalk of the emerging outcrop of the Baltic Sea and the English Channel.

Mortimore (Mortimore & Wood, 1986) observed huge discrepancy in the flint distribution over the two main chalk provinces. A stratigraphical distribution of the flint in the main two provinces is presented in Figure 14.

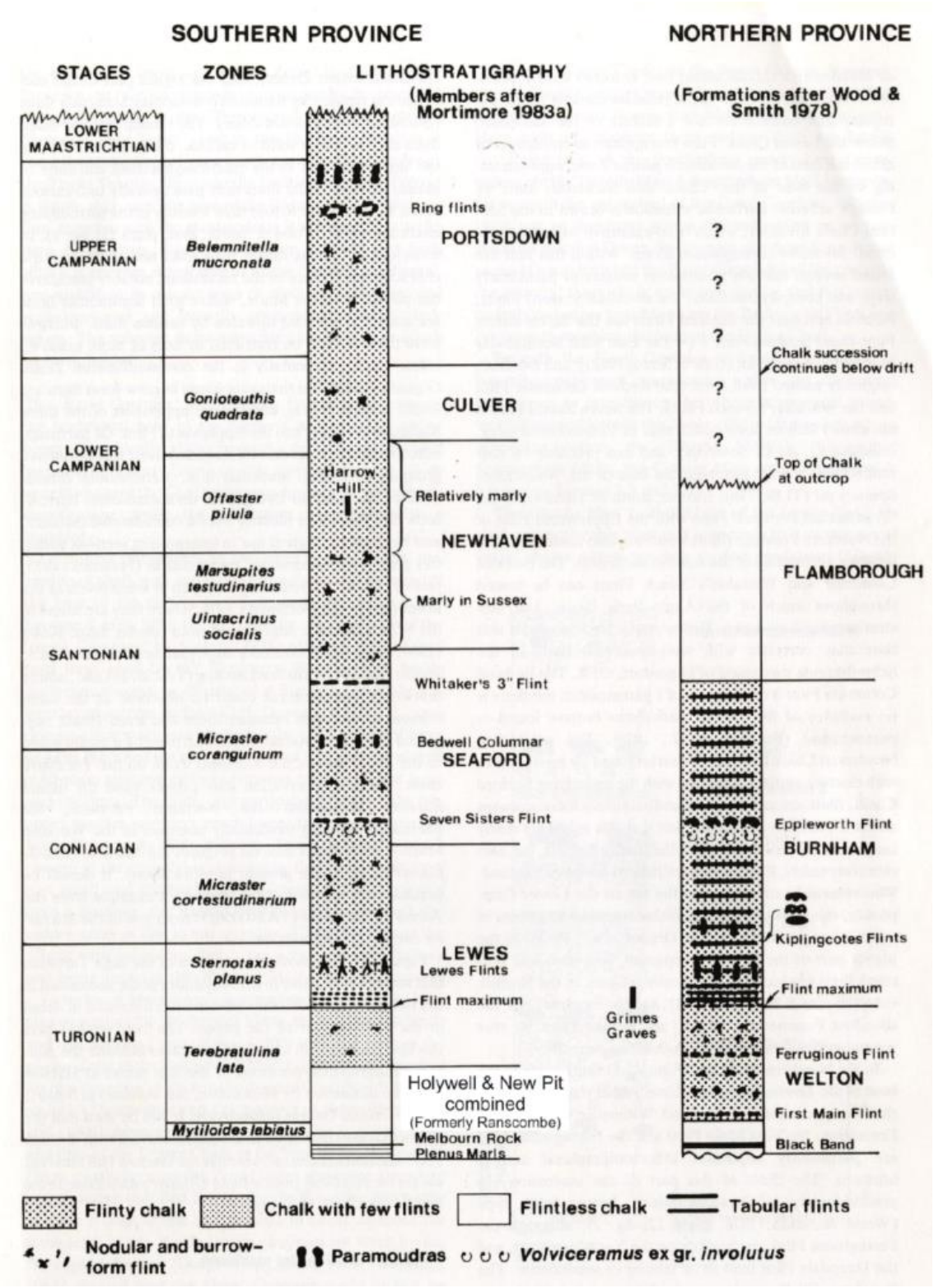

Figure 14 - Distribution of flint in the English Chalk (Mortimore & Wood, 1986)

Northern Province is mainly characterized by the presence of grey flints with a tabular shape. Same features are not encountered in the Southern Province, where flints are generally black, characterized by a burrow-form. It is important to highlight that the

Northern Province chalk visible at outcrops is flintless, in marked contrast with the Southern Province whose chalk presents bands of flints clearly identifiable.

2.2.3. Formation

Flints formed soon after the sedimentation of chalk, from the deposition of some organisms, like sponges, radiolaria/diatoms, characterized by the presence of biogenic silica in their own skeleton. Once the organic material dissolute, silica reach the seabed dissolving in the chalk lime mud. Within the chalk deposit, the decomposition of organic material produces hydrogene sulphide. These particles migrate upward and at a certain depth, less than 10m depth, meet the oxygen released by the above water column, producing a chemical reaction. This acidic condition dissolves carbonate and silica precipitates, replacing chalk grain by grain. Silica change is state over the time. Initially in the form of crystalline opal, it is progressively transformed in quartz with the increase of time and of the overburden.

Figure 15 - Echinoids preserved as flint (www.discoveringfossils.co.uk)

Within flint nodules a wide range of marine fossils can be found. Sometimes the chemical reaction took place directly within the shell, due to the presence inside it of high permeable chalk. In this case flints preserved the shape of the original organism (Figure 15).

Different stratigraphic distribution of flints in the European Chalk is directly associated to the geological history of the deposits. Generally, sedimentation areas characterized by greater water depth result less reach in flint presence. This is probably due to the reduced oxygen concentration of the water, which prevents the chemical reaction (silica precipitate).

2.2.4. Properties

The large presence of flint band has a strong influence in chalk modes of failure. However, for the purpose of this work is more interesting explore the strength and deformability of flints as single elements. In contrast to the embedding weak chalk, flint is a very strong and brittle material. Flint has a "conchoidal" fracture mode, like rock crystal or glass, but with fracture surface more regular, less curved with very sharp edges.

There is only limited information on the strength of flint. One of the early measured results of the flint strength have been published by Lautridou et al. (Lautridou, 1986), who suggest a UCS strength of 391 MPa and a Brazilian tensile strength of 68 MPa.

Test made by Cumming (Cumming, 1999), on nodular and sheet flints, show no direct correlation between Point Load Strength (Is 50) and the uniaxial compressive strength (UCS). Point load test does not appear as a reliable strength indicator.

Recent studies have been carried on by Lawrence and Collier (Lawrence & Collier, 2017), whose results are presented in Figure 16.

Several mechanical tests have been performed, in order to evaluate the relationship between the mechanical properties and the morphology and microtexture of flints of three different regions. In general, the obtained results show that engineering properties varies with flint class and no size effects has been reported. A good correlation has been found between flint and UCS. Flints of the Northern Province are characterized by a significantly low density with respect to the flints from the south of England and France. This suggests a different degree of silicification.

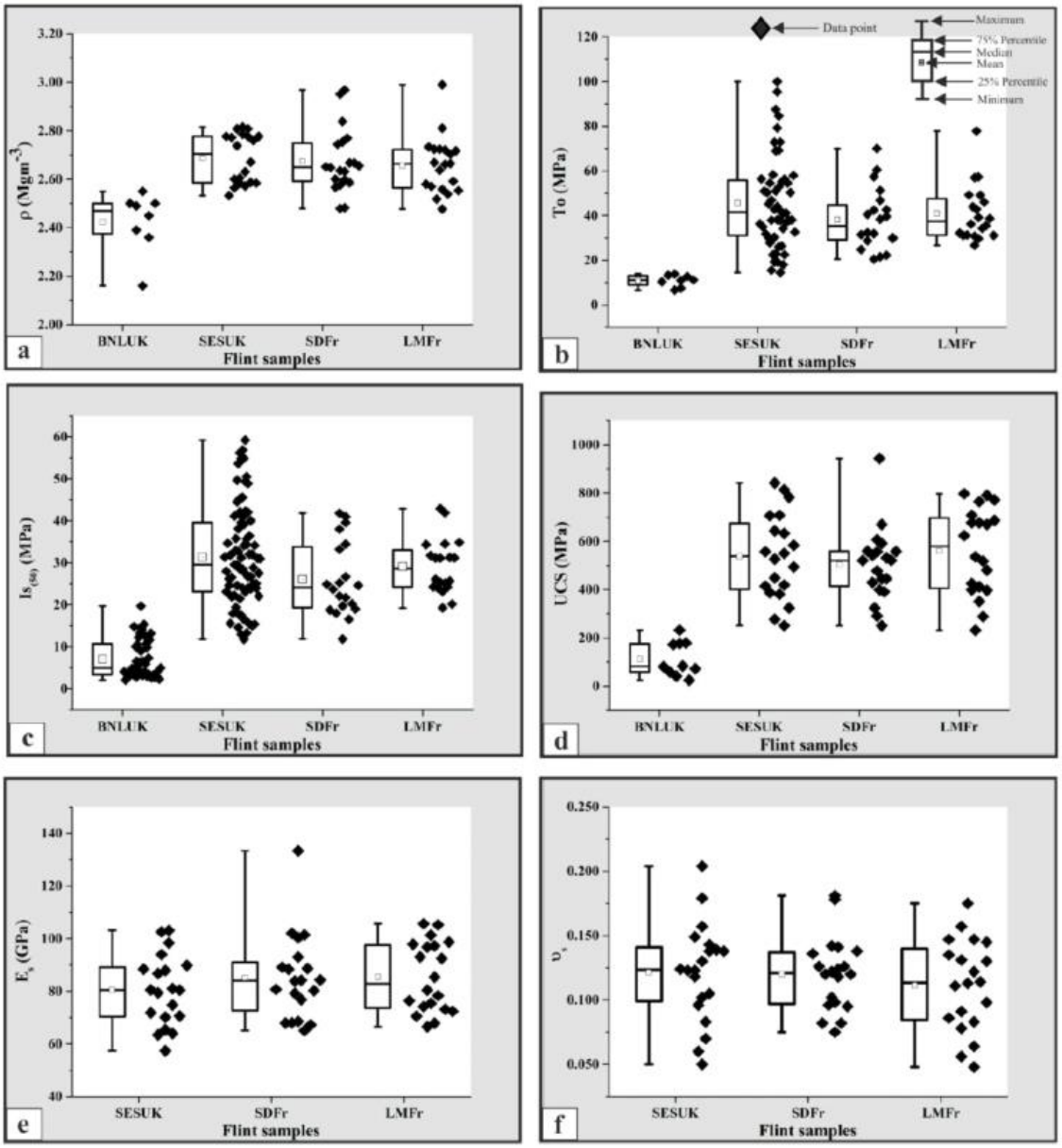

Figure 16 - Flints density and strength and deformability tests results

Considering the high-density flints of the Southern Province, the average values reported in Table 1 can be assumed as representative of the mechanical behavior of flints.

Table 1 – Assumed flint properties

ρ [Mg/m^3]	UCS [MPa]	σ_t [MPa]	E_s [GPa]	ν [-]
2.65	500	40	80	0.125

3. Offshore foundations

3.1. Offshore foundations

3.1.1. Introduction

An offshore wind turbine can be considered mainly composed by three elements:

- the tower, a metallic pipe with a diameter between 4m and 6m;
- the turbine, placed on top of the tower;
- the blades, connected to the turbine.

In the offshore environment to the previous elements must be added the transition piece and the substructure. The transition piece connects the substructure to the tower and provides correction for potentially misalignment. The substructure maintains the whole structure in the operational position.

Therefore, the main difference between the different types of offshore wind turbines is in the way these structures are supported and bound to the seabed.

Offshore foundation substructures can be divided in:

- fixed foundations,
- gravity foundations;
- floating foundation systems.

Their selection and use are related to the water depth of the installation site (Figure 17). Gravity and fixed foundations are mostly used for water depths up to 60m. Fixed foundations have been installed at higher depths for the oil&gas industry, however they are not economically convenient for offshore wind structures. For deeper depths, floating systems have started to be developed.

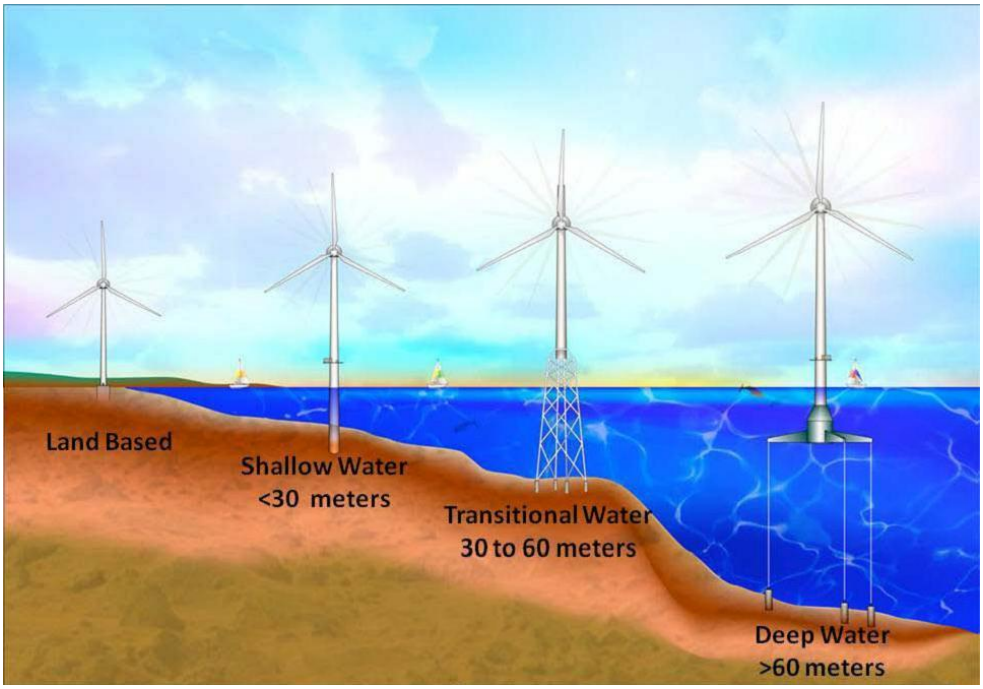

Figure 17 - Offshore wind turbine substructures

Due to the shallow water depth, as reported by Wind Europe (Wind Europe, 2019), installation of offshore wind turbine in Europe is at the moment dominated by fixed foundations, with monopiles representing about 80% of the total number of installed offshore wind turbine (Figure 18).

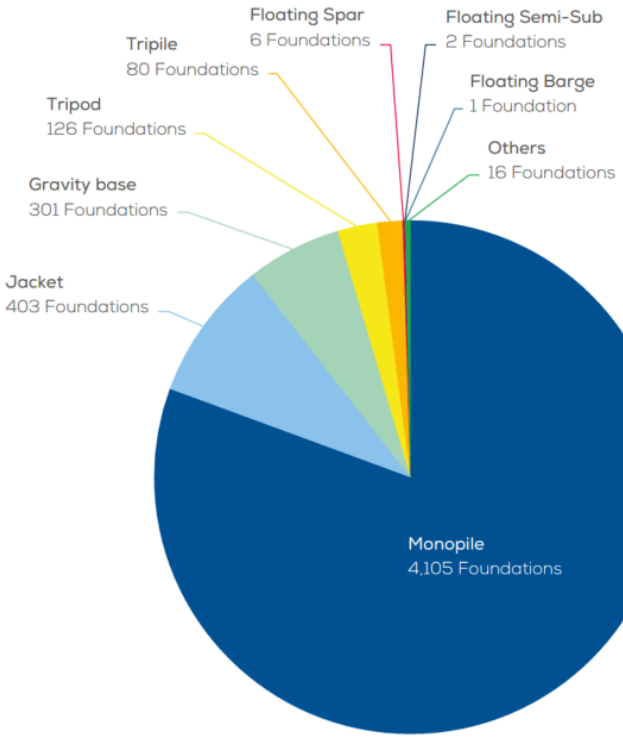

Figure 18 - Installed substructure types in Europe at the end of 2019 (Wind Europe, 2019)

3.1.2. Gravity foundations

In gravity foundation systems stability is guaranteed by the combined effect of the self-weight and the dimension of the base, usually flat, that should be big enough to resist the overturning forces. In some cases, with the aim of improving the sliding resistance and grant a protection from scour, skirts can be adopted at the base of the foundation. This type of foundations usually has a circular shape, in some cases made by a series of open or closed cells. In offshore wind industry, the base radius of the gravity foundations ranges between 25m and 30m.

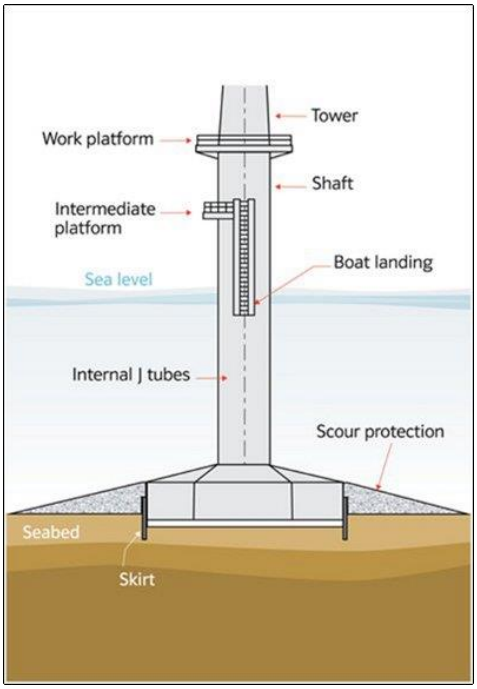

Figure 19 - Offshore gravity foundation (4C Offshore)

Design of gravity structures foundations must take into account the morphological characteristics of the seabed. The biggest disadvantage of this type of substructures is the need for a seabed preparation prior to the installation operations. In some cases, the removal and substitution of the shallowest soil layer is demanded, due to poor mechanical properties or non-homogeneity. An intervention is also needed in case of morphological irregularities; in these cases, it has to be considered the possibility of creating an artificial platform by addition of new material or by removing part of the in-situ soil.

By contrast, the main advantage of a gravity foundations is represented by its material, being concrete easily accessible and not expensive as steel, and at the same time characterized by a better resistance to fatigue. Moreover, these types of structures are

built onshore and easily transported to the installation location, where are installed by sinking, making the installation operation easy and less expensive with respect to the other foundation systems.

3.1.3. Jacket Structures

Jacket structures are commonly assembled on land and then transported to the installation location. They comprise a framed steel structure supporting the wind turbine tower, anchored to the soil by means of tubular piles or suction bucket foundations, usually installed at each corner of the substructure (Figure 20).

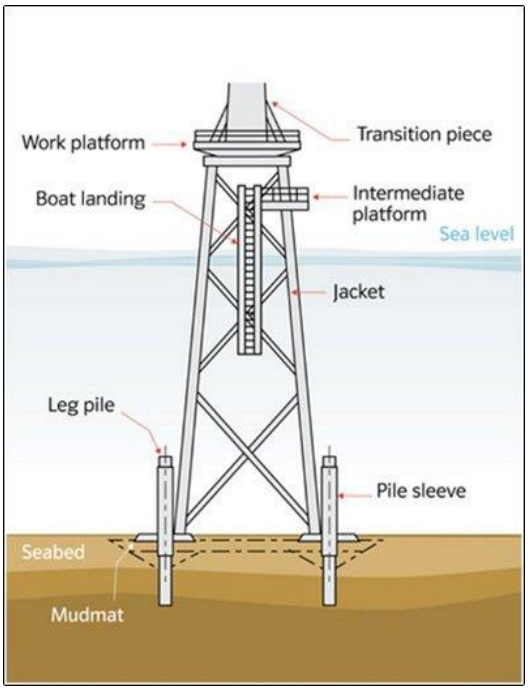

Figure 20 - Jacket structure for offshore wind turbine (4C Offshore)

In offshore wind industry, jacket structures are mainly used to support the Offshore High Voltage Stations (OHVS), characterized by heavy weight producing high static compression load on the substructure. At this time, only few wind turbines have been installed on this type of foundation, but their number seems to rapidly grow due to the increase of the turbine size and water depth installation.

Jacket structures result more easily to be built than other offshore substructures. Moreover, the reduced weight allows for a more easily transportation. On the other hand, due to the high presence of joints this type of structure can be more expensive to fabricate and require more inspection and maintenance.

Jacket structures are commonly assembled on land and then transported to the installation location, where are founded on piles (Chatzigiannelis, 2009). The installation method of these structures depends on type and dimension of the lattice structures. If the installation of the substructure and of the pile is made simultaneously, two different options can be followed:

- Leg or pin piles (Figure 21a): if the lattice is large enough, piles can be installed through the jacket legs and connected to the jacket structure through welding or grouting the anulus between the pile and the leg.
- Skirt piles (Figure 21b): piles are driven through external skirts at the base of the jacket structure.

Alternatively, the structures and the foundation piles can be installed separately. In this case piles previously installed through a frame posed on the seabed. Once the installation is completed, the frame is removed and the jacket structure can be installed.

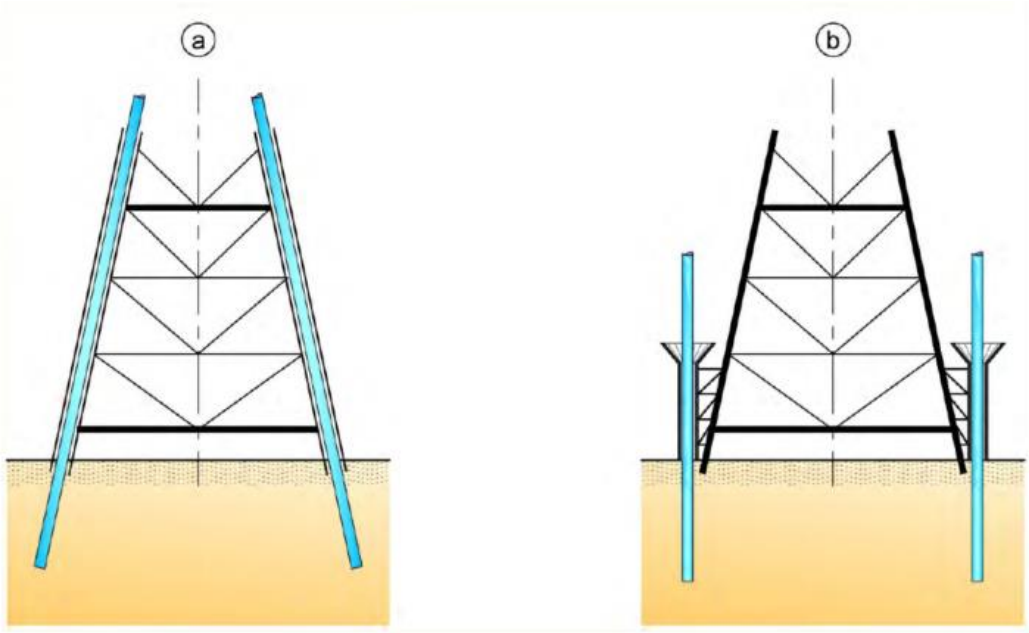

Figure 21 - Jacket structure installation through leg piles (a) or skirt piles (b) (CFMS, 2018)

Jacket structures have been widely used for oil&gas projects characterized by high water depth. However, the installation of offshore wind turbine in high level water by means of this substructure is economically not convenient. At present, Orsted awarded the construction of the biggest jacket structures in offshore wind industry. During 2020 and 2021, 56 jacket foundations, reaching a height of 75m, will be installed for the 900MW Greater Changhua project in Taiwan.

3.1.4. Floating foundations

Beyond 50m of water depth, fixed foundations for offshore wind turbines become not convenient from the economical point of view. The main reason is due to the extremely high bending moment acting on the substructures, that requires massive structure to be built. This factor makes floating structures a more reliable solution in the offshore wind industry, in case of seabed characterized by a depth over 50m.

In a floating offshore wind turbine, the tower is rigidly fixed on a barge, which itself is moored by means of chains or wire ropes to an anchor system on the seabed.

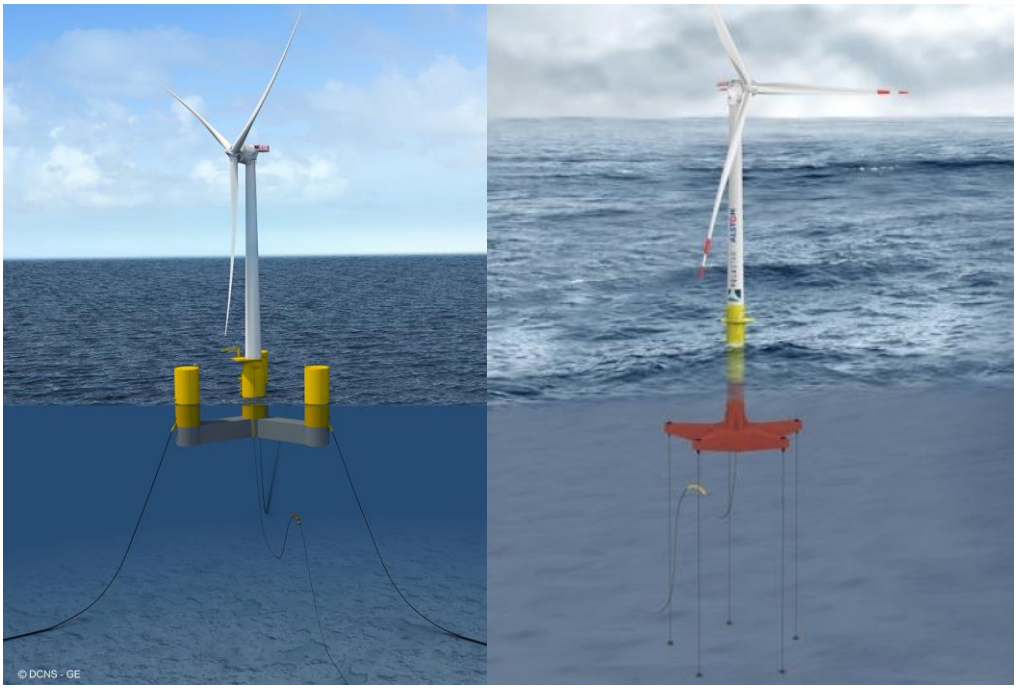

Figure 22 - Floating offshore wind turbine: catenary mooring (left) and tension leg system (right)

Three different mooring systems can be adopted: catenary mooring taut-leg and tension leg. The biggest advantages of catenary mooring are represented by the relatively low cost of the anchors and the possibility to use this system in shallow water. However, this system is generally not able to provide the needed stability. Taut-leg mooring systems becomes advantageous for high water depths, because of the smaller footprints. Tension leg mooring system is a subgroup of taut-leg systems where anchors are vertically installed below the floating structure. These systems, due to the applied tension by the mooring cables, provide a good stability but require more complex and costly anchors.

The anchorage systems commonly used for floating structures can be separated in four main categories:

- Driven piles
- Suction buckets
- Gravity base anchors
- Marine anchors

The choice of the anchorage system is closely linked to the bottom soil condition of the site.

Driven pile and suction buckets represent the most effective systems, able to guarantee high load capacity. However, the installation cost of these systems is very high.

A gravitational anchor uses the dead weight to provide the required horizontal and vertical forces.

Marine anchors, known also as drag-base anchor, can be used for application where movement of the whole system may not be critical. It represents one of the less expensive anchorage, suitable for catenary mooring system.

However, despite the anchorage system, installing a wind turbine on a floating structure represents an engineering challenge for the designer, due to the many constraints of this technology.

3.1.5. Monopiles

According to Wind Europe (Wind Europe, 2019), in 2018 monopiles represent 81.5% of all installed foundations in Europe

Monopiles represent the most used foundation type to support offshore wind turbines, due to the competitive cost and the availability in Europe. According to Wind Europe (Wind Europe, 2019), in 2018 monopiles represent 81.5% of all installed foundations in Europe.

From the engineering point of view, monopiles are largely used because of minimal seabed preparation requirements, resistance seabed movements and scour damage (Zhang, et al., 2010). This type of foundation can be considered as a sort of extension of the tower through the seabed, with a larger diameter in order to ensure adequate stiffness.

Monopile diameters, initially between 3m and 5m, have been progressively increased until reaching nowadays dimensions between 6m and 9m. Technical development in

manufacturing allows nowadays monopiles with a diameter up to 10m to be built. However, the installation of piles of such dimensions is limited by the capacity of the crane vessels.

The installation of this type of substructure is realized by means of special vessels (Figure 23), able to transport the monopile offshore, lift it and position it for the driving.

Figure 23 - Jack-up vessel installing a monopile

In monopile design, a leading role is played by soil-structure interaction, which results, for standard monopiles (diameter > 5m and thickness > 50mm), in a rigid behavior (CFMS, 2018). In this case it is important to highlight two mains different in the soil resistance component with respect to standard pile design:

- A great contribution to the global resistance is provided by the reaction acting in the lower part of the monopile:
- Using a conventional pile design method leads to an underestimation of lateral and rotation stiffness due to the larger diameter and the contribution of the axial skin friction and the shear forces at the pile toe (Figure 24).

As a consequence, the soil mechanism to be used to model a monopile has to represents as much as possible the soil stiffness.

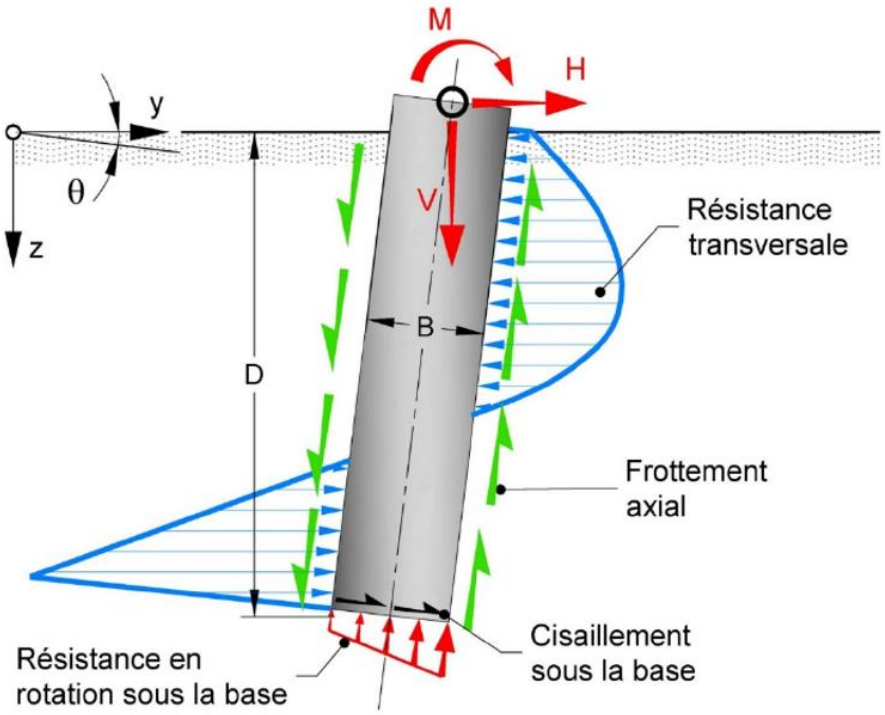

Figure 24 - Soil resistance components of a rigid monopile (CFMS, 2018)

The analysis of the natural vibration frequencies is often fundamental to evaluate piles diameter in order to avoid fatigue phenomena. These structures are dynamically sensitive because of the proximity of the vibration frequencies transmitted by the cyclic loads (wind, waves and blades rotation) and the natural vibrations frequencies.

4. Pile driving

As seen in previous Chapter, piles represent an important type of foundations in the offshore wind industry where large diameters monopiles play a fundamental role seen their relative ease of installation and structural performance if compared to other structures. In relatively soft rocks like chalk or hard glacial tills, large piles or monopiles are frequently used as foundation. Both types are installed by driving, a still today effective methodology which allows of rapidly install piles and provide piles with a significant axial and lateral capacity.

4.1. Piles installation methods

In offshore wind industry most of the foundation systems require piles installation, with the only exception of gravity foundations (§3.1.2) and some anchor systems used for floating wind turbines (§3.1.4).

Pile installation can be mainly divided in static or dynamic penetration methods. Regarding pile driving in the offshore environment, the most common installation techniques are:

- Jacking;
- Vibratory driving;
- Impact driving.

Pile jacking (Figure 25) is a static installation method, in which pile is installed by means of a hydraulic ram that push the pile within the ground. The big advantages offered by this technique with respect to dynamic pile driving techniques is represented by the reduction of noise and vibrations during the installation phase. The disadvantage is the need of a heavy ballast or anchoring system and the consequent limitation of pile size.

Vibratory driving technique (Figure 26) uses vibrations induced at the top pile by a vibratory hammer to reduce friction at the pile-soil shaft interface. This reduction allows the pile to penetrate within the soil by means of the system self-weight (vibratory hammer + pile). The use of vibratory driving technique minimizes the risk of damage during the installation, being the induced stress much lower than the elastic limit of the structural material. This type of installation is very efficient in case of pile installed in loose sands;

however, it results not so effective in case of stiff soil. Such technique is used for the initial installation of piles, as significant doubts exist about the long-term capacity of piles entirely installed by vibration. Such piles are normally impact driven in the last part to allow to reach the required axial capacity.

Figure 25 - Pile jacking operation

Figure 26 - Vibratory driving

Impact driving represents the oldest and most effective technique historically used for pile installation. Impact driving allows to install piles of any size and with large axial capacity. In particular, in the last 15 years, the impact energy which can be delivered in a single blow by a hydraulic hammer can reach several thousands of Joules.

However, the high energy delivered at each blow to the pile produces intense stresses which can easily reach 80% of the yield.

In this work a special section has been dedicated to this installation technique, as to the high energy (and stress) induced in the pile elements leads to significant risks of pile damaging in particular at the pile base, which is in most cases the most exposed part of the pile.

4.2. Pile impact driving

Since the Prehistory men have installed wood piles by means of the impact of a weight at the top. Over the years, the installation techniques have been progressively upgraded although maintaining the same basic principle.

In impact driving techniques, the impact of a falling weight on the pile top produces a compression wave traveling from the top to the pile toe. The propagation of the wave along the pile produces a temporary reduction of the shaft friction. In order to obtain the pile penetration, the induced energy shall be adequate to overcome the skin friction at the soil-pile interface, and produce a plastic, and therefore permanent, displacement at the pile toe. The installation by means of this type of technique is obtained by a succession of the described process, sometime at very high frequency, producing cumulative pile penetration.

Because of the high versatility of this installation technique, being suitable from most of the potential soil conditions, pile impact driving can be considered as the standard installation method in the offshore industry.

4.2.1. Driving systems

The installation of a piled foundation, especially in the offshore environment, is a very expensive operation. For this reason, driving machinery have been continuously developed and today very large hammers are very often used in the offshore wind industry. According to Rausche (Rausche, 2000), the so-called driving system (Figure

27) includes the hammer, the hammer cushion, the helmet and the pile cushion (in case of concrete pile). Moreover, pile driving guides are usually used to maintain the vertical alignment during the installation.

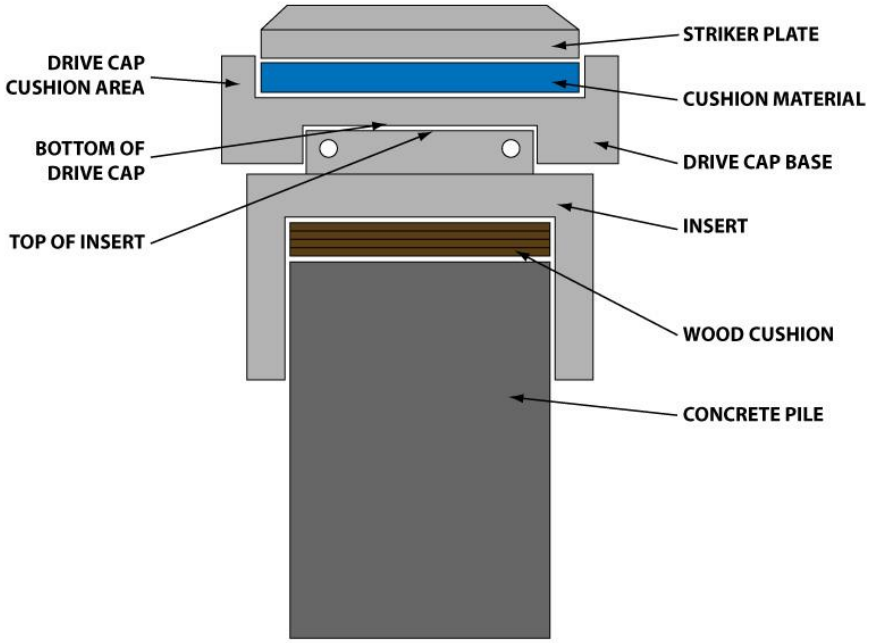

Figure 27 - Scheme of a pile driving system

Pile driving hammer are usually classified by their potential energy, evaluated through the maximum height of the ram. Actually, not all the potential energy is transmitted at the pile top. So, it is important to evaluate the efficiency of the hammers, as the ratio between the potential energy, and the kinetic energy.

Two other parameters play an important role in the selection of the hammer: the mass ram and its velocity. The product of these two parameters gives the momentum, parameter which better indicates the maximum force acting on the pile top. In fact, in absence of the cushion the velocity of the ram and the pile top are the same at the impact instant. The presence of the cushion spreads the peak force, which depends essentially on the impact velocity at the beginning of the impact. So, a greater mass of the hammer ram is needed to maintain more than possible the pile top force near its maximum values. A combination of ram mass and velocity results therefore essential to ensure pile penetration.

From the technological point of view, hammers can be divided in:

- Drop Hammers:
- Air/Steam Hammers;
- Diesel Hammers;
- Hydraulic Hammers.

The operation mode of steam and diesel hammers is equivalent, they only differ in the engine, which respectively use air pressure or combustion. Both technologies use the engine to pull the rams up to start the downward movement. Just before the impact, the steam engine is used again to generate an upward force.

Due to the high efficiency and the possibility of controlling the drop speed and therefore the energy and blow rate, hydraulic hammers have become the most used technology in the industry. Hydraulic hammer uses hydraulic pressure both to lift the ram and accelerate it downwards. This technology can produce an acceleration of up to 2g, with an energy between 35 kNm to 3000kNm and a blow rate of 50/60 blows per minute.

4.2.2. Driveability analysis

In the design of offshore pile, the optimization of pile length, size and its installation are a fundamental aspect. In order to evaluate safe, feasible and economic solutions, the design approach must combine geotechnical, structural and installation aspects. In this context, especially in the offshore industry, an accurate prediction of pile driving is a key aspect.

Pile driveability is usually assessed through the following analytical approach:

- energy balance approach.
- one dimensional wave equation approach.
- two- or three-dimensional finite element methods.

The use of energy balance equations and finite element methods represent respectively the simplest and the most complex methods. The main limitations related to these approaches consists in the low accuracy of the energy balance method and the high level of computational resources required by finite element analysis. This lead over the years

to a large use of the one-dimensional approach to perform driveability analysis and simulate the actual driving conditions.

The first model to evaluate wave equation analysis in pile driving was proposed by Smith (Smith, 1960). This method uses lumped mass to discretize the pile connected through spring and dashpot to simulate the material stiffness and damping. and simplified rheological models to simulate pile-soil interaction.

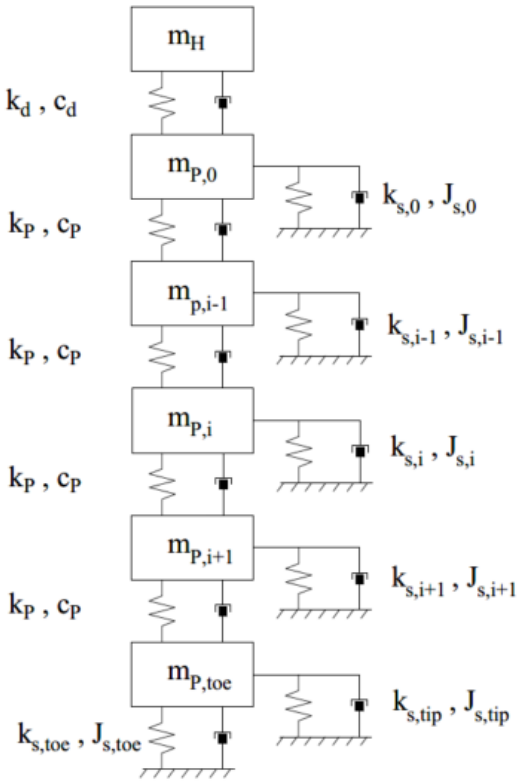

Figure 28 - Lumped-mass Smith model

The problem can be divided in two steps: the interaction between the hammer and the pile and the interaction between the pile and the embedding soil.

Pile driving system is usually modelled as a combination of three elements: two elastic elements representing the ram and the pile connected by a linear spring modelling the pile cushion.

The second step is the dynamical behavior of the pile after the hammer impact, with the aim of evaluating the pile penetration in the soil, per each blow. The Smith method consists in an equation time step solution of a one-dimensional wave iteratively applied until displacement is achieved and downward velocity is lost.

A fundamental aspect is player by the soil-pile interaction. According to this method the total soil resistance mobilized during the driving phase is:

$$R_d = R_s(1 + J\,v) = Kw + Cv \qquad \text{Equation 2}$$

where:

- R_d is the dynamic soil resistance;
- R_s is the static soil resistance;
- J is a damping constant;
- v is the velocity of the pile segment during a time interval;
- K is the spring stiffness;
- C is the dashpot constant.

Usually stiffness K is expressed in terms of the pile displacement, known as Quake Q to mobilize the maximum resistance $R_{max.}$ whose value varies in function of the soil conditions.

The major limit of the original Smith formulation was the absence of elements taking into account the radiation damping, being the dashpot introduced only to model viscous damping. The Smith model has been progressively refined over the years and at present forms the basis of various commercial software. One of the most used programs to simulate pile installation by impact driving is GRLWEAP, developed by Goble & Rausche (Goble & Rausche, 1999). Through this software is possible to analyses several aspects of the driving process, like driving equipment (hammer properties) and final pile bearing capacity.

These factors are closely related to the cost and quality of the installation. In order to determinate a successful, safe and the economical installation, for a given soil condition a driveability analysis, should aim at the optimization of pile characteristics, hammer energy and blows rate, on the basis of the following principles:

- Minimize the number of blows needed to reach the pile capacity to reduce the installation time;
- Minimize the maximum stress induced in the pile, to avoid accumulation of fatigue and potential tip damage.

4.3. Pile tip buckling

Buckling instability is one of the more occurring phenomena in pile failure. It represents the cause of failure of many structures and its importance cannot be underestimated during the design phase.

Pile buckling can be mainly divided in two main groups (Bhattacharya, et al., 2005):

- Global buckling, suffered by the longitudinal section of the pile;
- Local buckling, where the transversal section is deformed, usually at the pile tip.

The causes that can trigger the two phenomena can be of different origin and different entity, such as acting stresses exceeding the material resistance or manufacturing imperfections of the structural element.

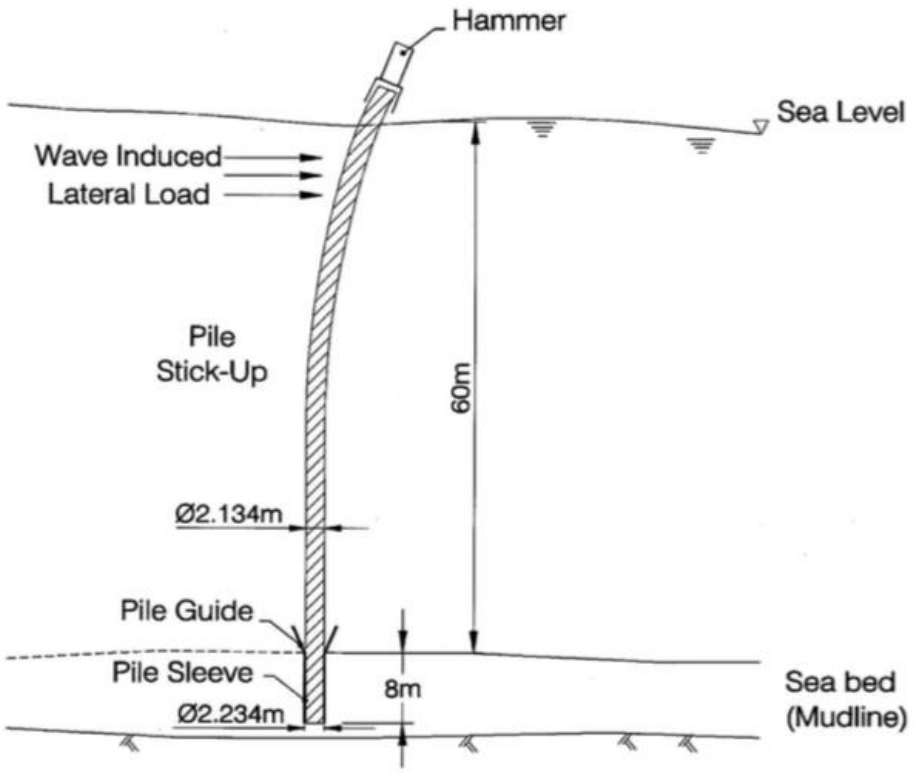

Figure 29 - Global buckling during pile driving (Bhattacharya, et al., 2005)

Regarding the global buckling, the slenderness of the pile plays a fundamental role in the potential damage. Partially exposed piles, as widely occurs in the offshore environment, amplify the risk of damage: especially during driving, the combination of horizontal forces, produced by the sea current, and the axial stress, produced by the hammer, can lead to a global buckling of the pile (Figure 29).

To avoid global buckling, a particular attention must be reserved to the following aspects:

- piles installed in extremely soft clay;
- initial imperfection, produced during the manufacturing phase of the structural element;
- loss of lateral support due to soil liquefaction.

About the first point, Eurocode suggests verifying the buckling phenomenon in case of pile installed in clay characterized by an undrained resistance below 15kPa.

A study conducted by Bhattacharya et al. (Bhattacharya & Bolton, 2004), have revealed as fully embedded piles, passing through loose to medium dense sand, if soil liquefies during an earthquake can buckle under the axial load alone.

Regarding local buckling, it appears to be particularly dangerous for thin walled piles during the driving phase, particularly for installation through hard soil and rock or when a stiff element is encountered within the soil.

This work is mainly focused on local buckling phenomenon resulted from pile tip-boulder interaction. The presence of an obstruction produces an increase of the resistance to the driving. The force needed to displace the boulder arise at the pile-boulder contact point and can lead to a local damage of the pile tip.

4.4. Boulder-soil-pile interaction

Large diameter piles, open ended and thin walled are ever more used in the offshore industry, due to the high bending stiffness offered and ease installation. At the same time these elements result particularly vulnerable to local buckling phenomenon during pile driving.

The installation through cemented soil layers or the impact against a boulder can trigger a distortion at the pile tip, which progressively propagates during pile driving, both in longitudinal and transversal directions, until a potential closing of the base section of the pile (Figure 30).

This type of phenomenon is called extrusion buckling.

Figure 30 – Damaged piles in Rotterdam harbor

To better understand this process, Erbrich et al. (Erbrich, et al., 2010), developed a numerical method, called BASIL. By means of ABAQUS, the pile-soil interaction has been modelled through fixed-end anchors distributed around the pile section (Figure 31, left) and along its length and an initial distortion is modelled at the pile tip (Figure 31, right). The different direction between the pile advancement and the distorted pile wall, generates an acting force on the pile, which progressively deforms the pile wall as the pile advance (Figure 32).

The described method highlights how this type of pile failure is dependent on an initial damage of the pile tip. With the offshore trend of increase the dimensions of the piles and in particularly the diameter to thickness ratio, the risk of create this initial damage of the pile during the transportation and installation increase. While procedures to prevent damage during transportation and mobilization have been developed, soil heterogeneities encountered during the driving can trigger the initial distortion without being clearly detectable.

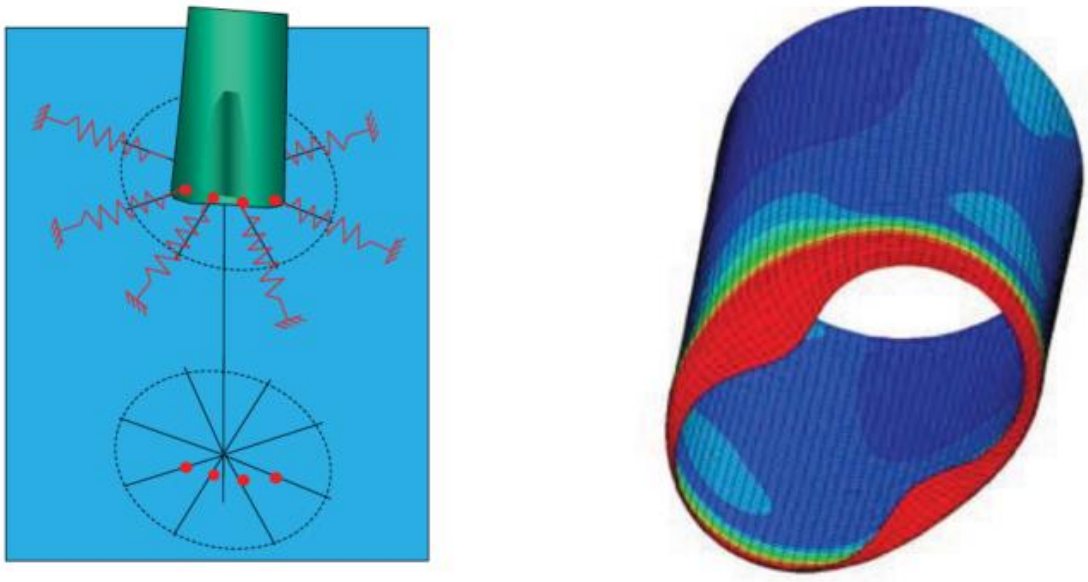

Figure 31 - BASIL model (left) and exaggerated initial imperfection on ABAQUS (right)

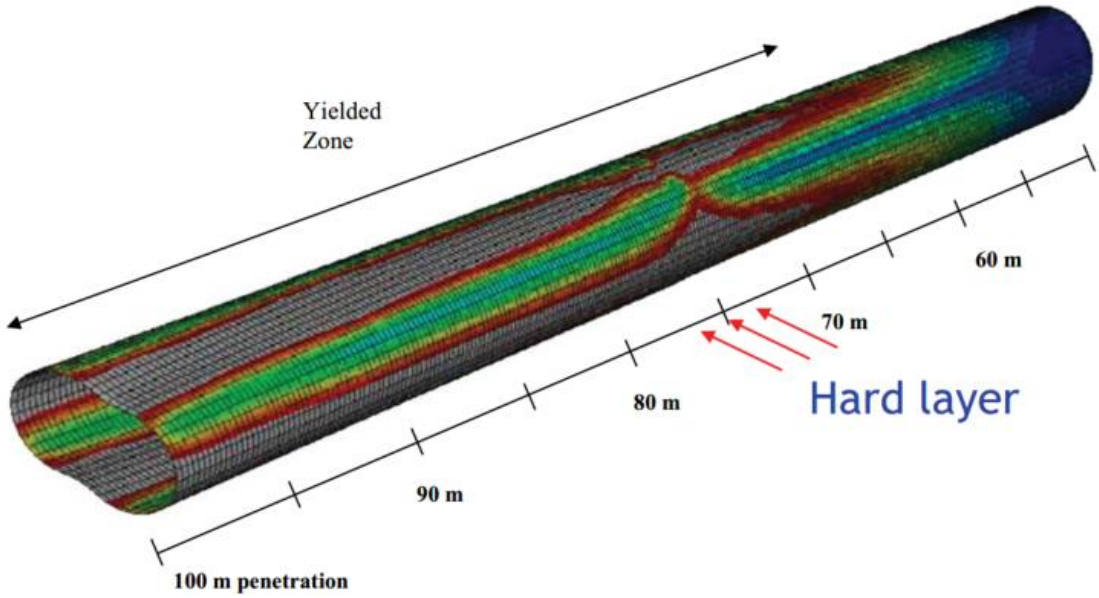

Figure 32 - Progressive pile distortion below hard layer

In particular, when a boulder is encountered, the only effect which can be observed is an increase in the resistance to driving. The force needed to displace the obstruction arises at the pile tip, with the risk of triggering the extrusion buckling phenomenon or in some cases leading to a premature refusal.

4.4.1. Refusal

Refusal due to a boulder encountered is risk commonly faced in the offshore industry.

It is a common practice in the sector, to evaluate the required hammer energy through a driveability analysis prior to the installation. However, the resistance offered by the boulder can overcome the hammer energy, causing a premature refusal.

According to API (API, 2011), "*pile driving refusal with a properly operating hammer is defined as the point where the pile driving resistance exceeds either 300 blows per foot (0.3m) for five consecutive feet (1.5m) or 800 blows per foot (0.3m) of penetration"*, resulting therefore in approximately an advancement of 1mm per blow.

Therefore, it is fundamental evaluate prior to the driving the requested energy to overcome the obstruction, in order to avoid very expensive solutions, like mobilizing and demobilizing of piling hammers or drill out of the pile.

However, the maximum energy transmitted by the pile should avoid potential local damage during pile driving. API suggests that the stresses induced in the structural element should not exceed 80%-90% of the yield strength of the material.

4.4.2. Pile tip buckling

The damage of the pile tip is a real risk occurring when a hard stratum or a boulder is encountered. As previously described (§4.4), once an initial distortion is present at the pile tip, a progressive failure of the pile can develop.

This problem is emphasized by the current trend of increase the diameter to wall thickness ratio.

API guideline (API, 2011) are frequently used to evaluate the minimum wall thickness to avoid local buckling. In case of pile to be installed by driving where hard driving conditions are foreseen, according the recommendations, the following equation should be used to evaluate the minimum wall thickness:

$$t = 6.35 + \frac{D}{100}$$ Equation 3

where:

- D, is the pile diameter in mm;
- t is the pile wall thickness in mm.

A solution frequently adopted to avoid damage is represented by driving shoes. This solution consists on an internal thickening of the pile wall close to its tip, which provides a double effect:

- increase of the resistance;
- reduction of the internal skin friction, improving driveability.

Usually the length of the thickened area is minimum one diameter while the thickness is increased up to 50%.

Even though the adoption of these prudential solutions, cases of local buckling have been reported (Figure 33), highlighting the difficulty of such recommendations to provide a safe guidance for pile design and the correlation of the damage mainly with the axial force acting at the pile tip (Randolph, 2018).

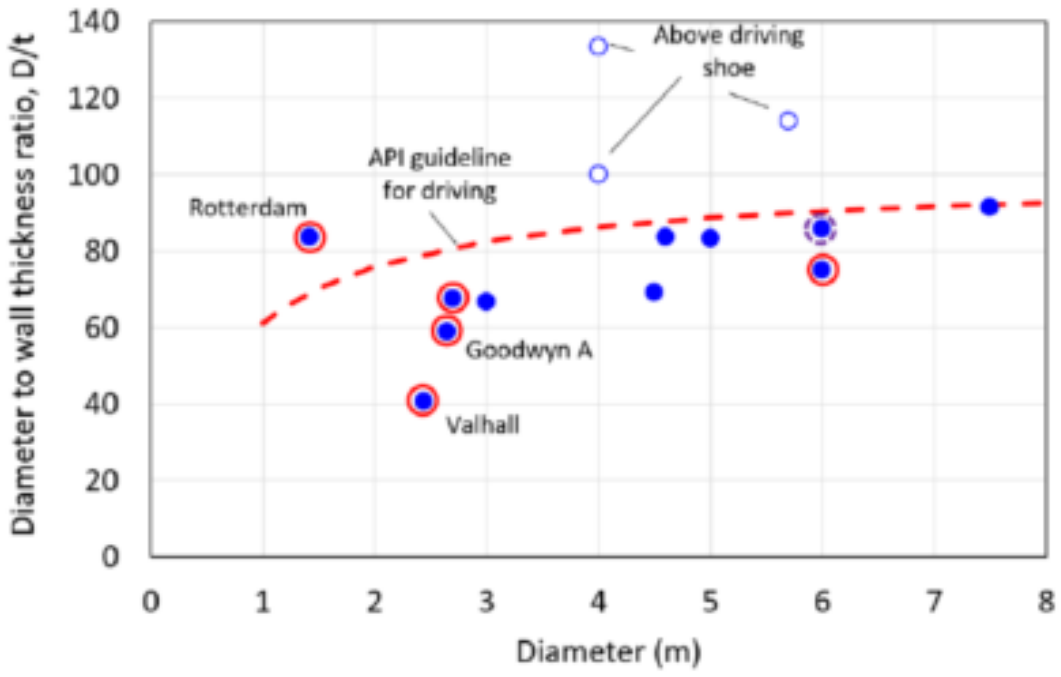

Figure 33 - Dimensions of open-ended piles experienced extrusion buckling damage (red and purple circles)

Therefore, a special attention has to be dedicated to the force which arise at the pile-boulder contact point. The pile-boulder interaction represents a very complex problem, mostly influenced by the following aspects:

- boulder size and strength;
- embedding soil mechanical behavior;
- pile-boulder contact point;
- pile stiffness.

Only a few studies on this subject are available in literature. Holeyman et al. (Holeyman, 2015) proposed a dynamic model based on the 1D theory where the boulder-pile-soil interaction is modelled through a series of springs and dashpots (Figure 34), whose stiffness and damping parameters are function of the boulder geometry and density and of the shear modulus of the embedding medium.

The mechanical model is developed through the software GRLWEAP, which limit the numerical analysis to the following assumptions:

- linear material behavior;
- possibility to model only the axial behavior.

The result of the analysis is given in terms of load provided by the boulder for a given force applied by the hammer. This result is finally compared with the maximum axial force able to trigger the pile tip buckling phenomenon.

An assessment of the force which can cause the tip damaging can be made by means of the approach proposed by Aldridge et al. (Aldridge, et al., 2005). By using an upper bound theory for an assumed plastic hinge mechanism, showed in Figure 35, an estimate of the amplitude of the horizontal point load able to cause the formation of the plastic hinge, can be evaluated through the following relationship:

$$F_{lat} = 1.4\,\sigma_y t^2 \qquad \text{Equation 4}$$

where:

- F_{lat}, is the lateral force which cause the pile buckling;
- σ_y, is the yield stress of the material;
- t, is the pile wall thickness.

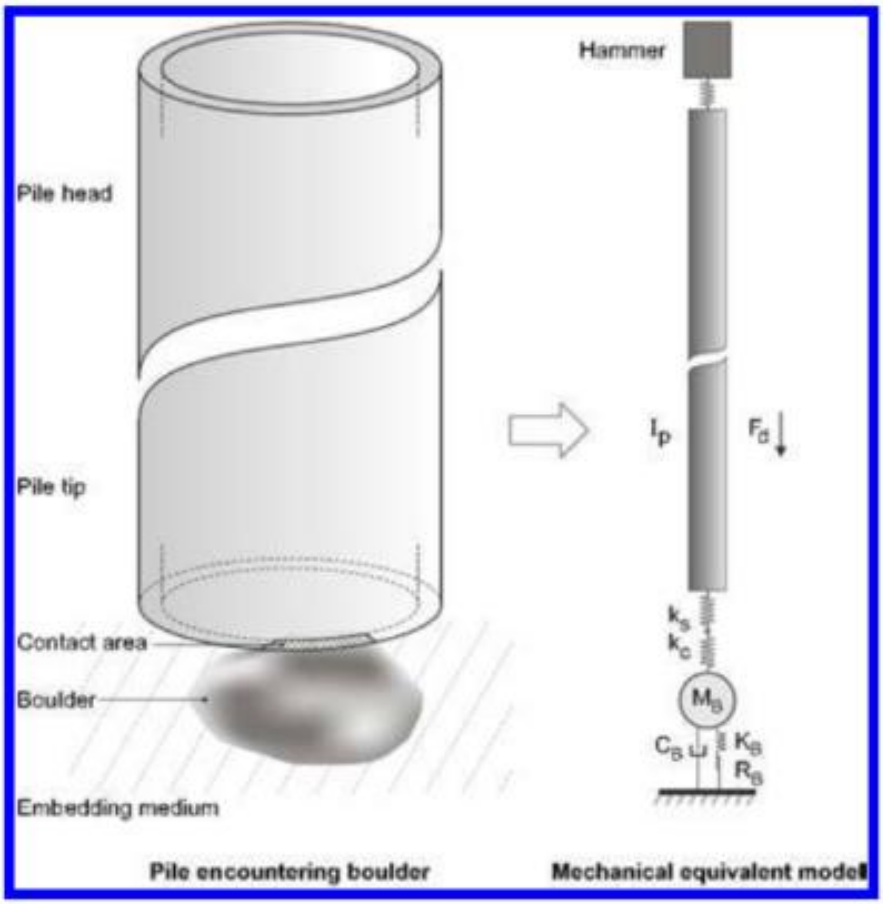

Figure 34 - Pile-boulder-soil model (Holeyman, 2015)

The relationship has been validated afterwards through laboratory tests conducted on steel pile and 3D numerical analysis, by means a further estimate of the near-axial force that produce the local buckling has been evaluated. For a force applied at 1:4, the amplitude which produces the tip damage can be estimated as:

$$F_{lat} = 2.8\,\sigma_y t^2 y \qquad \text{Equation 5}$$

It is important to highlight that the proposed relationships are only dependent on the thickness and steel yield stress and not correlated with the diameter to thickness ratio D/t as suggested by the API recommendations.

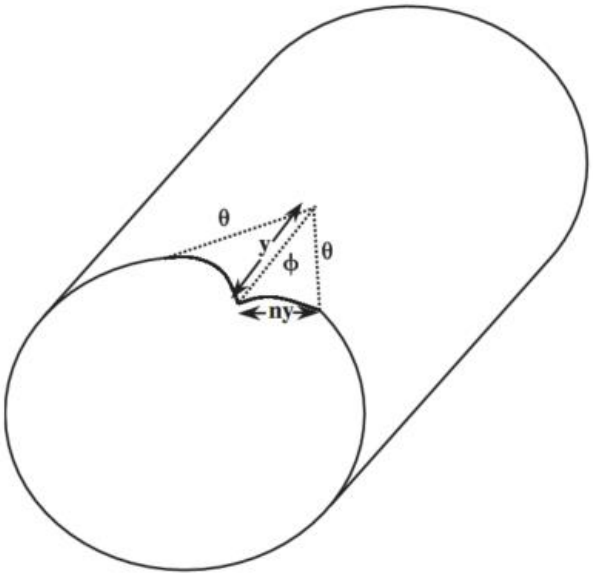

Figure 35 - Plastic hinge mechanism (Aldridge, et al., 2005)

5. Static 2D FEA analysis

5.1. Introduction

During pile driving in chalk, when a flint is encountered, two possible phenomena could occur: the flint breakage or the flint plastic displacement in the soil. Both the phenomena are dependent on the strength parameters of the flint and the embedding chalk. A previous work (Gargarella, 2018) on the same subject has fully investigated the condition for which there is a transition from a soil bearing capacity, governed by the undrained resistance of the embedding soil, to a flint failure, governed by its tensile strength. By comparing the bearing capacity ,obtained from the T-bar solution, and the flint tensile strength ,obtained from the Brazilian test equation, a ratio of S_u/σ_t =0.13 has been found between the undrained resistance and the flint tensile strength, as a transition value between the two failure conditions. Thus, for S_u/σ_t <0.13, the failure mechanism is governed by a bearing capacity failure. Due to the high flint tensile strength with respect to the low strength of the soft chalk, the flint is normally displaced into the chalk. The force needed to displace the flint arises at the contact point between the pile and the flint, and its magnitude and direction are mainly dependent on the flint size and shape, on the chalk strength/stiffness and on the position of the contact point. Since the strength parameters of the materials could be evaluated through a proper site investigation, the biggest uncertainties are represented by the position of the interaction point and the flint shape and size. With the aim of studying the influence of these two factors and evaluate a valid model to be used for the more complex dynamic analysis, 2D plane strain FEM analysis have been carried out.

5.2. Static Analysis Model

5.2.1. Geometry and mesh

The embedded flint has been modelled at the center of a square model, whose dimension is evaluated as 50 times the major flint axis to avoid influences of the boundaries. The analyses have been carried out in plane strain condition with an imposed field stress of 400 kPa. With the aim of studying the influence of the flint shape on the flint/pile-wall interaction, three different flint geometries have been explored, one circular and two ellipsoidal. The horizontal axis of the ellipsoidal flint has been kept constant and equal to

the diameter of the circular flint for comparison purpose, while two different size of the vertical axis have been considered, equal to a half and a quarter the horizontal axis (Figure 36).The analysis have been performed for two different flint sizes, by considering the horizontal axis equal to 0.2 m and 2m. Due to the static loading and the absence of inertial forces, the obtained results are perfectly scaled by a factor equal to 10.

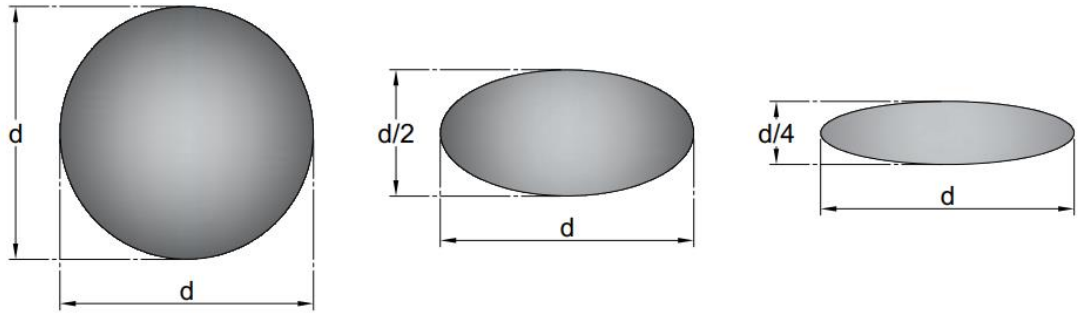

Figure 36 - Flint Geometries

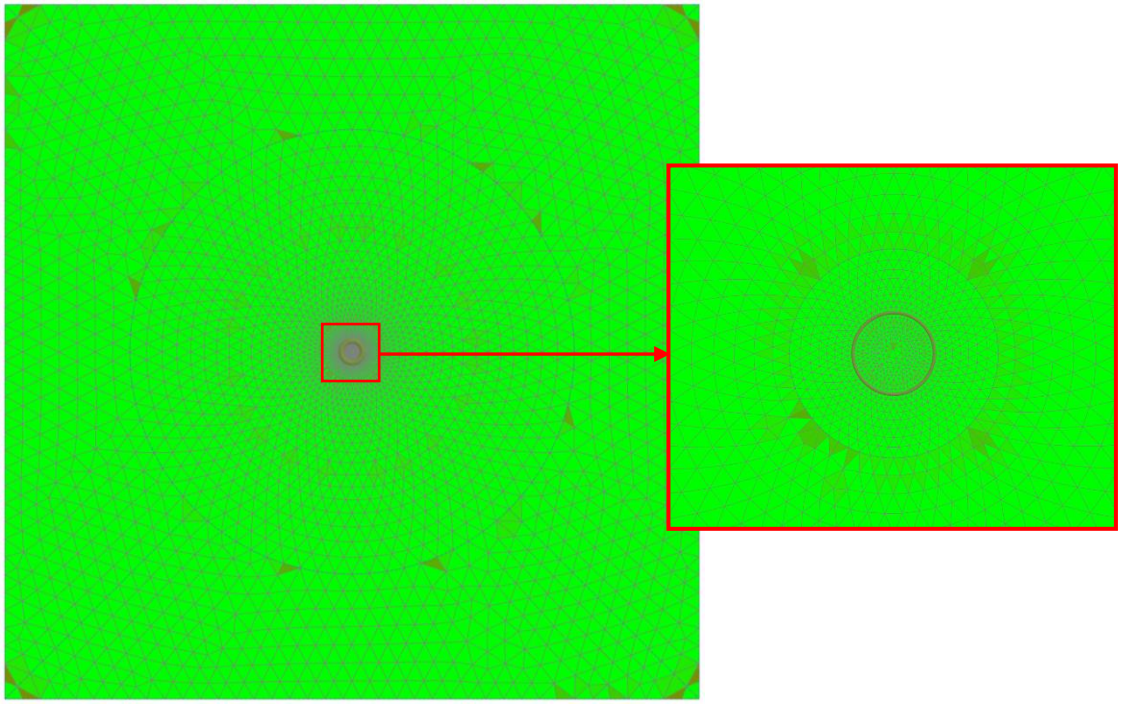

Figure 37 - Mesh quality

For the meshing of the numerical model, 15-noded elements have been chosen. To improve the mesh quality a series of polycurves have been added around the flint. This allowed to set different mesh density around the flint and gradually refine the mesh from the boundaries to the area close to the flint, where high strain gradients are expected. As a result, a mesh with the same accuracy but a reduced number of elements is obtained

(Figure 37). A sensitivity analysis has been carried out to evaluate the proper mesh density to reduce the computational time and, at the same time, obtain good quality results.

5.2.2. Soil and Flint Parameters

Since previous studies (Gargarella, 2018) have proved that the flint is mostly displaced into the soil without breakage, a Mohr-Coulomb linear elastic model has been used to represent the flint behavior. Strength and deformability parameters have been chosen to let the flint behave as a rigid body with respect to the embedding soil. A Guest-Tresca model has been chosen as failure criterion for the chalk in undrained conditions during offshore pile driving, by using the Undrained C feature in Plaxis 2D. This feature allows to perform total stress analyses, with undrained stiffness and shear strength as main parameters of the soil. The disadvantage of this approach is that no distinction is made between total and effective stresses.

A grade D_m chalk has been considered, whose strength and deformability parameters have been chosen after a literature review (§2.1.4 and §2.2.4), as the mean value for this type of soil.

Table 2 shows the materials parameters used for the static finite element analysis.

Chalk Parameters			**Flint Parameters**	
E_u [GPa]	**S_u [kPa]**	**ν_u [-]**	**E [GPa]**	**ν [-]**
0.1	100	0.495	80	0.125

Table 2 - Materials strength and deformability parameters

To allow relative localized displacements between the flint and the embedding chalk an interface has been considered with the same strength parameters of the chalk. A sensitivity analysis has been carried out on the strength reduction factor R_{inter}, by using 1, 0.5 and 0.1. This parameter governs the interface strength, which in undrained condition, is calculated from the embedding soil strength as follow:

$$f_s = R_{inter} S_{u,soil} \qquad \text{Equation 6}$$

where:

- f_s, is the shear strength of the interface;
- $S_{u,soil}$, is the undrained shear strength of the soil.

5.3. Imposed vertical displacement analysis

At a global scale, if the pile size is large and heavy pile overall driving will not be affected by the flint presence. Thus, the pile, during its vertical advancement, will plastically displace the flint into the soil. In turn, the flint will react to this imposed displacement with a dynamical force, which could be such in magnitude and inclination to initiate the deformation of the pile steel wall.

The main problem is thus related to the interaction forces exchanged between the flint and pile that at a local scale could damage the pile tip. To have a first assessment of the flint/pile-wall interaction, static finite element analysis have been carried out, by imposing a purely vertical displacement on the flint, with the horizontal component fixed to zero and focusing on the horizontal and vertical forces needed to displace the flint within a soft chalk. Such model simulates the impact of the pile wall on the flint in the hypothesis of no slip and of an infinite elastic radial stiffness of the pile; it should provide an upper bound of the static reaction force, which will be correct as a limit for very low pile velocity and acceleration during each impact. For each investigated geometry, the imposed displacement has been applied at 10 different points, moving the point where the displacement is imposed from the flint center to his right edge at 90° along a clockwise direction. The magnitudes of the forces have been evaluated as the values in correspondence of the plateau in the load displacement curves, corresponding to a complete development of the failure mechanism.

5.3.1. Circular Flint

To validate the model, the first analyses have been performed on a circular flint (Figure 38); this allowed to check the calculations and the numerical model of the previous work presented on the same subject (Gargarella, 2018) which was the starting point of this work.

To evaluate the influence of the strength of the interface, a sensitivity analysis has been performed on the R_{inter} parameter (Equation 6), by using three different values: 1(fully rough), 0,5 and 0,1. The load-displacement curves obtained are plotted in Figure 39 and

show a typical elasto-plastic behaviour in which a first linear part is followed by a non-linear behaviour until a plateau is reached. Since we are interested in the value of the force needed to fully develop a plastic displacement of the flint, for each analysis the value of the force in correspondence of the plateau has been retained.

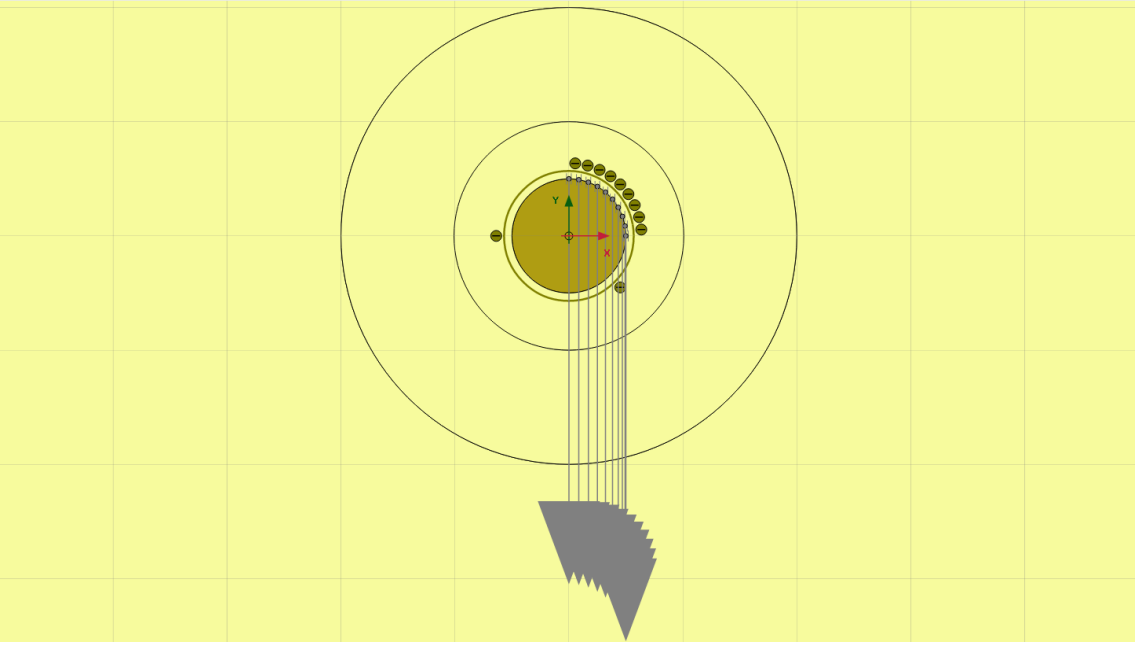

Figure 38 - Imposed vertical displacement analysis model

The obtained results are presented in Figure 40 and Figure 41, in terms of normalized horizontal F_x and vertical F_y forces versus the normalized distance of the contact point δ from the flint centre, normalized by its radius R.

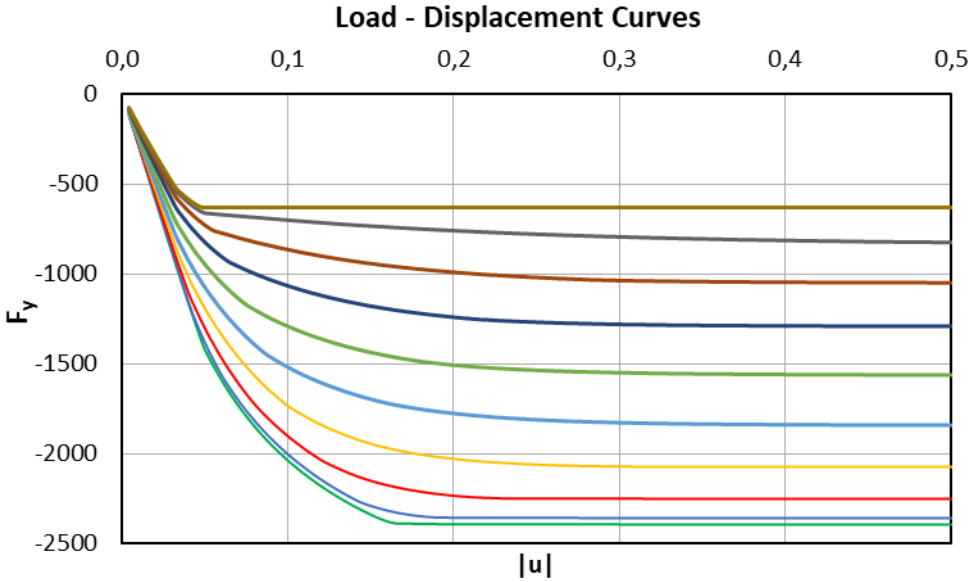

Figure 39 - Load-displacement curves

As the flint is modelled as a cylinder displaced in plain strain conditions, the closed form solutions of laterally loaded piles (deep failure) and of the T-bar can be used to validate the numerical results in the case of vertical displacement imposed at the point at the top of the flint. In order to compare them with the factor N_c, proposed by Randolph&Houlsby (Randolph & Houlsby, 1984), the forces have been normalized by dividing them for a factor equal to S_uD, where S_u is the undrained resistance of the chalk and D is the flint diameter.

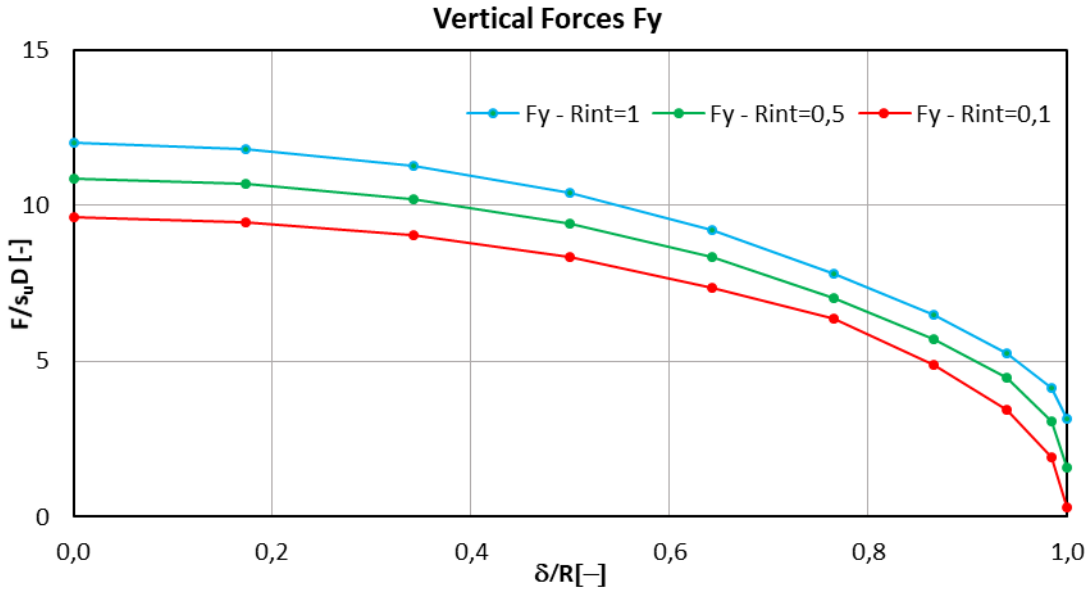

Figure 40 - Circular Flint - Normalized vertical forces

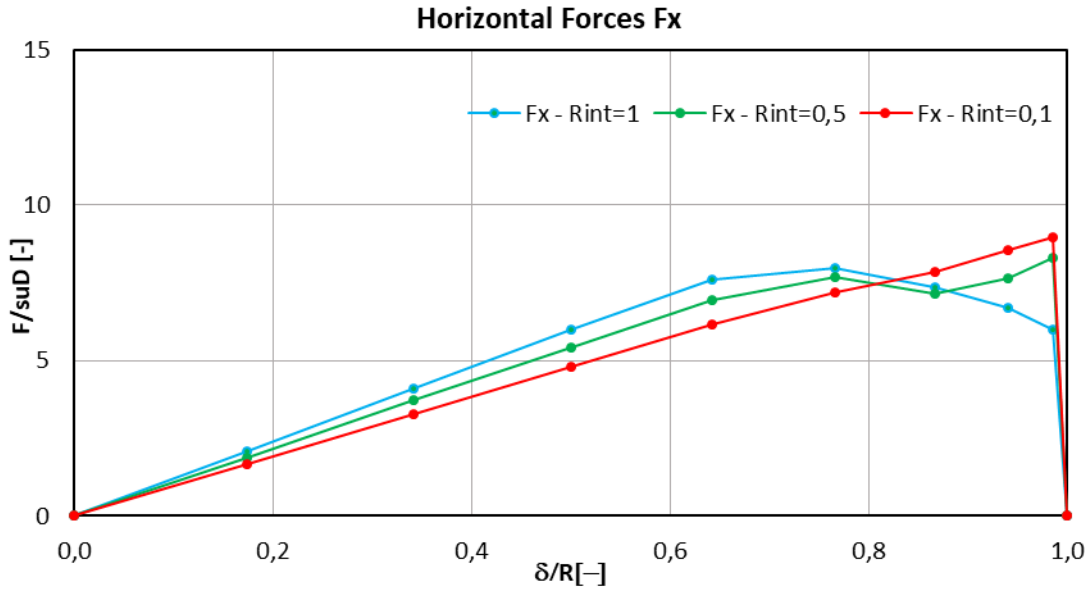

Figure 41 - Circular Flint - Normalized horizontal forces

As shown in Table 3, the normalized vertical forces obtained with a centered imposed displacement match quite well the values of the roughness factor N_c proposed by the previously quoted Authors.

Analytical solutions	α_R	1	0.5
	$N_c=N_{lim}/S_uD$	11.94	10.82
Numerical results	R_{inter}	1	0.5
	$F_{v,y}/S_uD$	12	10.86

Table 3 - Comparison between the obtained vertical forces and the roughness factor values proposed by Randolph&Houlsby

By reducing the R_{inter} parameter a consequent constant reduction of the vertical reaction forces has been noticed.

A more complex behaviour is showed by the horizontal forces: the reduction of the interface strength is followed by the increment of the force the more the flint is hit laterally. This result is due to the complexity of the failure mechanism, which is a combination of a bearing capacity failure and a rotational sliding.

In order to understand better this flint behaviour, the resultant forces, obtained as the vector sum between the vertical and horizontal forces, and their orientation have been analysed. Figure 42 shows how the more the strength of the interface is reduced the more the resultant forces trend to a constant value, equal to the bearing capacity of the flint.

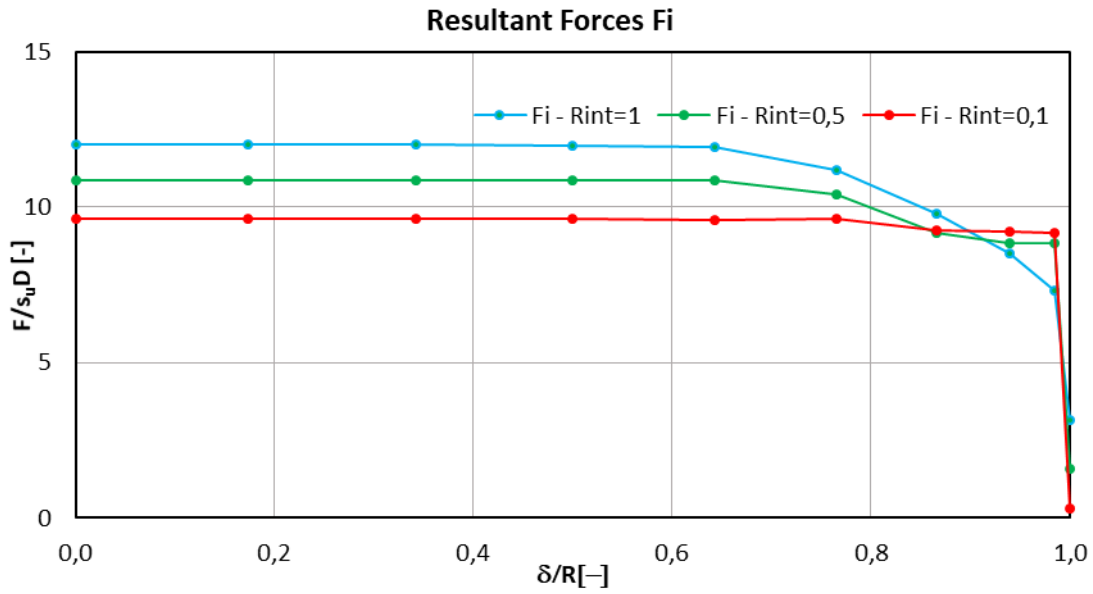

Figure 42 - Circular Flint - Trend of the normalized resultant forces

This means that, as shown in Figure 43, the resultant forces tend to remain perpendicular to the flint border at the displacements application points, pushing the flint laterally the more the flint is hit laterally.

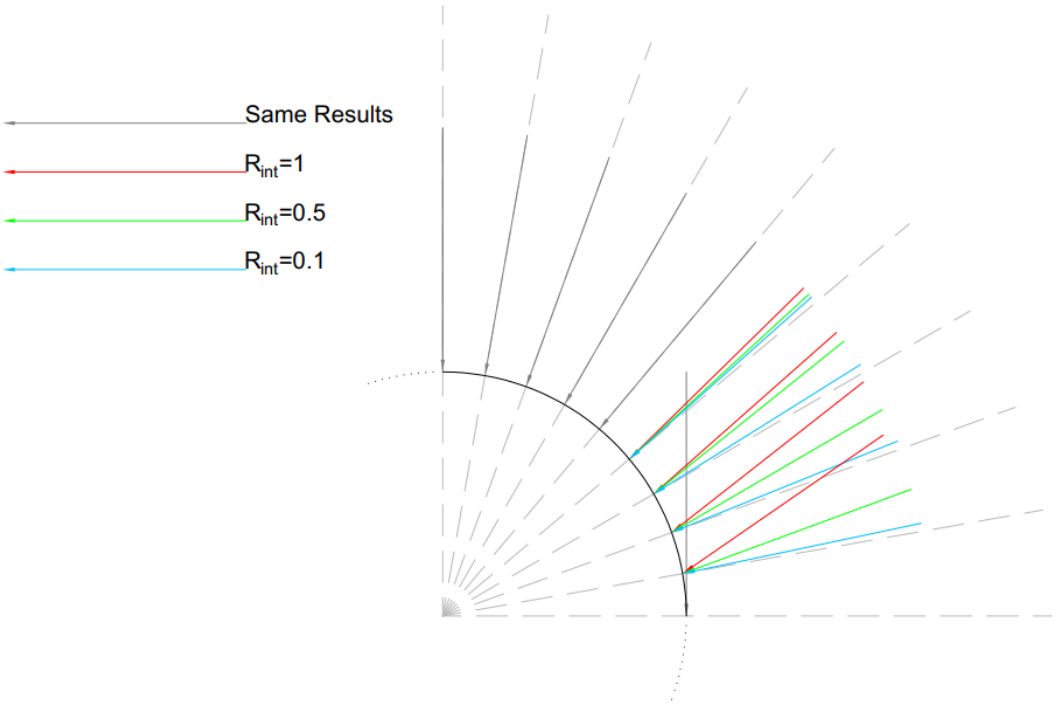

Figure 43 - Direction of the resultant forces

To understand better the behaviour of the flint, a focus on its final overall displacement obtained per each analysis has been done; in particular, Figure 44 shows the horizontal and vertical displacements experienced by the central point of the flint normalized by its radius. It is noticed that until the flint is hit at half is radius, the displacement is equal for the three analysed cases. This is confirmed by the fact that the same result is obtained for the direction (Figure 43) and for the value of the resultant forces, that remains constant (Figure 42). Moving over this point, the more the interface is weak, the more the horizontal displacement grows and the vertical one decreases.

With the purpose of explaining this latter result, the resultant forces that arise at the contact point have been decomposed in their tangential and perpendicular components to the flint surface. By plotting the tangential forces, as in Figure 45, it is possible to understand better the failure mechanism of the flint.

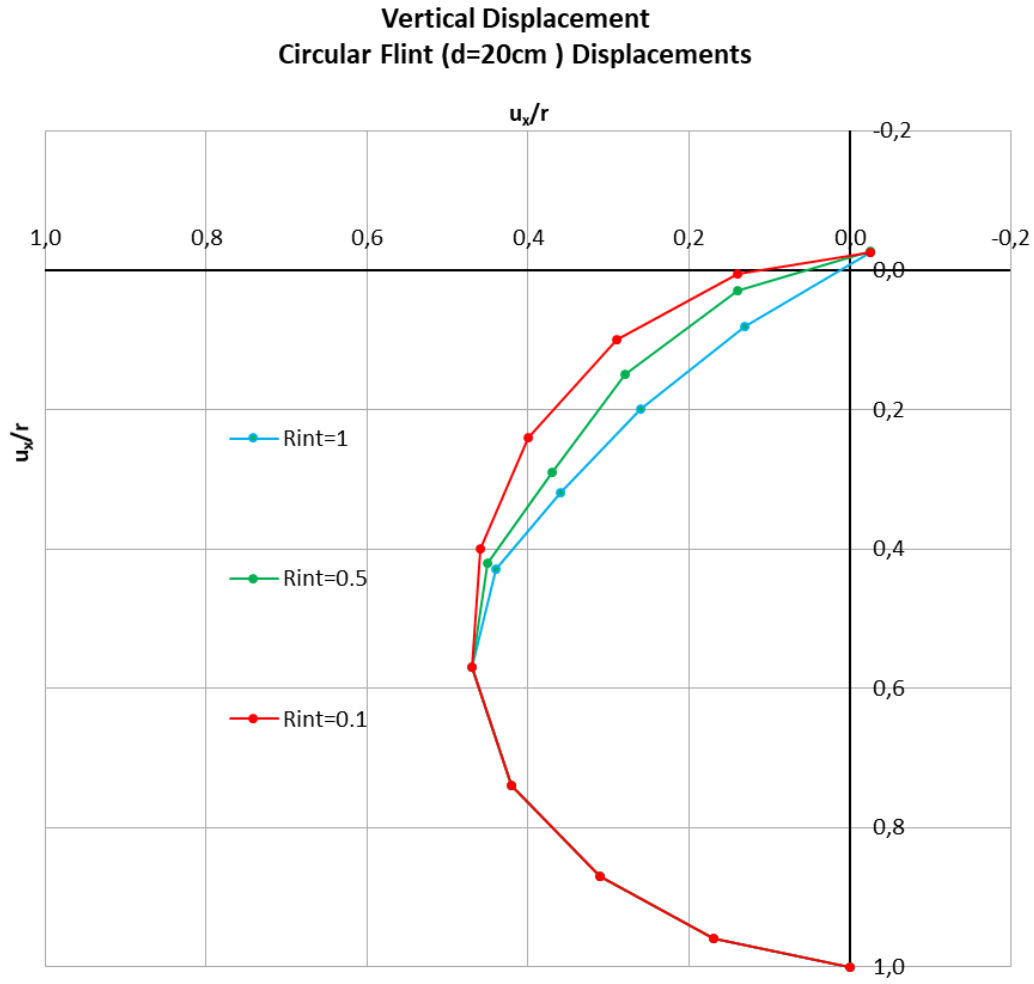

Figure 44 - Flint central point displacements

In case of maximum resistance of the interface, the ultimate torsional resistance is mobilized only when the applied imposed displacement is tangent to the flint surface, with a consequent pure rotational sliding failure mechanism. By reducing the interface strength, the full rotational resistance is mobilized for more centred contact point, as shown by the plateau reached by the tangential forces. In view of the obtained results it is possible to state that with a reduced interface strength, when the circular flint is hit laterally a full rotational sliding failure occur early, with the consequent that the flint itself can be no longer dragged down and it has to be displaced mostly horizontally; numerical results show that this combination provides higher values of the modulus of the force. As well, this lead to an increase of the horizontal forces the more the interface strength is reduced and the flint is hit laterally.

This allows to conclude that, except for the possible plastic deformation imposed to the pile wall, hitting the flint/boulder on a side does not necessarily constitute a less dangerous condition.

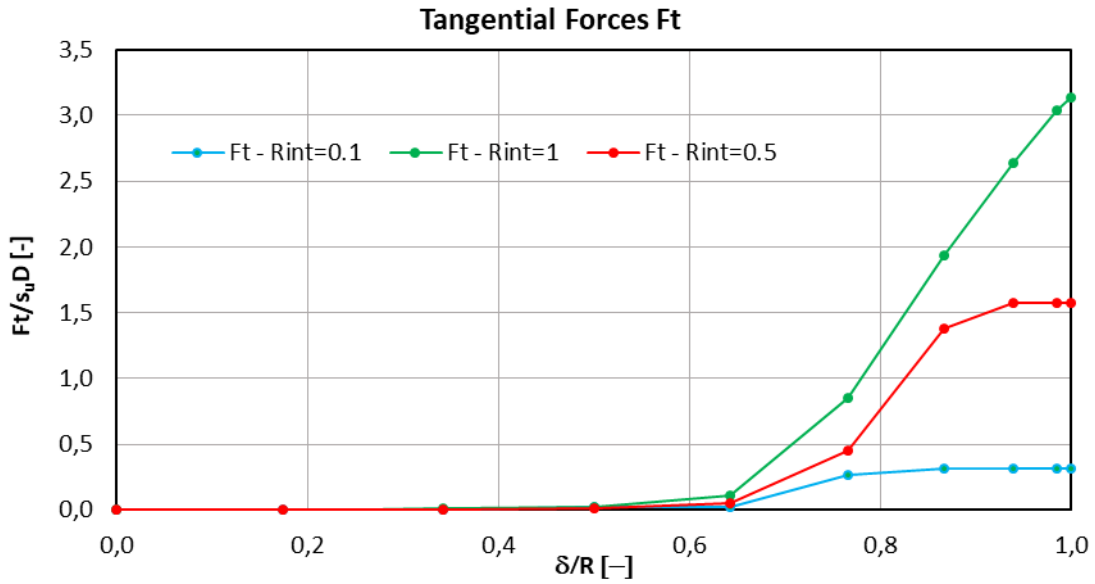

Figure 45 - Circular flint - Tangential forces

5.4. Ellipsoidal flint

To evaluate the influence of the flint shape, the analyses with imposed vertical displacements have been carried out by considering two ellipsoidal flints with two different size of the vertical axis, respectively equal to d/2 and d/4. As for the circular flint, the application point of the imposed displacement has been changed for each analysis by moving it from the center to the flint extremity and a sensitivity analysis has been performed by using three different values of the R_{inter} parameter.

Figure 46 and Figure 47 show the trends of the vertical (continuous line) and horizontal (dashed lines) forces obtained respectively for a flint with a vertical axis equal to d/2 and d/4.

Focusing on the effects generated by the different shape, it is possible to notice that, by reducing the vertical axis size, a more rapidly decrease of the vertical forces is obtained when the flint is hit more laterally. An analogy could be made with the reduction in the bearing capacity of a shallow foundation due to an eccentric load. Indeed, the more the vertical axis is reduced the more the flint assumes the shape of a shallow foundation.

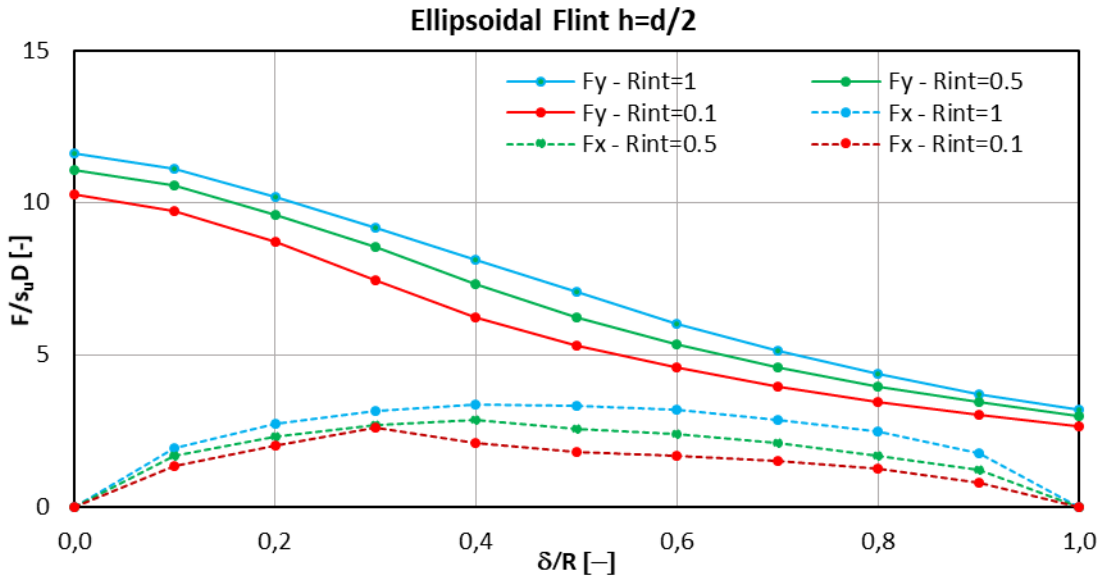

Figure 46 - Ellipsoidal flint h=d/2 - Vertical and horizontal forces

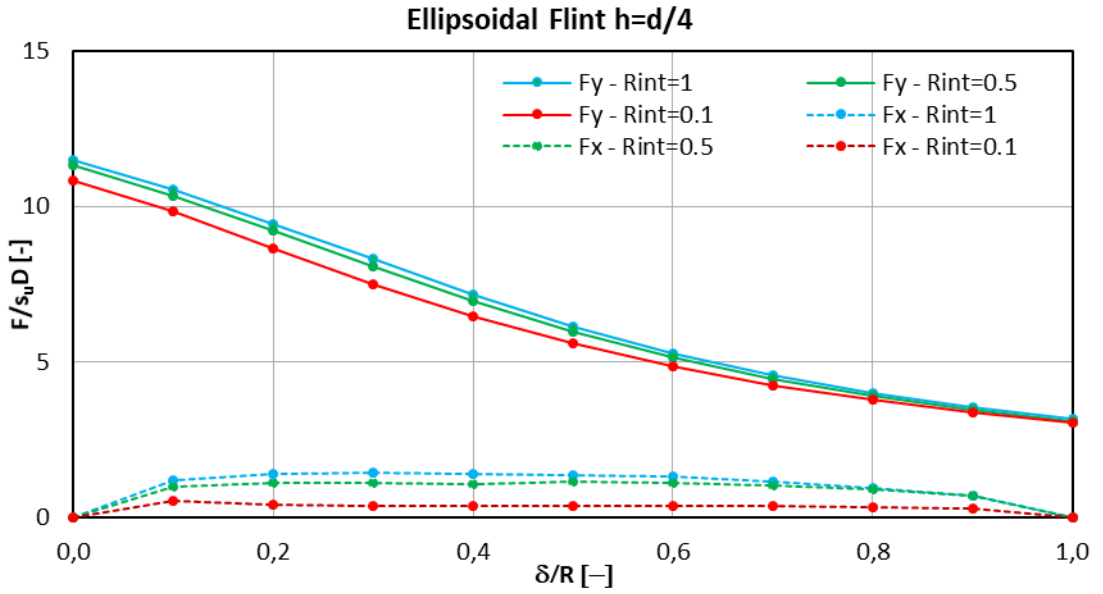

Figure 47 - Ellipsoidal flint h=d/4 - Vertical and horizontal forces

Similarly, a reduction of the vertical axis is followed by a reduction of the horizontal forces. A reasonable explanation of this result could be given by the fact that, as a result of the vertical axis size reduction, the resistance offered by the embedding soil to the lateral penetration decrease.

As a result of the different strength interface, it is possible to notice that in this case the reduction of the R_{inter} parameter led to a consequent reduction of the obtained forces. Regardless of the application point of the imposed displacement, no increase of the

horizontal forces has been reported. This result it is related to the different shape of the flint: the ellipsoidal shape does not allow failure mechanisms where a pure rotational sliding occurs. So is possible to state that the failure mechanism is not affected by the strength of the interface. This is confirmed by the plots of the inclined forces (Figure 48 and Figure 49), that show how only a small reduction of the forces is obtained by changing the interface strength parameter.

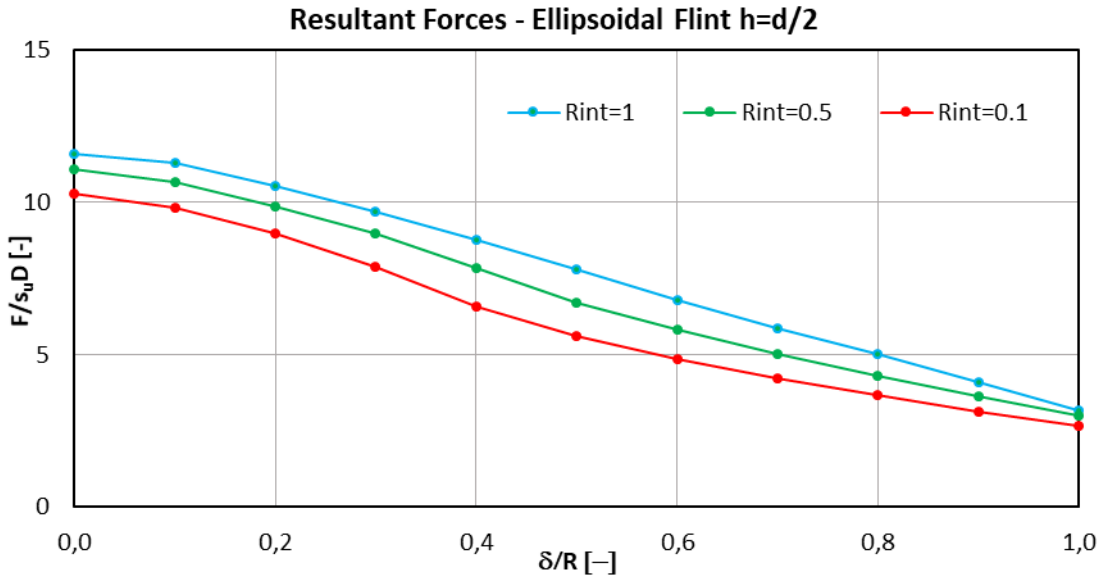

Figure 48 - Ellipsoidal flint h=d/2 - Resultant forces

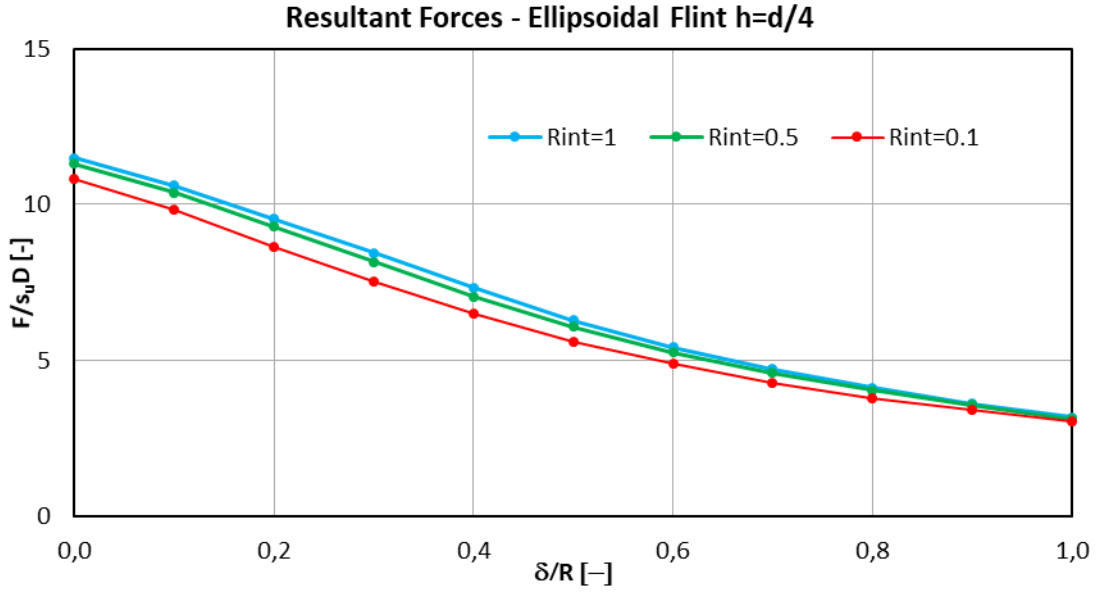

Figure 49 - Ellipsoidal flint h=d/4 - Resultant forces

5.5. Influence of the pile presence

The analyses carried out so far do not take into account the behaviour of the pile, which is assumed to fully restrain the horizontal component of displacement. The pile presence could lead to different failure mechanisms from the ones observed by applying a simple vertical displacement, if its radial deformability is accounted for. In principle, a different amplitude of the force at the contact point could be obtained. In particular, the two main factors that may affect significantly the results are the pile wall stiffness and the radial stiffness of the pile.

The presence of the pile could modify the flow of the soil developed around the flint, observed in the previous chapter. This phenomenon could be compared to the influence of the shaft on the resistance of a ball penetrometer (Zhou, H., Randolph, F., 2011). As a consequence, a potential different flint behaviour could be obtained and therefore the influence of the pile wall should be investigated.

Focusing on the interaction forces between the pile and the flint, a significant role is played by the circular stiffness of the pile. Considering an imposed vertical displacement with the horizontal one fixed is equivalent to consider a pile with an infinite radial stiffness. So, if the real circular stiffness of the pile is taken into account, reduced values of the horizontal forces, with respect to the ones previously computed, should be expected.

The following paragraphs present the results of 2D static finite element analysis carried out with the aim of explore the influence of these two factors and find the best model to be used for the more complex dynamic analysis.

5.5.1. Pile model

A pile of 4m diameter with a wall thickness of 65mm has been considered. The thickness has been evaluated according to the API recommendation of D/t=60 for commonly-used offshore platform steels (API, 2011). A linear elastic behavior has been chosen to model the pile steel material, with a Young's modulus of E=210GPa and a Poisson's ratio of ν=0.2.

To simulate the 3D geometry of the pile in a 2D plane strain model, the pile wall has been modelled as a plate element connected to some springs, added to the model as horizontal fixed-end anchors. During pile driving in a low- medium density chalk, the pile creates

puttified zone of remoulded chalk close to the shaft, characterized by high pore pressure. As a consequence, only a very low shaft shear resistance is mobilized (Jardine, et al., 2018). To model this phenomenon, between the plate and the soil, an interface with a strength reduction factor of R_{inter}=0.01 has been added. The stiffness of the springs has been evaluated in order to model the circular stiffness of a pile with the same features. Two different stiffness values have been used to differentiate the pile end section deformability from the other sections. According to Roark and Young (Roark & Young, 1975), the inwards deflection ρ_{lat} under a lateral load per unit length w for a ring of diameter D and wall thickness t supported at each side can be expressed as:

$$\rho_{lat} = \left(\frac{\pi}{4} - \frac{2}{\pi}\right)\frac{0.75wD^3\left(1 - v_{pile}^2\right)}{t^3 E_{pile}} \qquad \text{Equation 7}$$

Based on finite element analysis performed by Aldridge et al. (Aldridge, et al., 2005) on the end section of a pile laterally loaded, the lateral stiffness is similar to that derived with the solution proposed by Roark and Young (Roark & Young, 1975) for a ring of approximately 0.5D length. With this equivalent length, the relationship between the pile toe lateral deflection and the lateral force acting on the pile can be expressed by:

$$\rho_{lat} = \frac{0.204F_{lat}D^2}{t^3 E_{pile}} \qquad \text{Equation 8}$$

From this equation, the lateral stiffness of the pile end section can be evaluated as:

$$k_e = \frac{t^3 E_{pile}}{0.204D^2} \qquad \text{Equation 9}$$

Finite element analysis performed with the aim of evaluating the circular stiffness of a pile loaded by a punctual force at the bottom (Gargarella, 2018), confirm how the results

obtained through this equation are in agreement with the stiffness obtained by applying a unit horizontal displacement to a pile tip in PLAXIS 3D.

Using this relationship, for the pile considered in the analysis, the following value has been obtained:

$$k_e = \frac{(65mm)^3(210GPa)}{0.204(4m)^2} = 17669\ kN/m \qquad \text{Equation 10}$$

The obtained finite element model, shown in Figure 50, should be able to reproduce the circular stiffness of the pile.

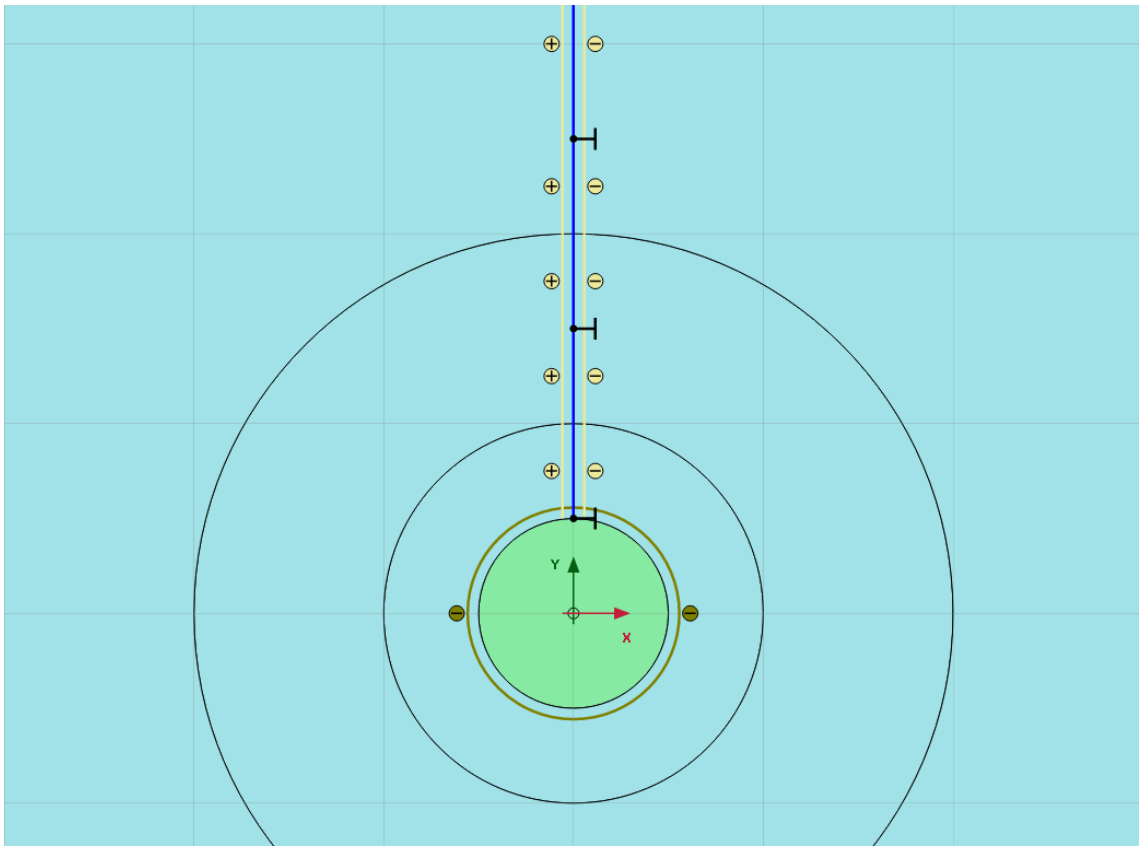

Figure 50 - Pile model in plane strain conditions -Plaxis 2D

5.5.2. Imposed vertical displacement with pile

A series of analysis have been carried out by considering the plate end section in contact with the flint and by imposing a vertical displacement at the plate top, able to produce a complete failure in the soil. For each selected flint geometry, ten different contact point have been explored; in each analysis, the vertical and horizontal forces that arise at the contact point between the flint and the pile wall were calculated. The vertical forces have been obtained through the load-displacement curves by evaluating the value reached by

the force once a plastic displacement is obtained. Regarding the horizontal forces acting on the pile tip, the values have been obtained by reading the reacting force of the spring of the fixed-end anchors inserted at the plate end section

A set of analyses have been performed by considering the circular stiffness of the pile, as previously evaluated (see §5.5.1).

Figure 51 and Figure 52 show how, due to pile wall presence, the resulting flow mechanism differ from the simple rotational "Martin" mechanism (Martin & Randolph, 2006) observed by imposing a simple vertical displacement to the flint, leading to a reduction of the forces at the contact point.

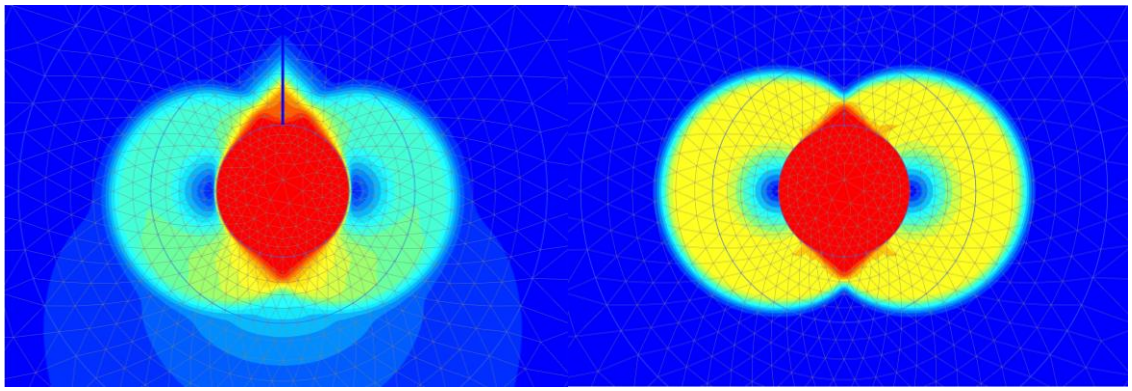

Figure 51 - Comparison of the flow mechanism with and without pile - centered contact point

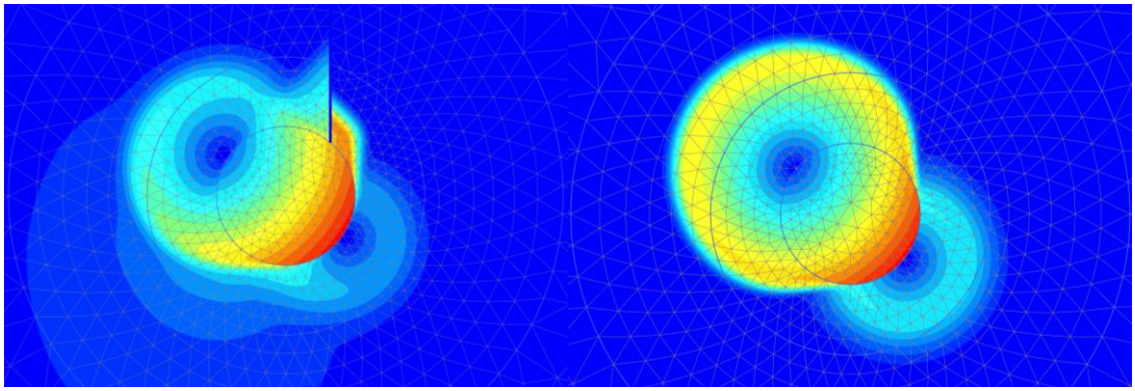

Figure 52 - Comparison of the flow mechanism with and without pile - lateral contact point

A comparison with the results obtained by applying only a vertical displacement is presented in Figure 53, in terms of normalized vertical and horizontal forces in function of the normalized distance of the contact point from the flint centre. By comparing the results with the ones obtained by imposing a simple vertical displacement to the flint, it is possible to notice that comparable trends are obtained. The main difference is represented by a reduction of the horizontal forces in presence of the pile wall.

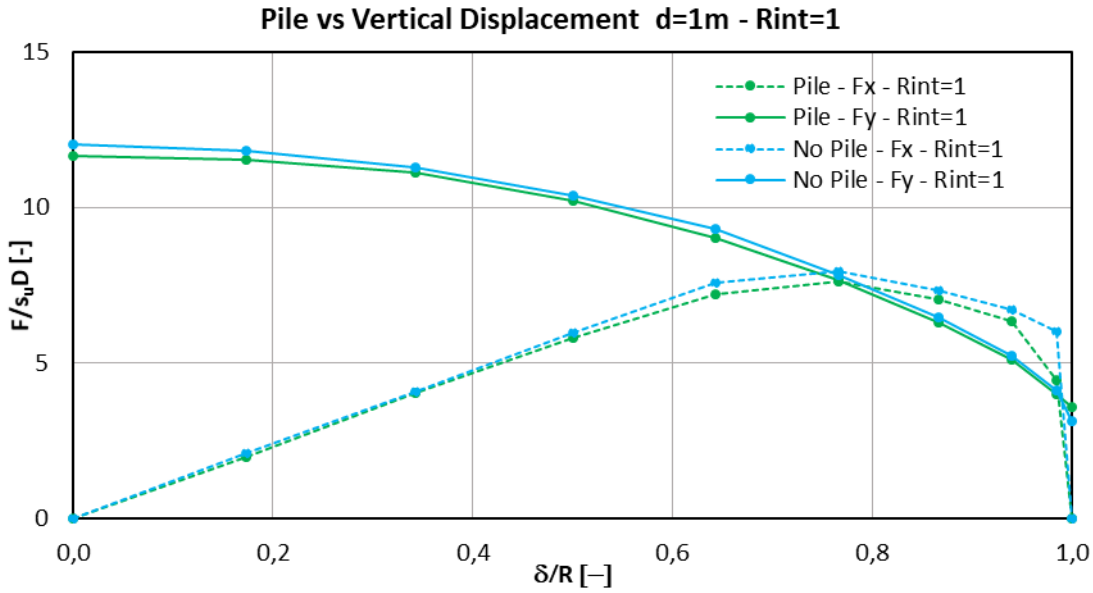

Figure 53 – Circular flint – Influence of the pile presence

As previously described (§5.5), this reduction can be attributed to the pile wall presence and the pile circular stiffness. In particularly the presence of the pile wall modifies the soil flow around the flint, leading to a reduction of the vertical forces, while the reduction of the horizontal forces is due to the horizontal deformability of the plate in the model, whose allowed displacement is governed by the stiffness of the spring of the fixed-end anchor at the pile tip.

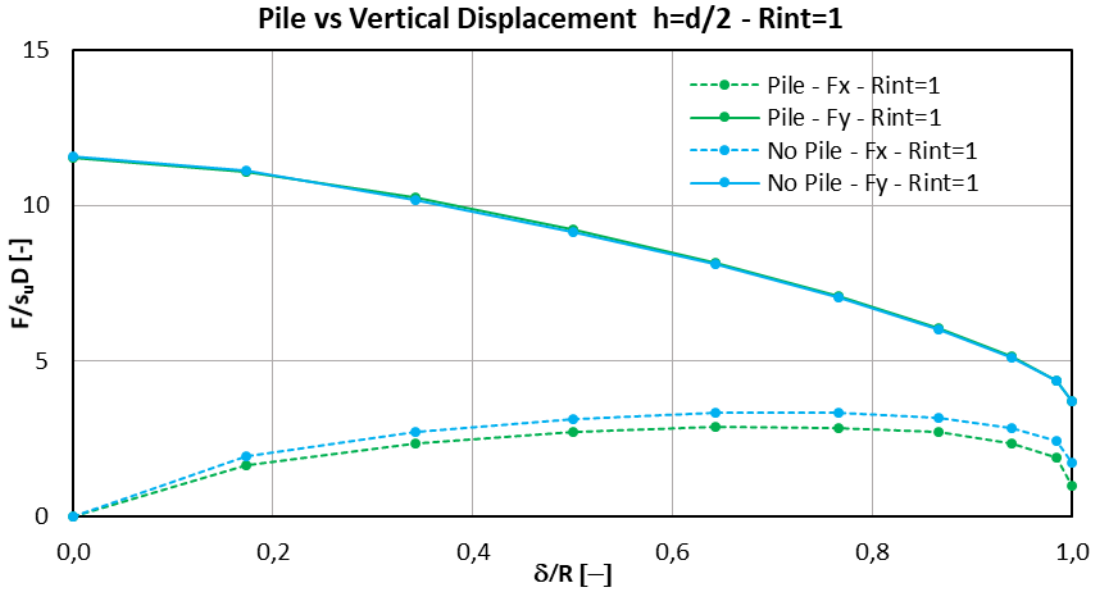

Figure 54 - Ellipsoidal flint h=d/2 - Influence of the pile presence

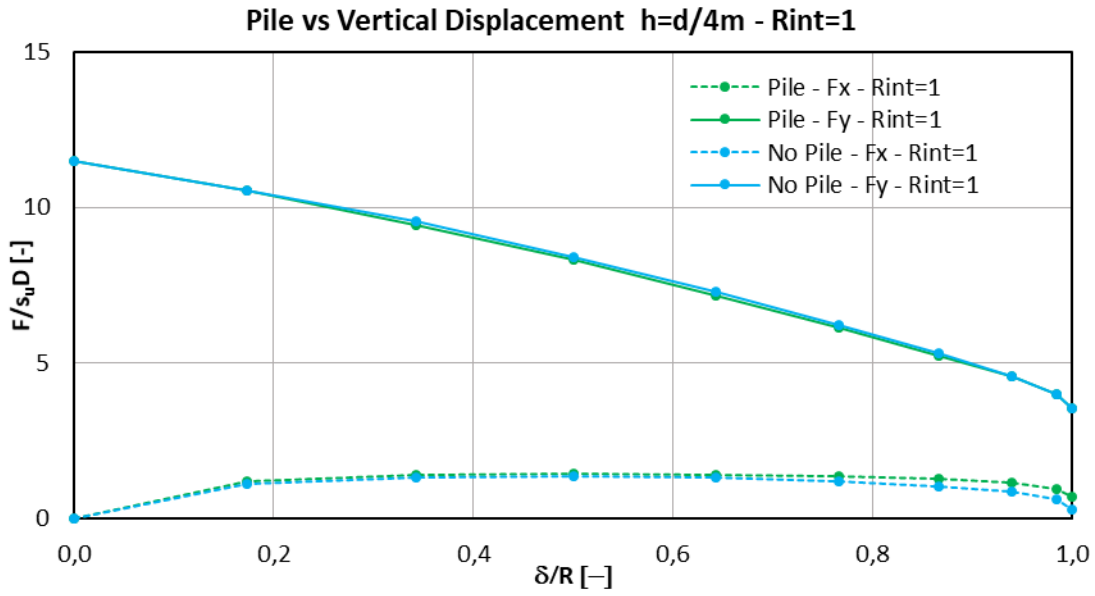

Figure 55 - Ellipsoidal flint h=d/4 - Influence of the pile presence

Same analyses have been performed on ellipsoidal, leading to the same conclusions. The results are showed in Figure 54 and Figure 55.

The obtained results indicate that for the selected pile D and D/t, the effect of the pile deformability is not paramount. Therefore, for the dynamical analysis, the numerical model is not able to reproduce properly the phenomenon. In fact, pile and flint results linked through the contact point. This led to a resistance of the inertial forces of the flint after the impact. These reason lead to the decision to avoid the modelling of the pile in the more complex dynamical analysis, modelling only its radial stiffness.

6. Dynamic 2D FEA analysis

6.1. Introduction

During pile driving, when the hammer hits the pile top, a compression wave is produced, which travels along the pile, reaches the pile toe where it is reflected and after travels back upward. If a flint or a boulder is encountered, the compression wave will be transmitted at the contact point, producing a dynamic motion of the obstruction within the soil. The presence of the flint lead to a local increase of the force at the contact point, which could trigger the pile tip buckling phenomenon.

In order to investigate this complex phenomenon, dynamic numerical analyses have been carried out with the aim of evaluating the magnitude of the force needed to plastically displace the obstruction within the soil.

Moreover, it is important to notice that pile driving operations produce ground vibrations which propagates from the pile through the surrounding soil. In order to properly model the dynamical behavior of the embedded flint and soil damping effects, a special emphasis has been reserved to the wave propagations through the model.

In this thesis, these mechanisms will be explored using dynamic finite element analyses performed by means of the PLAXIS 2D Dynamic module.

The most relevant aspects of the dynamic model, described in detail in the following sections, can be summarized as follow:

- definition of appropriate geometry and mesh;
- definition of the soil properties and soil damping parameters able to describe the wave propagation through the model;
- evaluation of the input load transmitted by the pile tip to the obstruction, obtained by means of a driveability analysis.

Results are obtained in terms of developed forces at the pile-flint contact point and plastic displacement of the flint.

6.2. Soil behaviour during pile driving

6.2.1. Wave propagation during pile driving

During pile driving, when the hammer impacts the pile head, a stress is created that propagates along the pile and across the embedding soil.

The main aspects of the vibration propagation during pile driving can be summarized in the following points:

- Wave propagation in the pile
- Pile-soil interaction
- Wave propagation in the soil

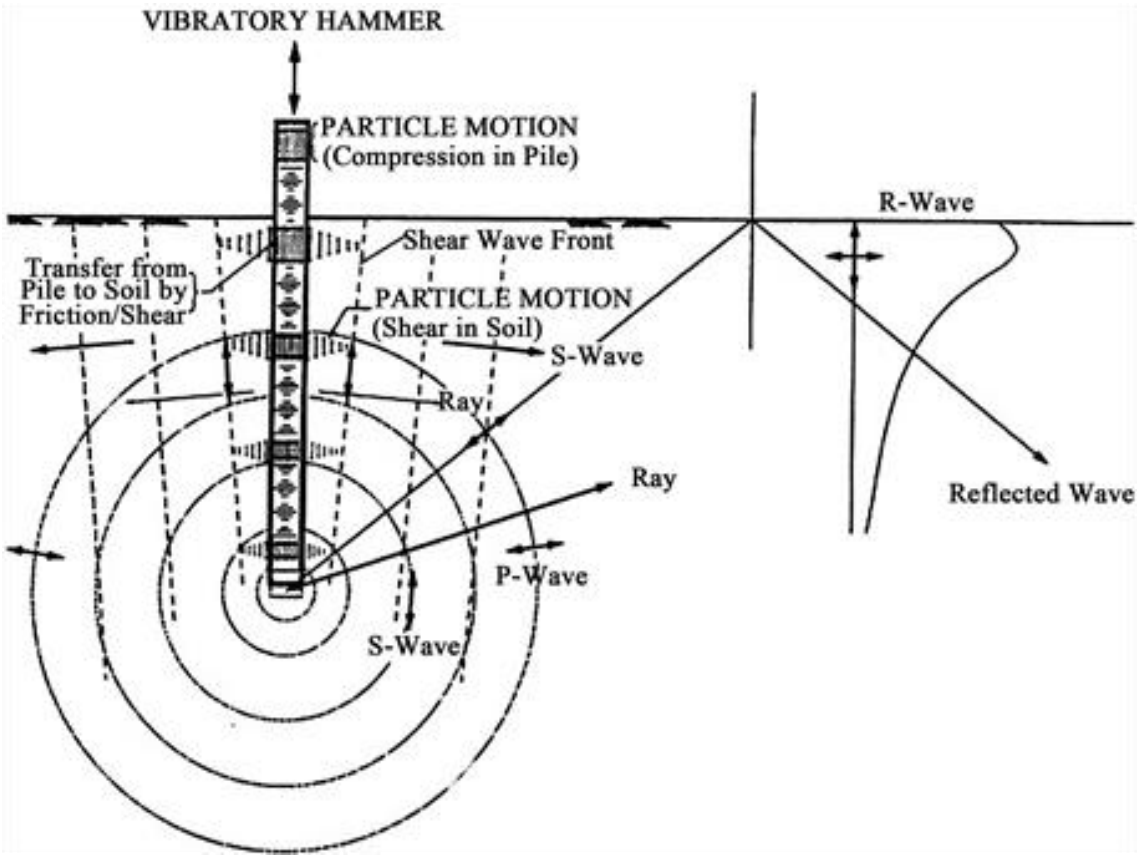

Figure 56 - Waves generated during pile driving (Athanasopoulos & Pelekis, 2000)

In particular, when the hammer impacts the pile, energy is transferred along the pile body in a form of compressional wave.

Along the pile shaft, shear waves (S-waves) are produced due to pile-soil interaction, which propagate conically through the embedding soil.

Once the compression waves induced by the hammer reach the pile toe, compressional wave (P-waves) and S-waves are generated. The waves propagate in the soil from the pile toe in all direction with spherical wave front.

Finally, when these waves reach the surface, due to wave refraction part of them are converted in surface waves, known as Rayleigh waves (R-waves), which conically propagate, involving a depth approximately equal to the wavelength.

Many studies are present in literature about wave propagation at low strain, nevertheless only limited information are available about dynamic pile-soil interaction which is characterized by large strain level.

Empirical methods based on the transferred power by the hammer are widely used to evaluate ground vibrations. However, these energy-based methods are limited by the assumption that wave propagation is only depending on the hammer energy, leaving out fundamental aspects like the soil mechanical behavior.

Indeed, during the driving phase, the generation of the three type of waves previously introduced depend on the velocity-dependent soil resistance at the pile soil interface (Massarch & Fellenius, 2008).

Thus, the ground vibrations depend on type and source of emission, influenced by hammer energy, pile properties and the pile-soil interaction, and on the wave attenuation with distance, influenced by geometric and material damping.

6.2.2. Waves attenuation

During pile impact driving, due to the dynamic force that develop along the pile-soil interface, energy is transmitted to the surrounding soil in the form of stress waves, which propagate into the surrounding soil. The amplitude of the waves is then progressively reduced with distance due to damping.

Attenuation of the stress waves in soil dynamic involves several mechanisms which contribute to the energy dissipation., which can be mainly divided in two phenomena:

- Radiation damping;
- Material damping.

Radiation damping, also known as geometric damping, is a reduction of the amplitude of the induced stress waves due to a spread of the wave energy over a larger volume. Therefore, the attenuation is directly related to the wave front of the induced waves. Indeed, given a certain distance, waves characterized by a spherical wave front, as the waves produced at the base during pile driving, are subjected to a larger radiation damping with respect to the R-wave, characterized by a cylindrical wave front.

Material damping consists in an energy dissipation due to physical mechanism within the soil, like friction between the soil particles, viscous behavior of the soil and development of plastic deformations.

For numerical purposes, material damping is frequently introduced through the Rayleigh formulation, which allows to consider damping in soil model whose plastic strain is not enough to model the damping characteristics of the real soil. According to this method, damping is introduced in the dynamic equations through the damping matric C, obtained as a linear combination of the mass matrix M and the stiffness matrix K.

$$[C] = \alpha[M] + \beta[K] \qquad \text{Equation 11}$$

where α and β represent the Rayleigh coefficients, which represent respectively the influence of the mass and the stiffness in the damping of the soil. High values of a reflects a larger damping of the lower frequencies while high values of b produce the damping of the high frequencies.

The two coefficients result linked through the damping ratio ξ_j by means of the following relationship:

$$\xi_j = \frac{1}{2}\left(\frac{\alpha}{\omega_j} + \beta\omega_j\right) \qquad \text{Equation 12}$$

The Rayleigh coefficients can be evaluated by assigning same value of the damping ratio for two difference frequencies:

$$\alpha = \frac{2\xi}{\omega_m + \omega_n}\omega_m\omega_n \qquad \text{Equation 13}$$

$$\beta = \frac{2\xi}{\omega_m + \omega_n} \qquad \text{Equation 14}$$

Based on these equations, by combining Equation 12 with Equation 13 and Equation 14, it is possible to evaluate as the damping ratio varies with the frequency.

$$\xi_j = \frac{2\xi^*}{\omega_m + \omega_n}\left(\frac{\omega_m \omega_n}{2\omega_j} + \frac{\omega_j}{2}\right) \qquad \text{Equation 15}$$

The obtained function provides a damping equal or less than the target damping ratio within the target frequency interval, whereas outside this interval a bigger damping is provide it.

Several methods are presents in literature to evaluate the target frequencies. One of the most applied is the method suggested by Amorosi et al. (Amorosi, et al., 2010) where the target frequencies are obtained as the frequency interval characterized by the highest energy content, evaluated on the base of the Fourier spectrum.

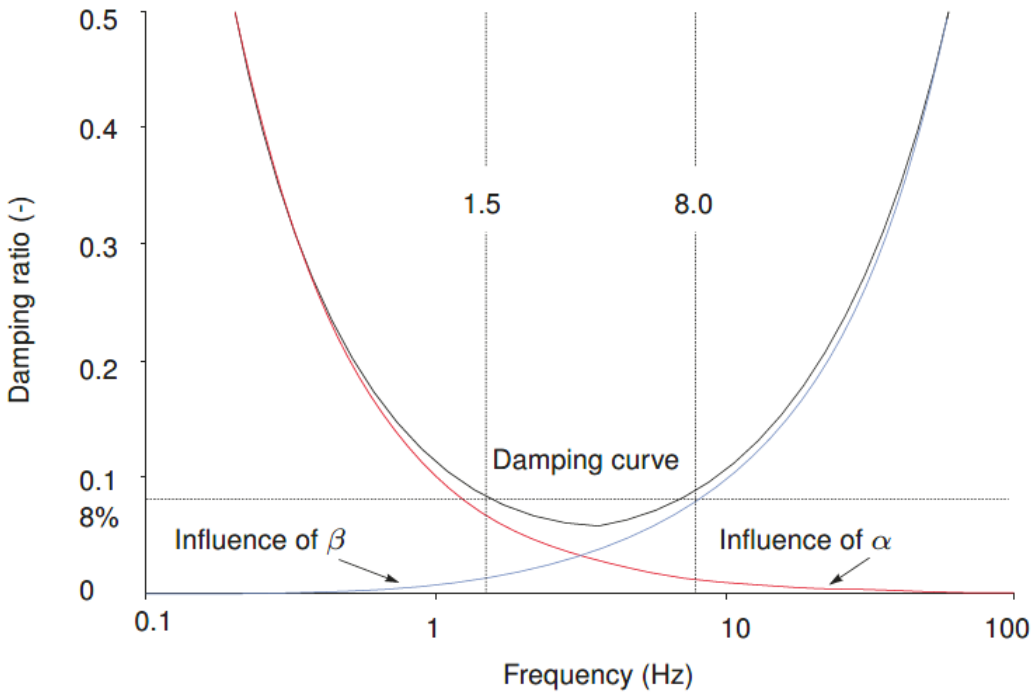

Figure 57 - Rayleigh damping parameters influence

Another form of damping introduced in the numerical models is the numerical damping, introduced in the model to reduce the so-called numerical noise, produced by the high frequency mode originated by the direct integration of the equilibrium equations.

In PLAXIS dynamic problems are solved through the implicit Newmark scheme, in which the numerical damping is governed by the parameters α_N and β_N, which can be expressed as follow:

$$\beta_N \geq \frac{1}{2} \qquad \text{Equation 16}$$

$$\alpha_N = \frac{1}{4}\left(\frac{1}{2} + \beta\right)^2 \qquad \text{Equation 17}$$

Numerical damping is imposed to the model when the parameters is β_N larger than ½, while α_N produces a dissipation of the high frequencies.

Finally, in order to allow the model to reduce the real infinite domain into a finite domain, in a dynamic numerical model viscous boundary should be set. This type of boundaries adsorbs the outgoing energy propagate through the model in dynamic analysis, avoiding wave reflection inside the soil.

Viscous boundaries have been introduced by Lysmer & Kuhlmeyer (Lysmer & Kuhlemeyer, 1969) and consist in a series of dashpot distributed horizontally and vertically along the borders. This solution is suitable for problem where the dynamic source is within the model. This method is implemented in PLAXIS and need the definition of the relaxation coefficients C1 and C2. According to the authors, based on a study in which the ratio between the reflected and impacted waves on the boundaries, values of C1=1 and C2=0.25 produce a nonreflecting condition.

6.3. Dynamic numerical model

6.3.1. Geometry and Mesh

Dynamic analyses have been carried out by considering three different flint shapes: one circular and two ellipsoidal. As for the finite element static analyses (see §5.2.1), the horizontal axis of the ellipsoidal flints has been set equal to the circular flint diameter while the vertical axis have been chosen equal to half (Ellipsoidal 1) and a quarter (Ellipsoidal 2) the horizontal ones.

For each selected flint shape, two different sizes have been explored, by considering the horizontal axis equal to 0.2m and 1m. Figure 58 shows the three different flint geometries

analysed. The sizes of the flint have been chosen with the aim of cover the flint dimension range most probably encountered in a layer of grade D white chalk. Flint larger than 1m have been found in chalk deposit but occur only in specific locations. An example is represented by the Paramoundra flints, very large flints (can be more then 2m in diameter), observed in the Paramoundra Chalk of Norfolk and Northen Ireland or in the Bedwell's Columnar Flint in Southern England (Lord, et al., 2002).

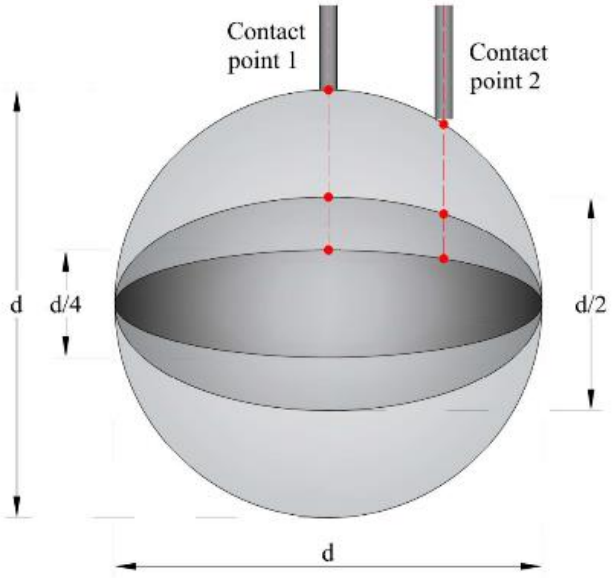

Figure 58 – Adopted model for dynamical analyses

Flints have been modelled at the centre of a square model, whose dimensions have been chosen in function of the flint size. The size of the model should be large enough to avoid potential influences by the boundary restraints. At the same time the model size should be reduced as much as possible to reduce the high computational time of the dynamic finite element analysis. By performing a sensitivity analysis on the model size, a good compromise has been obtained by setting the side of the model equal to 20 times the flint major axis size, which allows to obtain results not affected by the boundary restraints.

To allow a relative displacement between the flint and the embedding soil, an interface with a Rint=1 parameter has been added to the model.

In order to perform accurate finite element calculation, the mesh should be sufficiently fine. On the other hand, a very fine mesh could lead to excessive calculation time. Moreover, in order to obtain accurate results in dynamic analysis, the size of the mesh

elements should be chosen carefully, in function of the characteristics of the soil and the dynamic input signal. A study on the mesh element size influence on dynamic calculations has been conducted by Kuhlmeyer & Lysmer (Kuhlemeyer & Lysmer, 1973), who suggested to assume an element size not larger than λ/10, where λ is the wavelength corresponding to the maximum frequency of the input signal. To evaluate the frequency content of the impact force, a Fourier transform has been performed on the time history of the input signal. Figure 59 shows as the signal is mostly dominated by frequency between 0 and 300Hz.

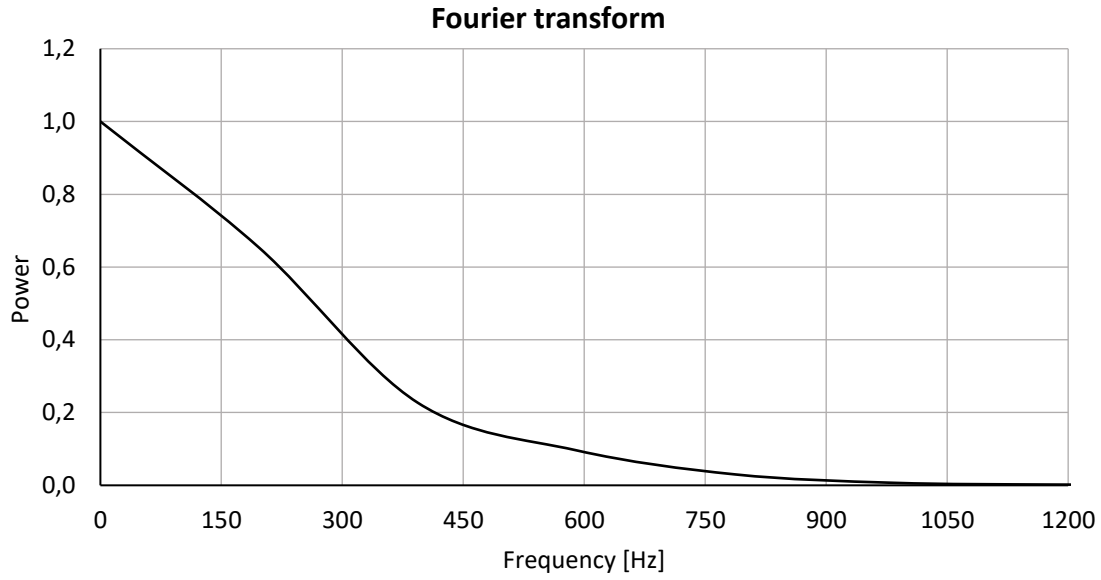

Figure 59 - Fourier transform of the impact load

The corresponding wavelength generated on the model by means of the following relationship:

$$\lambda = \frac{V_S}{f} \qquad \text{Equation 18}$$

where V_s is the shear wave velocity, and could be obtained as function of the shear modulus and the density of the soil:

$$V_s = \sqrt{\left(\frac{G}{\rho}\right)} \qquad \text{Equation 19}$$

Therefore, the mesh element size could be obtained as:

$$element\ size = \frac{\lambda}{10} = \frac{V_s}{10\ f_{max}} \qquad \text{Equation 20}$$

Three different soil parameters have been used to model the embedding chalk. According to Equation 20, the maximum element size should be evaluated by using the shear wave velocity of the less stiff material adopted in the analysis. Being the minimum shear wave velocity equal to 150 m/s, a mesh element size of 5cm has been obtained.

In PLAXIS 2D, 15-Node triangular elements have been adopted to discretize the model. The mesh generator requires a global meshing parameter that represents the target element size, l_e. This parameter is calculated as function of the whole model dimension through the following relation:

$$l_e = r_e \times 0.06 \times \sqrt{[(x_{max} - x_{min})^2 + (y_{max} - y_{min})^2]} \qquad \text{Equation 21}$$

where:

- x_{max}, x_{min}, y_{max} and y_{min}, are the outer geometry coordinates;
- r_e, is the relative element size factor.

By setting the relative element size factor equal to 1, corresponding to a Medium Element distribution, it is possible to obtain the required element size by applying local refinement to the model through the Coarseness factor. This command allows more accurate finite element mesh where large stress concentration or large deformation gradients are expected. Since the static analysis showed as the failure mechanism involve an area around the flint of approximately 1.5 times the flint diameter, by setting a series of polycurves, it was possible to refine the mesh around the flint for a length of 2 times the diameters. Taking into account the Coarseness factor, the mesh element size can be controlled through the following relationship:

$$l_e = Cors.Fact. \times r_e \times 0.06 \times \sqrt{[(x_{max} - x_{min})^2 + (y_{max} - y_{min})^2]} \qquad \text{Equation 22}$$

Table 4 summarizes the model dimensions adopted for each flint geometries and the corresponding relative element size factor that allowed to obtain a mesh element size of 5cm.

Table 4 – Models dimensions and relative element size factor

	Model 1 (4x4m)	**Model 2 (10x10m)**
$\mathbf{r_e}$	0.11	0.02

Figure 60 shows the final mesh obtained for the dynamic calculations.

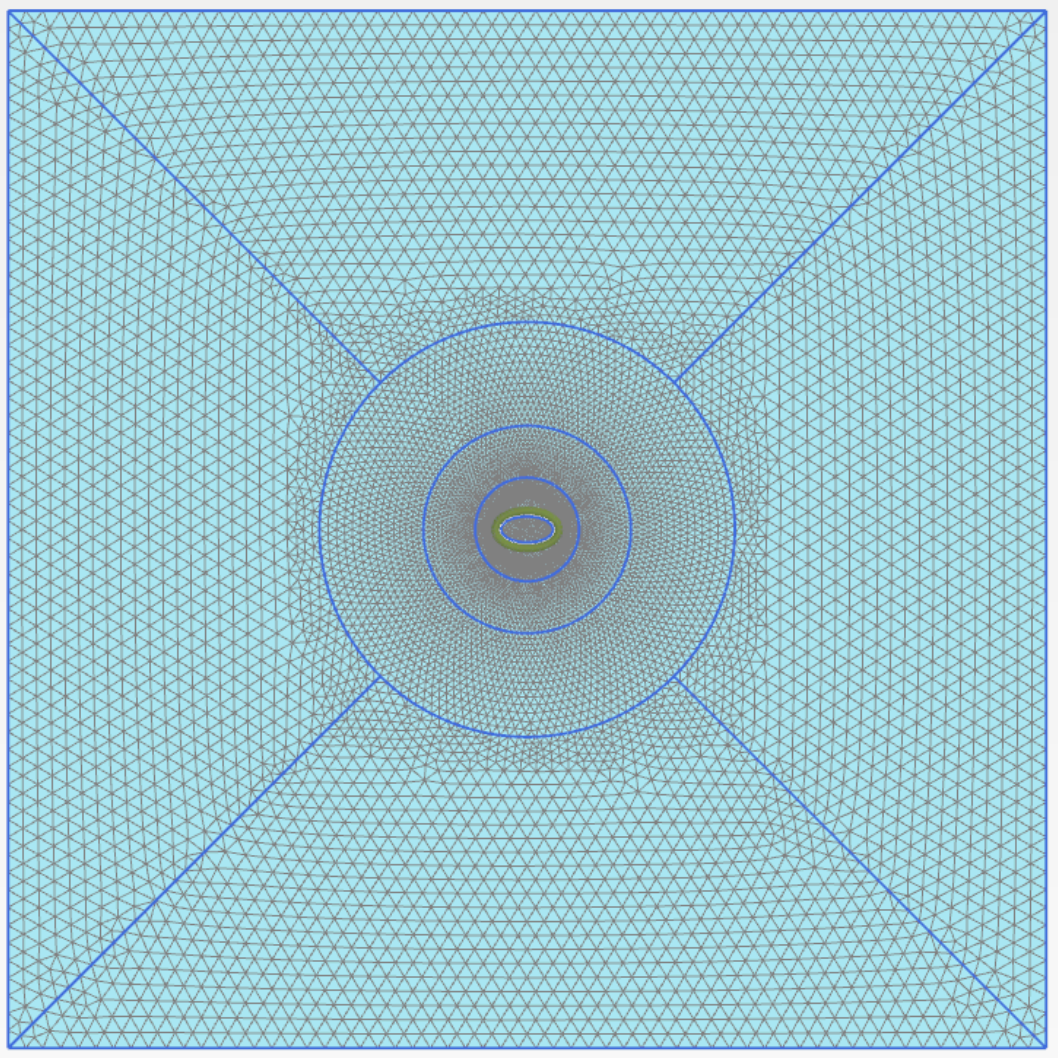

Figure 60 - Dyanamic analyses mesh

6.3.2. Material properties

The material adopted in the dynamic analyses is a chalk characterized by low density and high porosity, typically encountered in the shallow weathered layer of the white chalk deposit in the North Sea.

The soil has been modelled in PLAXIS with a Mohr Coulomb. During pile driving in chalk the high frequency of the load lead to pore pressure increment around the pile shaft. After the driving pore pressure are rapidly dissipated due to the high porosity of the material. The same behavior can be assumed between flint and the embedding chalk. To evaluate this undrained conditions, Undrained C feature has been selected in PLAXIS. In this type of model, the analysis is carried out by considering the total stress acting in the model, with all the other parameters specified as undrained. The advantage of this model is the lack of distinction between effective stress and pore pressure. However, this value are not of interest for the present study.

The following parameters are required in the model:

- soil unit weight;
- undrained shear resistance;
- undrained Poisson's ratio;
- undrained Young's modulus;

Regarding the soil density, being the modelled phenomena occurring under the seabed during offshore pile installation, the saturated unit weight has been considered.

Three type of chalk has been considered, whose saturated unit weight is reported Table 5.

Table 5 - Saturated unit weight

	Chalk 1	**Chalk 2**	**Chalk 3**
γ_{sat} [kN/m^3]	18.5	19.0	19.5

Regarding the undrained shear strength, after a literature review and based on internal experience in Cathie Associates, it was found that this type of material can show values

ranging between 100kPa and 1000kPa. As reported in Section 2.1.4 a typical ratio of 1000 is usually show between the undrained Young's modulus and the undrained shear strength. The assumed values of these parameters are reported in Table 6.

Table 6 - Undrained shear resistance and Young's modulus

	Chalk 1	**Chalk 2**	**Chalk 3**
S_u [kPa]	100	500	1000
E_u [GPa]	0.1	0.5	1

A fundamental parameter in the proposed model is the undrained Poisson's ratio, due to its high influence in the waves propagation through the model. In fact, in the analysis the compressibility of the water and the soil porosity is not considered, leading to unrealistic high wave velocity. This means that the values should be assumed as much as possible higher to produce plausible wave velocity.

According to Masson (1973) P-wave velocity in chalk range between 1300 m/s and 2800 m/s. However, being in saturated conditions, P-wave velocity can not be lower than 1500 m/s.

In elastic conditions, P-waves can be expressed as:

$$V_P = \sqrt{\frac{E_{oed,u}}{\rho}} \qquad \text{Equation 23}$$

where the oedometric elastic modulus can be expressed as function of the Young's modulus and the Poisson's ratio as follow:

$$E_{oed,u} = E_u \frac{1 - \nu_u}{(1 + \nu_u)(1 - 2\nu_u)} \qquad \text{Equation 24}$$

By using the presented relationship, the following values of Poisson's ratio able to produce reasonable values of wave velocity have been evaluated.

Table 7 - Undrained Poisson's ratio and wave velocity

	Chalk 1	**Chalk 2**	**Chalk 3**
υ_u [-]	0.496	0.49	0.485
V_P [m/s]	1688	2366	2705

6.3.3. Impact force

In order to analyze the dynamic response of a pile during the driving the force-time signal generated by the impact of the hammer is required. As previously described (§4.2.2), in the design phase driveability analyses are performed to evaluate the proper hammer in function of the soil and pile characteristics, in order to obtain a safe installation (without damage), economically (lowest blow/rate) and reach the required penetration (bearing capacity). The pile response is evaluated by means of numerical solution of the wave propagation of a wave in a one-dimensional element. The pile is modelled as an elastic nondimensional element connected through springs and dashpot to the surrounding soil in order to model the pile soil interaction.

During pile driving, when the hammer hit the pile, a compression wave is generated which travel along the pile at a speed equal to 5122 m/s for the steel.

When the wave reaches the pile at t_1=l/c is reflected and subsequently travel upward until reach the pile top at t_2=2l/c.

With the aim of investigating the dynamical behavior of an encountered flint during pile driving the evaluation of the dynamic force transmitted by the pile to the flint is crucial.

A driveability analysis have been carried out by using the commercial software GRLWEAP (Goble & Rausche, 1999).

A drivability analysis requires the following input data:

- unit shaft resistance;
- unit toe resistance;
- pile properties;

- selected hammer properties;
- quake and damping parameters.

Unit and toe soil resistance have been evaluated by considering an undrained shear resistance S_u=100kPa and by following the API recommendations (API, 2011):

- unit shaft resistance $f_s = \alpha\, S_u = 50kPa$, where $\alpha = 0.5$ per $S_u < 72kPa$;
- unit toe resistance $q_t = 9\, S_u = 900kPa$

Regarding the pile properties, an 8m diameter pile has been chosen with a length of 60m and a penetration target of 30m, typical depth adopted for an offshore monopile installed in shallow water. Regarding the thickness it has been evaluated by means of the API recommendations:

$$t = 6.35 + \frac{D}{100} = 86.5mm \qquad \text{Equation 25}$$

The hammer selection has been done based on previous experience of large monopile driving within Cathie Associates. The chosen hammer is the Menck MHU 2100S hydraulic.

Regarding quake and damping parameter, a value of 0.25s/m and 0.5s/m have been selected for respectively side and toe damping, while a value of 2.5mm has been selected for both side and toe quake.

Figure 61 shows a screenshot of the input window in GRLWEAP.

The obtained signal has been decomposed in the Top (Figure 62) and Bottom forces (Figure 63).

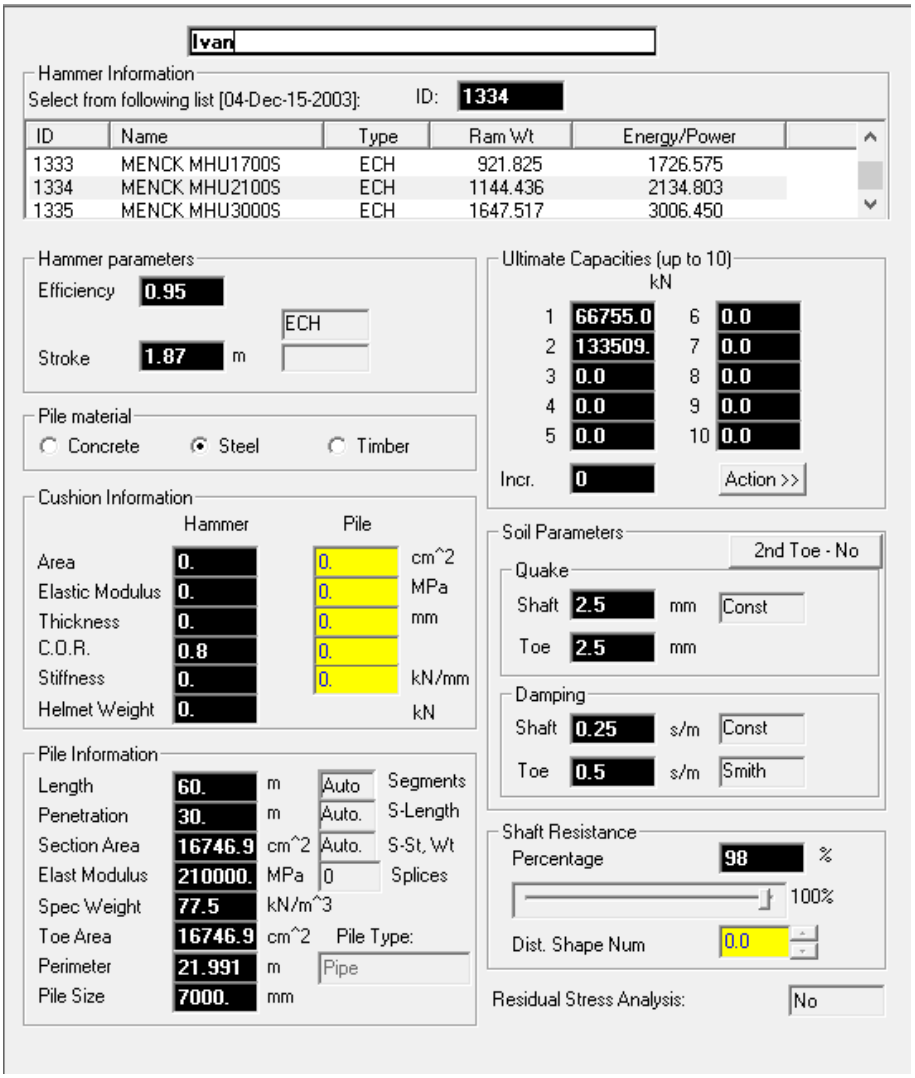

Figure 61 - GRLWEAP input parameters

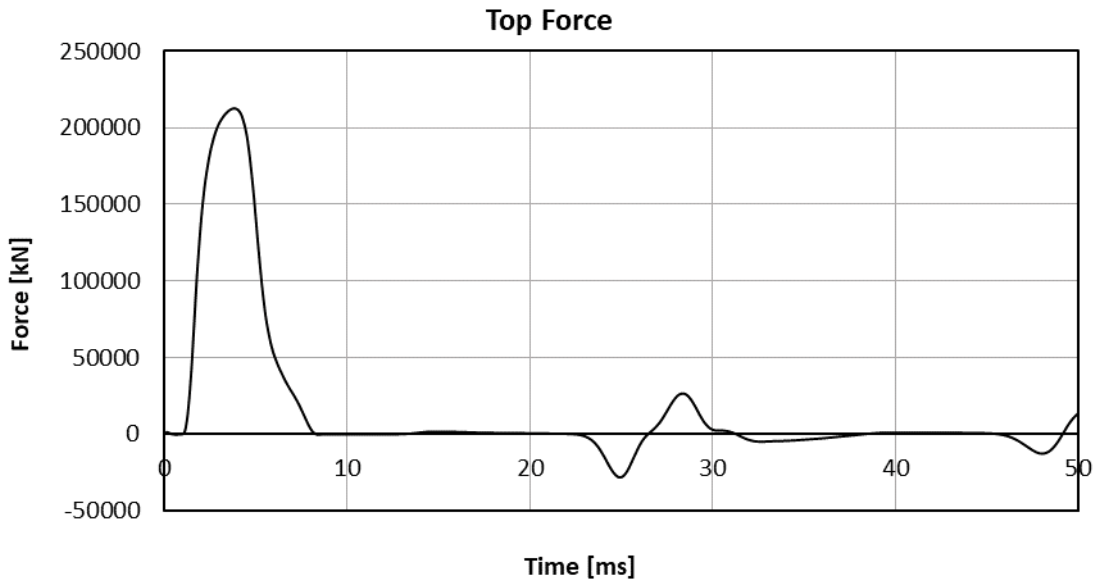

Figure 62 - Top Force

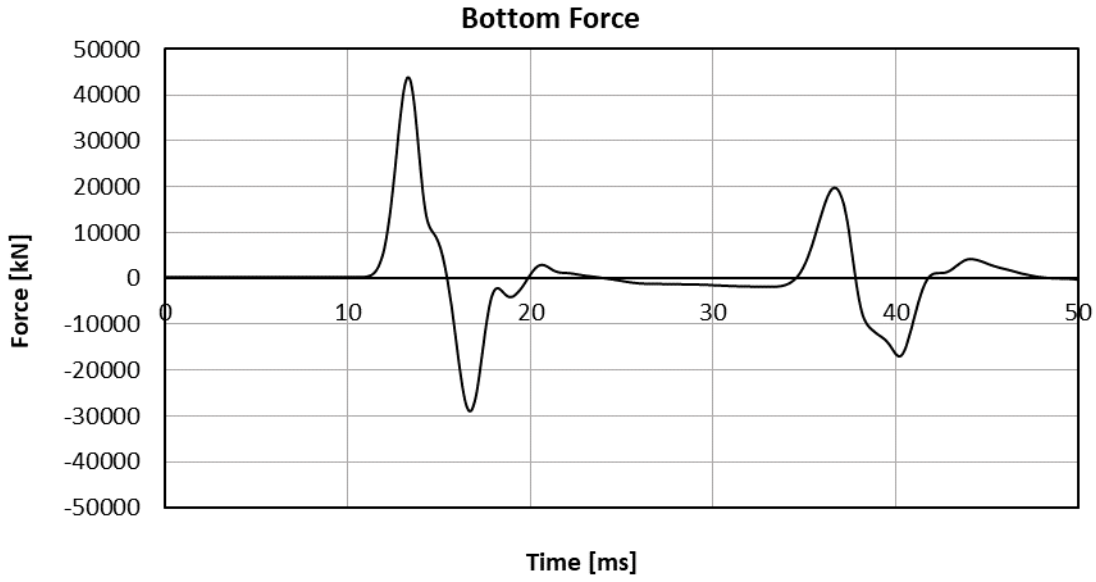

Figure 63 - Bottom force

Finally, to obtain the dynamic force the first part of the bottom force has been considered, which correspond to the force that arrive at the pile top prior to its reflection, which result influenced by the impedance at the pile top.

Figure 64 show the normalized bottom force used ad input dynamic multiplier in PLAXIS.

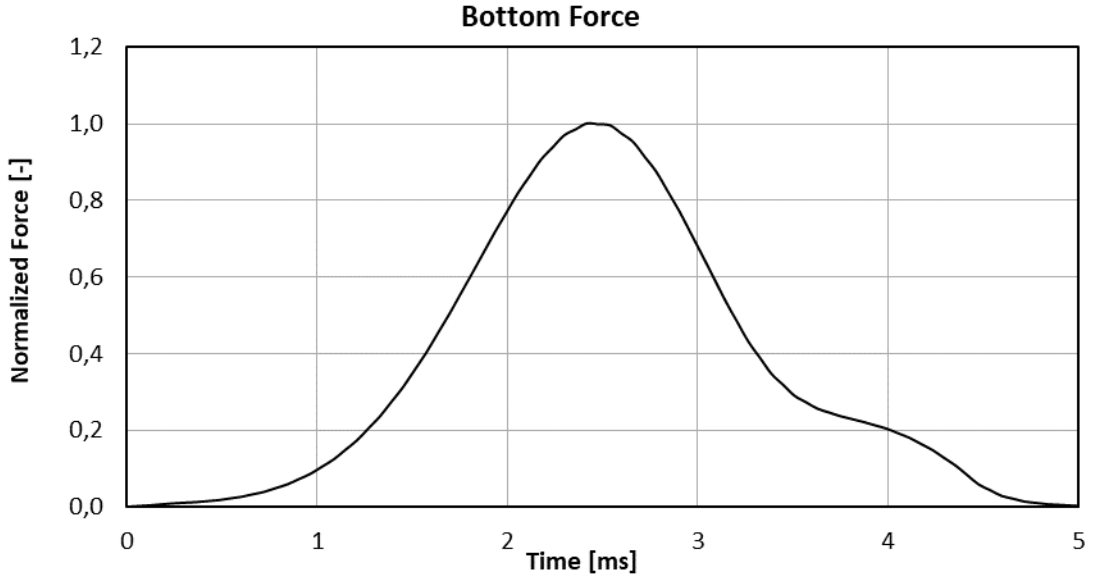

Figure 64 - Normalized bottom force

6.3.4. Damping parameters

During pile driving cyclic stresses are induced in the surrounding soil. As previously described in Section 6.2.1, the source and the entity of the vibrations are related to the soil-pile interface. In the studied phenomenon an additional source is represented by the boulder. After the impact the obstruction start to oscillate within the ground, producing P-waves and S-waves which spherically propagate through the soil.

In order to properly model the resulting ground vibration, a special focus should be made on damping effects. The adopted Mohr-Coulomb soil model, may generate plastic strain if the stress points reach the failure criteria, leading to damping in the dynamic calculation. However, it is important to be noted that cyclic stress within the failure criteria will only generate elastic strain and no material damping and strains accumulation can be considered (PLAXIS, 2018). The latter can be introduced in the model by means of the frequency-dependent Rayleigh coefficients, whose selection has been made based on the literature review presented in Section 6.2.2.

In particular, the calibration of these parameters has been made according the method proposed by Amorosi et al. (Amorosi, et al., 2010), who suggests to select the two target frequencies by defining the interval characterized by the highest energy content.

To evaluate the energy content of the vibration induced through the model, the following approach has been applied.

A dynamic impact force has been applied on the flint, in order to produce an elastic strain followed by a vibration of the flint on the embedding soil. The obstruction vibration produces the propagation of waves across the soil, which has modelled without Rayleigh damping.

Time-velocity curves have been evaluated for 4 different points selected between the flint and the boundary (Figure 65).

The free oscillation after the impact has been isolated for each monitored point. In order to highlight how the signal energy is spread among the frequencies a Fast Fourier Transform has been performed on the obtained data. This allowed to evaluate the power spectrum for each selected point, which describes how the energy of the vibrations is spread among the frequencies.

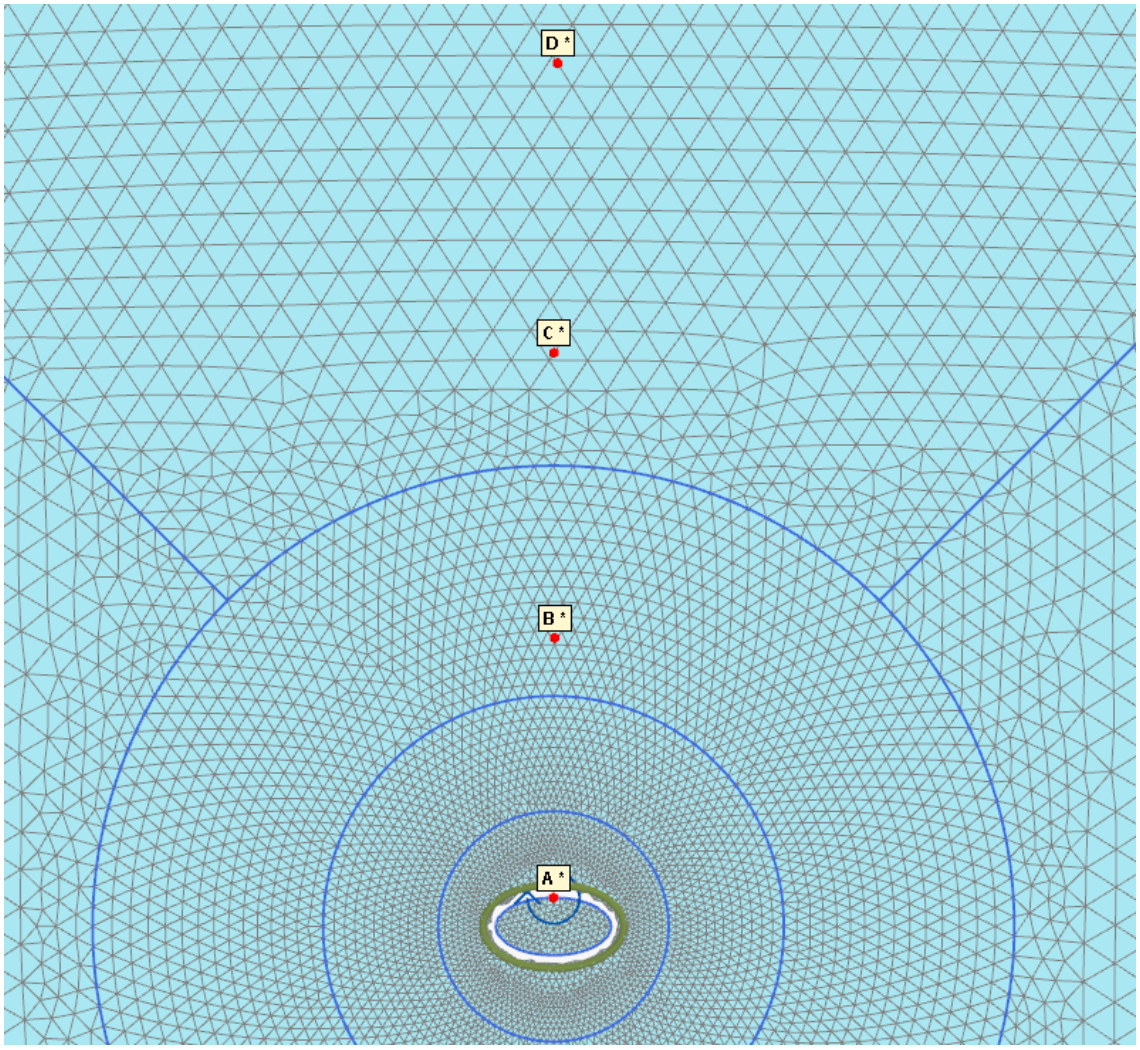

Figure 65 - Selected points for the evaluation of the power velocity spectrums

In this study, the energy is diffused through the model by the flint, which represents the source of the vibrations. Different shapes and different size of the flint produce different ground vibrations through the model. At the same time, the propagation of the waves is influenced by the soil stiffness of the embedding chalk.

Thus, by considering 3 different flint shapes, 2 dimensions and 3 different soil parameters, a total number of 18 numerical analyses have been carried out to evaluate the Rayleigh parameters.

Figure 66, Figure 67 and Figure 68 highlight the influence of the soil stiffness in the vibration propagation through the model produced by the oscillation of a circular flint with a diameter of 1m. By comparing the obtained plots, it is possible to notice how the more the stiffness of the embedding soil is increased the more the signal induced through the model is characterized by higher frequencies.

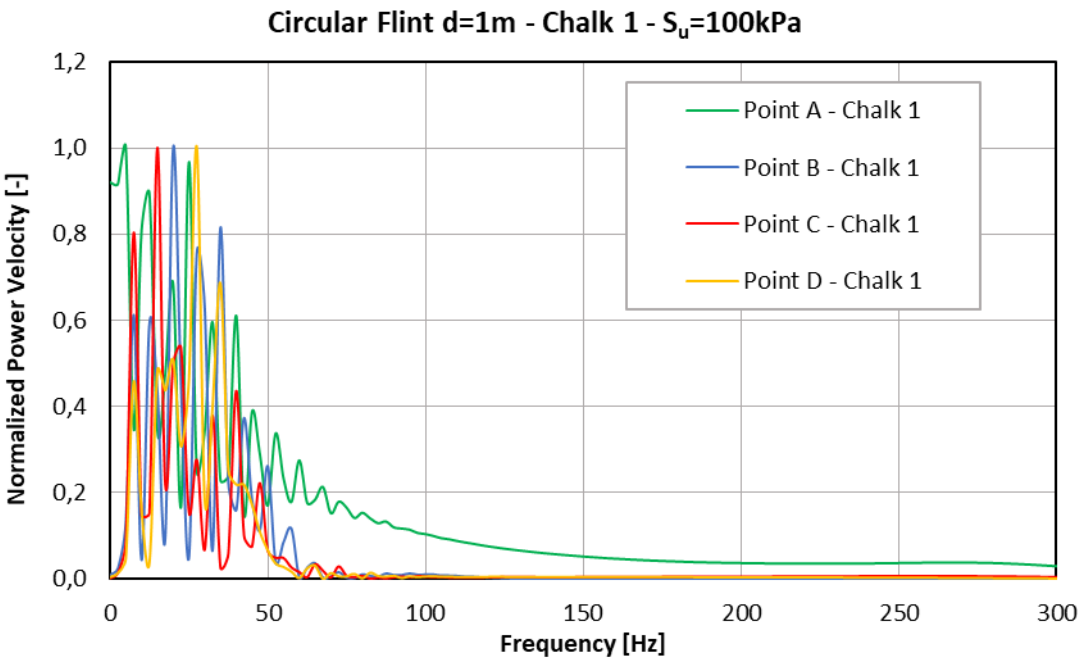

Figure 66 - Normalized Power Velocity - Circular flint d=1m - Chalk 1

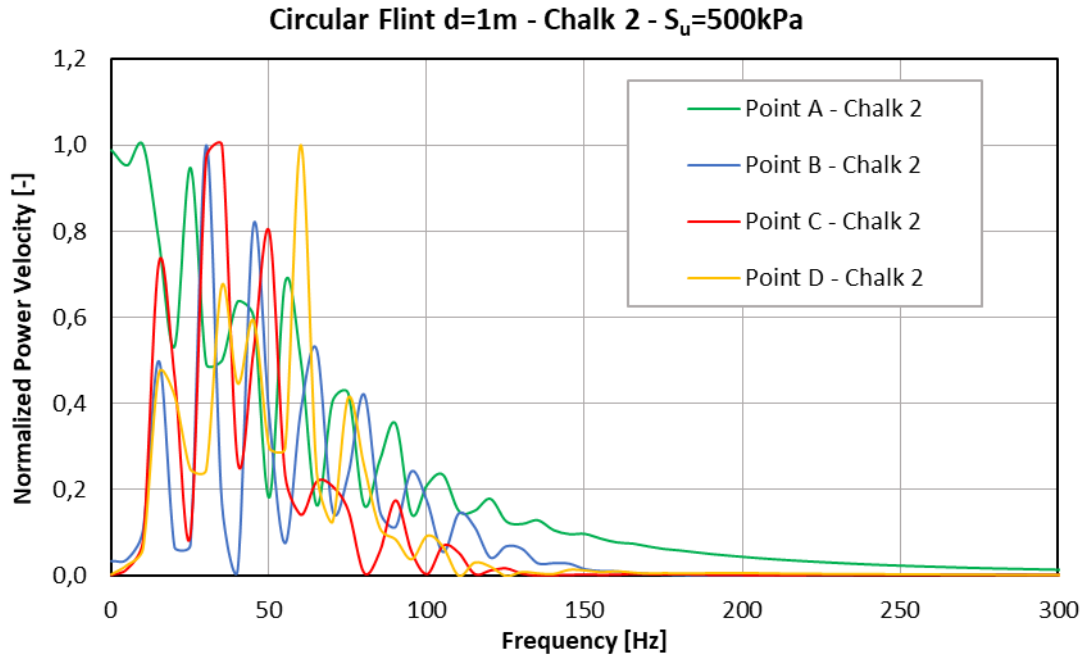

Figure 67 - Normalized Power Velocity - Circular flint d=1m - Chalk 2

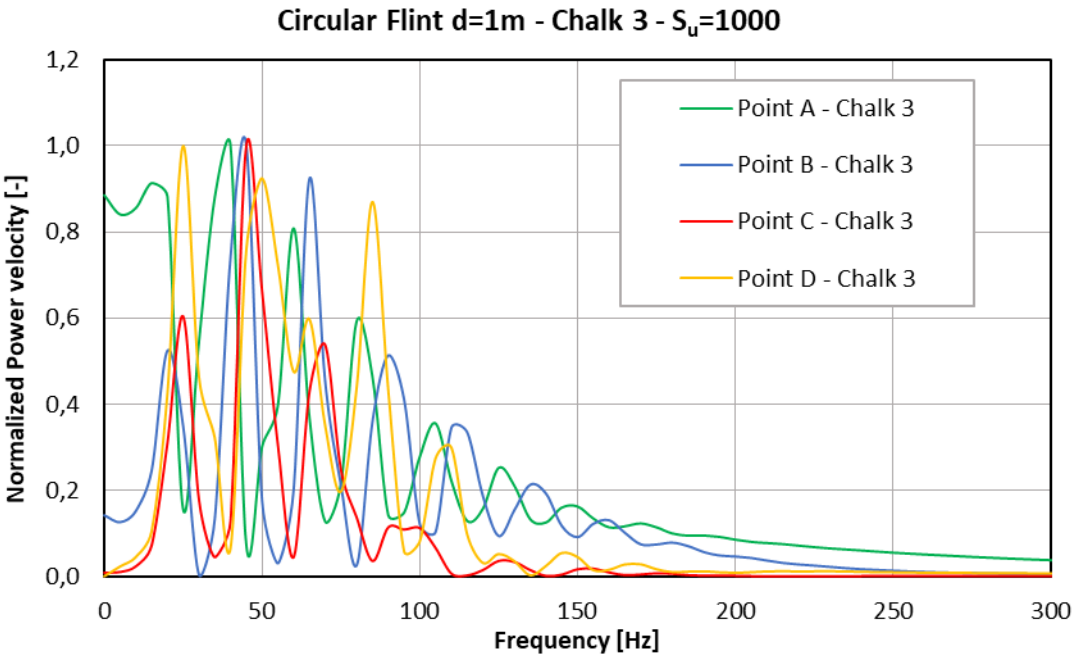

Figure 68 - Normalized Power Velocity - Circular Flint d=1m - Chalk 3

On the other hand, a comparison between Figure 69 and Figure 66, shows how a decrease of the dimension of the flint produces an increase of the frequencies characterized by a high energy content.

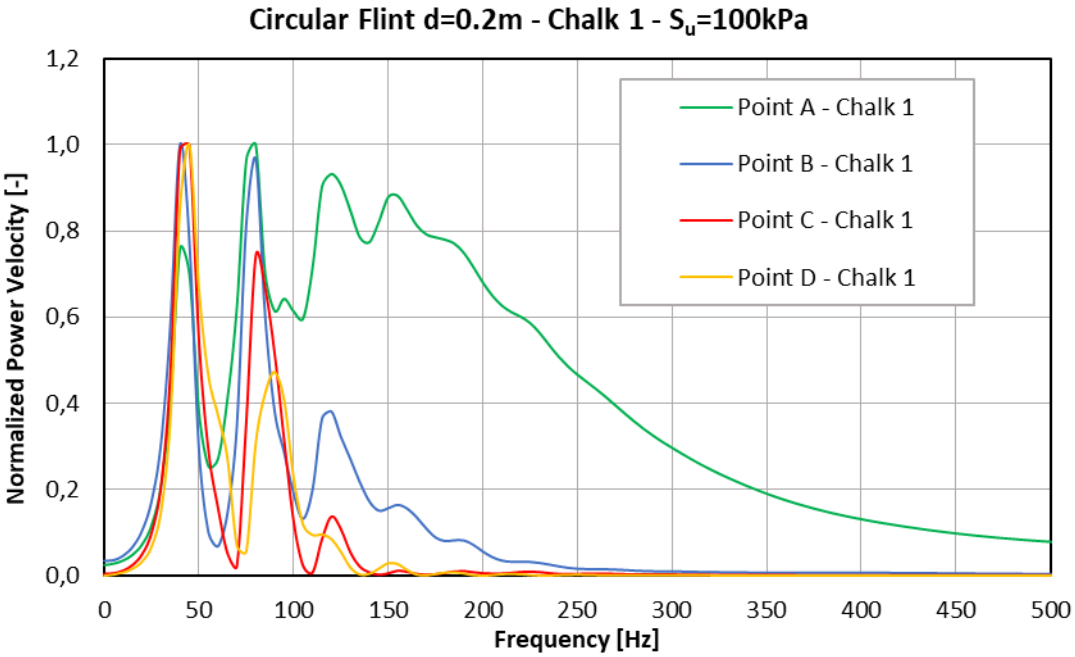

Figure 69 - Normalized Power Velocity - Circular Flint d=0.2m - Chalk 1

From the obtained results it is possible to understand that the vibrations induced on the surrounding soil are directly related to the size of the horizontal axis, which represents

the source of the ground motion. Indeed, being the flints subjected to a vertical impact load, the volume of the embedding soil displaced is a function of his size, in particular his horizontal dimensions. This concept is confirmed by a comparison between the power velocity spectrums obtained for the three different shapes analyzed.

The results obtained with the ellipsoidal flints (Figure 70 and Figure 71) show a comparable trend with the one obtained by considering a circular flint with the same horizontal axis.

These results confirm how the propagation of the wave is mainly governed by the size of the horizontal axis and the stiffness of the embedding soils.

Based on this finding, the Rayleigh coefficients have been evaluated for each type of investigated chalk and for the two different size of the horizontal axis explored.

The selection of the target frequencies has been done considering a band of 100Hz translated where the high energy content is observed.

The evaluation of the Rayleigh coefficients needs the assumption of a target damping, whose value is today object of debate. In this study a value of 5% has been imposed for both the target frequencies, as suggested by Amorosi et al. (Amorosi, et al., 2010).

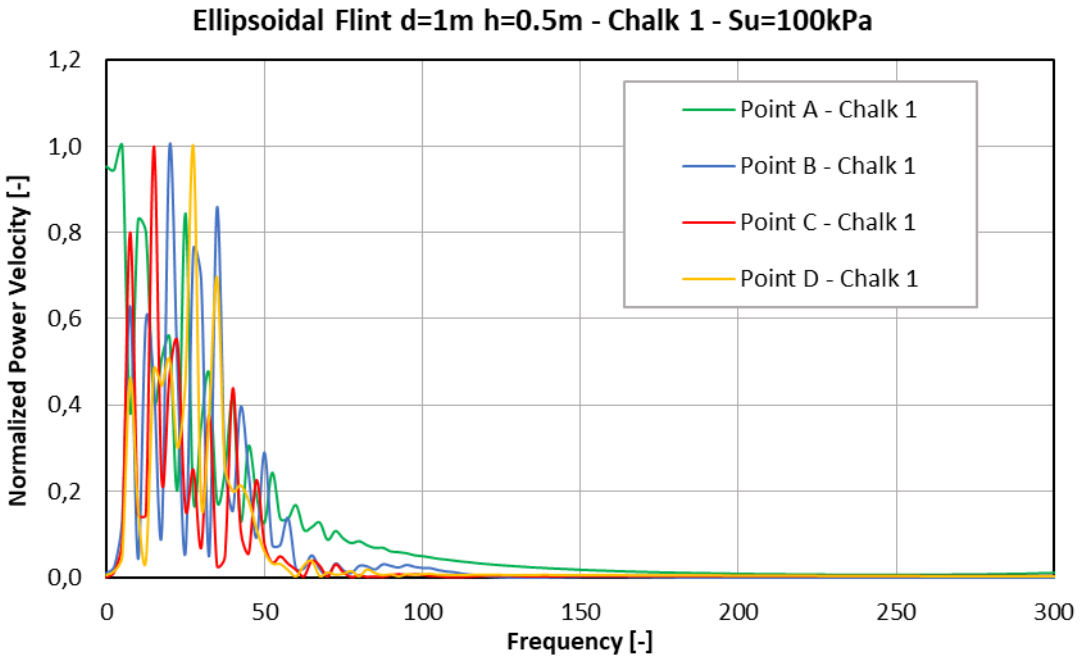

Figure 70 - Normalized Power Velocity - Ellipsoidal Flint d=1m h=0.5m - Chalk 1

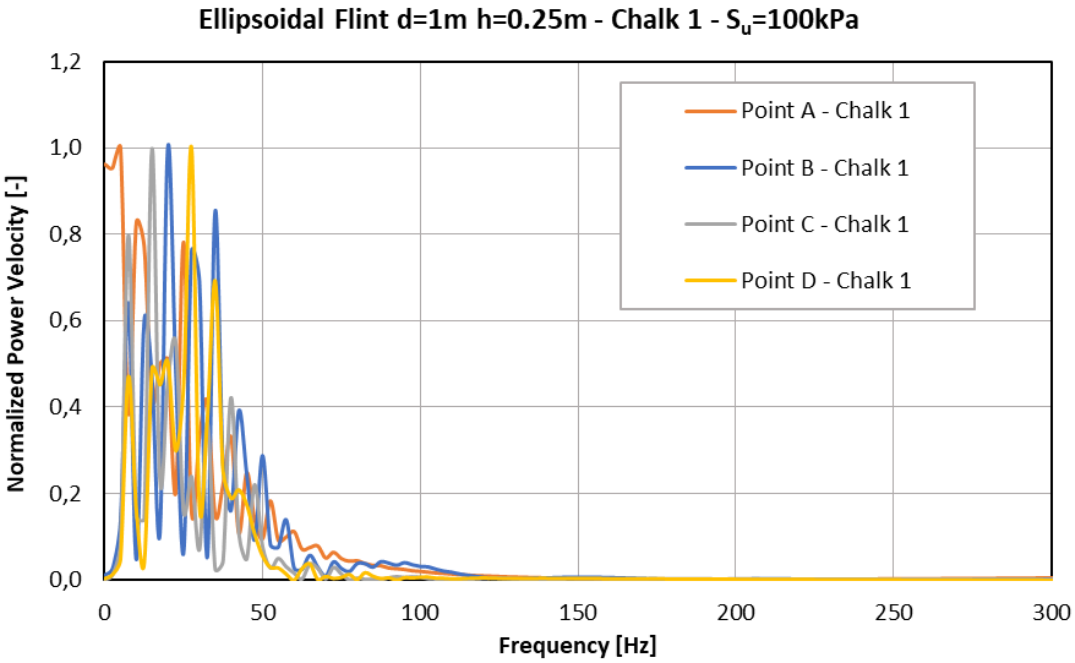

Figure 71 - Normalized Power Velocity - Ellipsoidal Flint d=1m h=0.25m - Chalk 1

The evaluation of the Rayleigh coefficients needs the assumption of a target damping, whose value is today object of debate. In this study a value of 5% has been imposed for both the target frequencies, as suggested by Amorosi et al. (Amorosi, et al., 2010).

Finally, by applying Equation 13and Equation 14, the Rayleigh damping parameters have been obtained for each explored dimensions and soil properties. A summary of the selected frequencies and the resulting Rayleigh coefficients is presented in Table 8.

Figure 72 shows the obtained damping curve for the Chalk 2, characterized by an undrained resistance equal to 500 kPa, and the two different size of the horizontal axis, respectively 1m and 0.2m.

Table 8 - Rayleigh coefficients

Horizontal axis size [m]	Soil type	f_n [Hz]	f_m [Hz]	D_R [%]	α_R [-]	β_R [-]
1	Chalk 1	5	105	5	3.0	1.45E-04
	Chalk 2	5	105	5	3.0	1.45E-04
	Chalk 3	30	130	5	15.3	9.95E-05
0.2	Chalk 1	40	140	5	19.5	8.85E-05
	Chalk 2	90	190	5	38.4	5.69E-05
	Chalk 3	140	240	5	55.4	4.19E-05

Figure 72 shows the obtained damping curve for the Chalk 2, characterized by an undrained resistance equal to 500 kPa, and the two different size of the horizontal axis, respectively 1m and 0.2m.

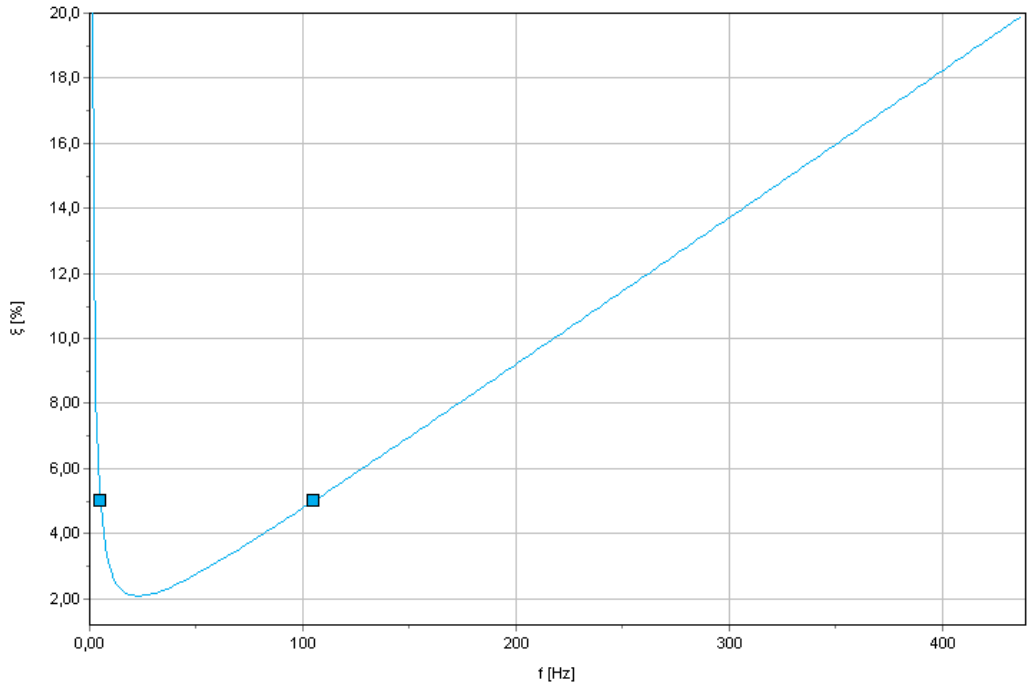

Figure 72 - Rayleigh damping curve - d=1m - Chalk 2

6.4. Dynamic analyses results

A parametric study has been carried out to evaluate the effects that shape and size of the flints have on its dynamical behaviour. The main features explored by the dynamical analyses can be summarized as follow:

- 3 different flint shape (1 circular and 2 ellipsoidal);
- 2 sizes for each selected flint geometry;
- 3 mechanical properties of the embedding soil;
- 5 peak forces;
- 2 application points (pile-flint contact point).

This led to a total of 180 dynamical analyses performed.

Three phases for each analysis were considered, one static and two dynamic. In the first, the initial stresses are initialized after the flint is created within the soil. In the second, the dynamic multiplier is activated in order to simulate the pile flint impact due to a single stroke (Δt=5 ms), while in the third no load are applied the free oscillations of the flint are analysed.

For each analysis, the final displacement of the flint and the module of the force that arise at the pile-flint contact point have been evaluated.

During the application of the dynamic force the flint is displaced into the soil. Once the load is removed, the flint starts to oscillate for about 0.1 seconds with a different frequency dependent on the flint size and on the stiffness of the embedding soil. A plastic displacement can be read at the end of the oscillation while part of the displacement is recovered.

Figure 73 shows an example of the time-displacement curves obtained.

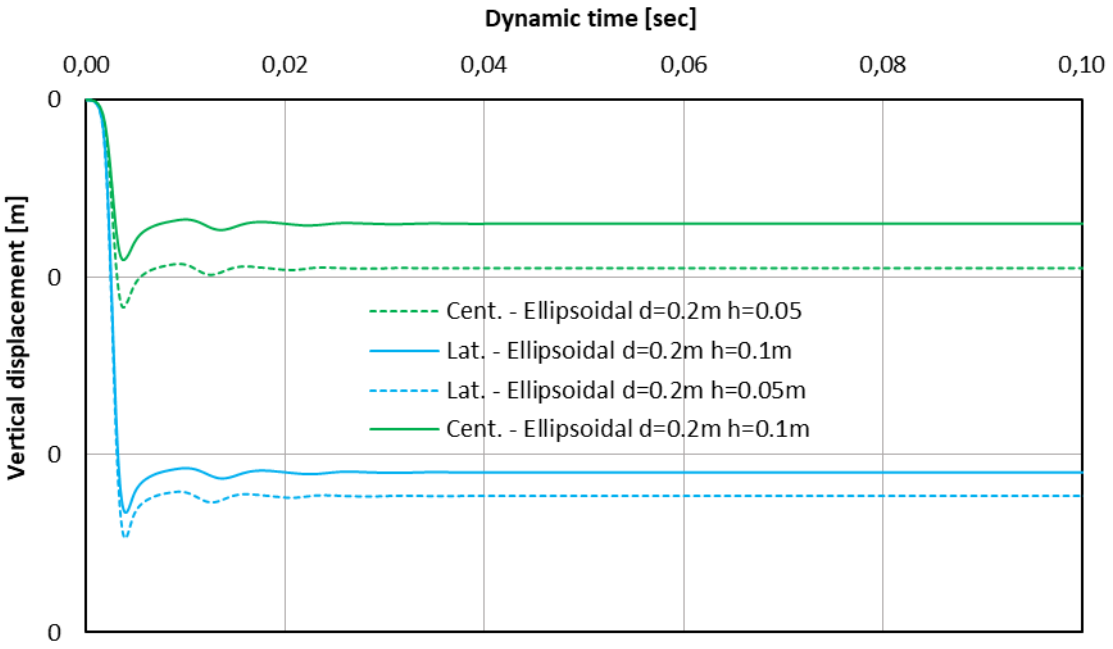

Figure 73 - Time-displacement curves

Regarding the force which arise at the pile tip, it has been evaluated as the module of the applied peak force and the resulting peak force acting on the horizontal spring.

In order to find a relationship between the force that arise at the pile-flint contact and the plastic displacement of the flint and allow a direct comparison between the obtained data, is important to find an equation able to take into account the main variables that influence the dynamical behavior of the flint.

The final displacement of the flint observed is mostly dependent by the following parameters:

- d [m], dimension of horizontal axis of the flint;
- L[m], length of the flint, equal to 1m due to plane strain condition;
- F [kN], module of the peak force acting on the pile tip;
- u_y [m], plastic displacement of the flint, measured at the pile-flint contact point;
- S_u,[kPa], undrained resistance of the embedding soil;
- E [kPa], undrained elastic modulus of the embedding soil.

The analysis of the involved parameters led to the following normalization of the module of the force acting on the contact point and of the final displacement of the flint:

$$f = \frac{F}{\sqrt{S_u E_u} dL}$$ Equation 26

$$x = \frac{u}{L}$$ Equation 27

This allow to consider obtain dimensionless quantity in which the main variables of the problem are directly considered.

6.4.1. Influence of the flint shape

A first consideration can be made about the influence of the flint shape. The obtained result shows a complex phenomenon.

In particular, for a chalk characterized by an undrained shear strength of 100kPa (Chalk1), ellipsoidal flints show systematically higher displacements (Figure 74).

Opposite behavior is shown in case of a chalk with an undrained shear strength of 1000kPa (Figure 75), where higher displacements are observed on the circular flints.

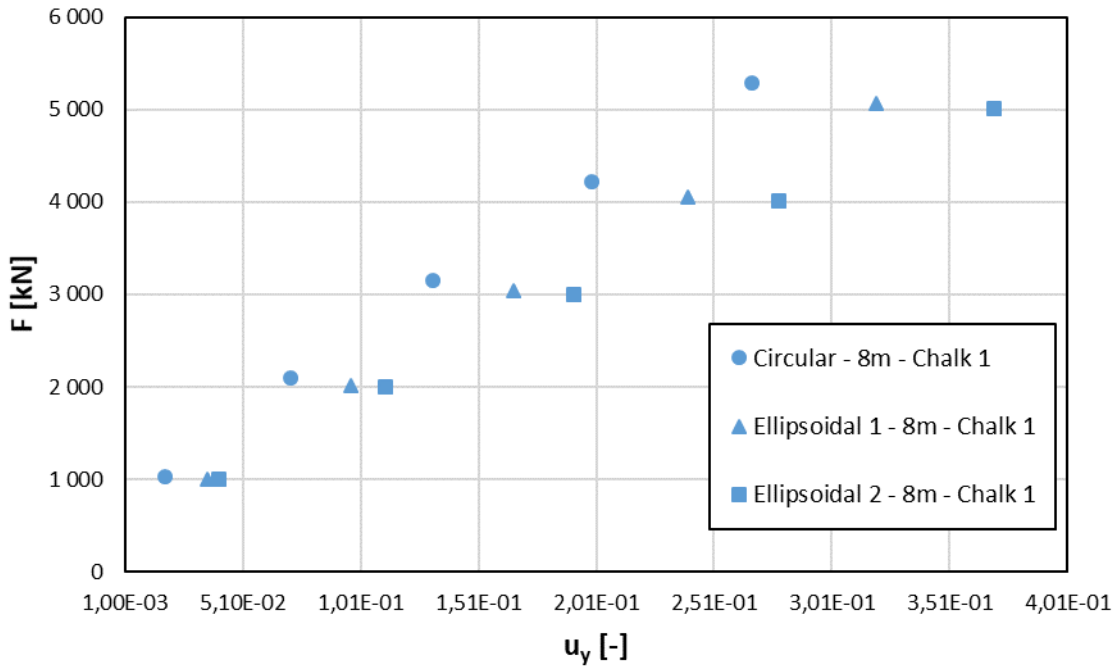

Figure 74 - Plot of the obtained results for a chalk with Su=100kPa.

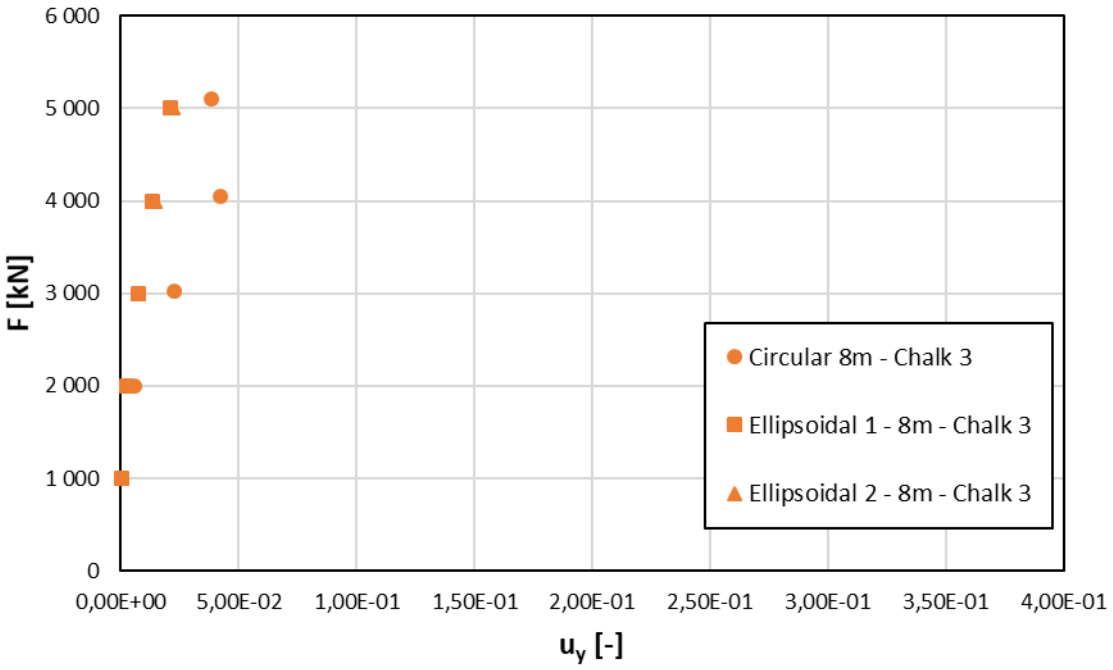

Figure 75 - Plot of the obtained results for chalk with Su=1000kPa

The obtained data could be explained by observing the flow mechanism of the circular flint.

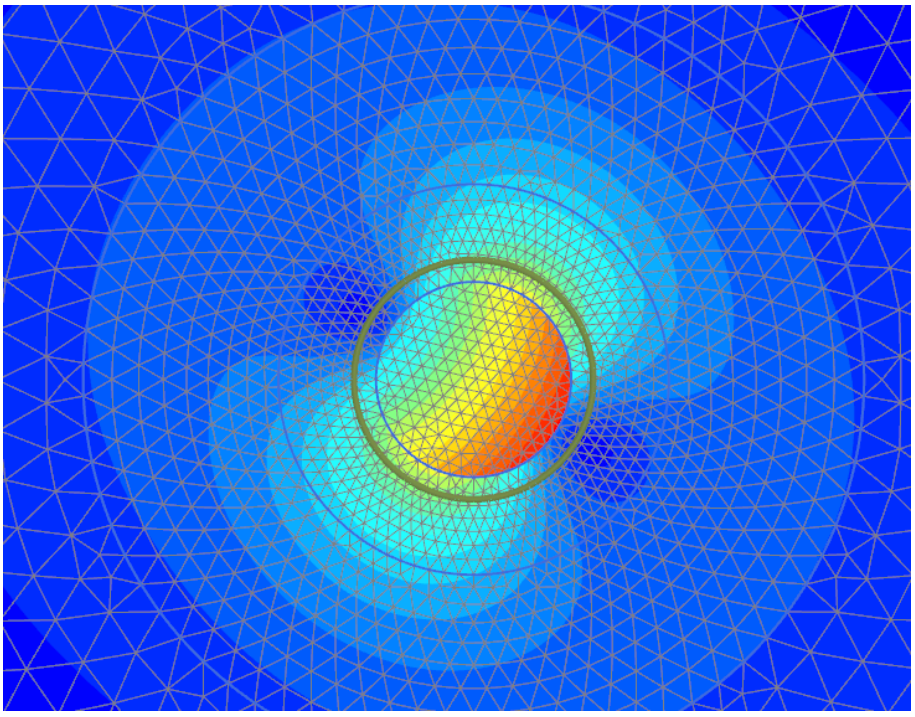

Figure 76 - Total displacements - Circular flint – Peak Force 5000 kN - Chalk 1

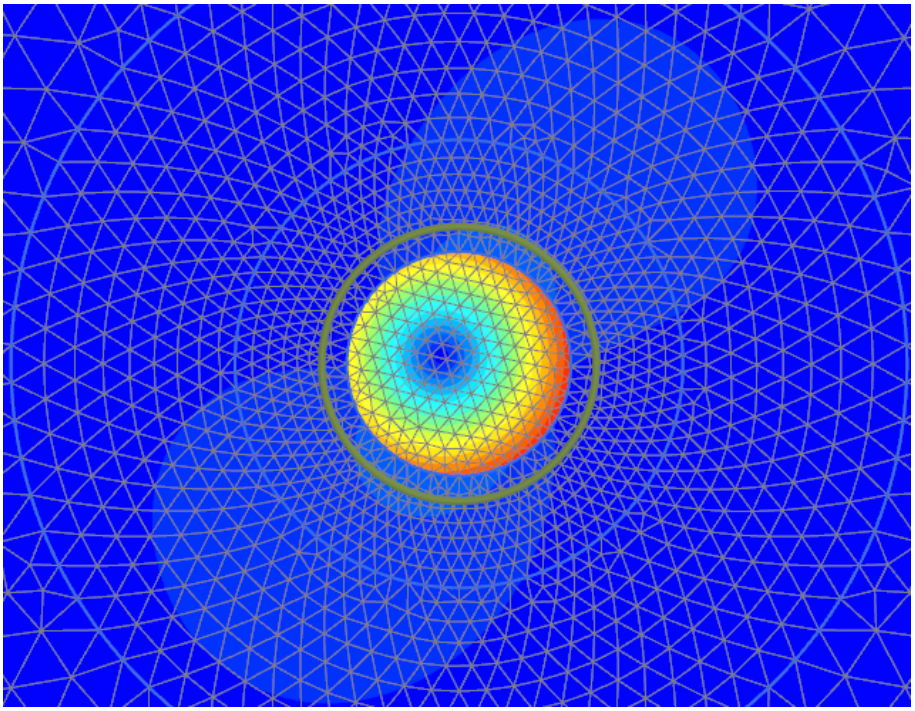

Figure 77 - Total displacements - Circular Flint - Peak Force 5000kN - Chalk 3

The results obtained for the more competent chalk, show that the applied force is not able to displace the flint within the soil, leading to a pure rotational failure mechanism.

In case of ellipsoidal flint, the same type of failure is avoided by the shape of the embedded obstruction, which, with the contribution of the high strength of the surrounding soil, limits the flint displacement. Comparing the resulting total displacements (Figure 78 and Figure 79), no valuable differences can be observed in this case.

The observed phenomena show the difficulty in the understanding of the mechanical behavior of potential obstructions encountered during pile driving. Several attempts to find a law able to reflects the different displacement obtained in function of the shapes of the flint and the strength of the embedding soil led to a higher dispersion of the data.

This finding and the enormous uncertainties represented by the shape e size of the flint and most importantly the non-predictable pile-flint contact point, are at base of the decision to process all the obtained data singularly, trying to find a law able to fit the data.

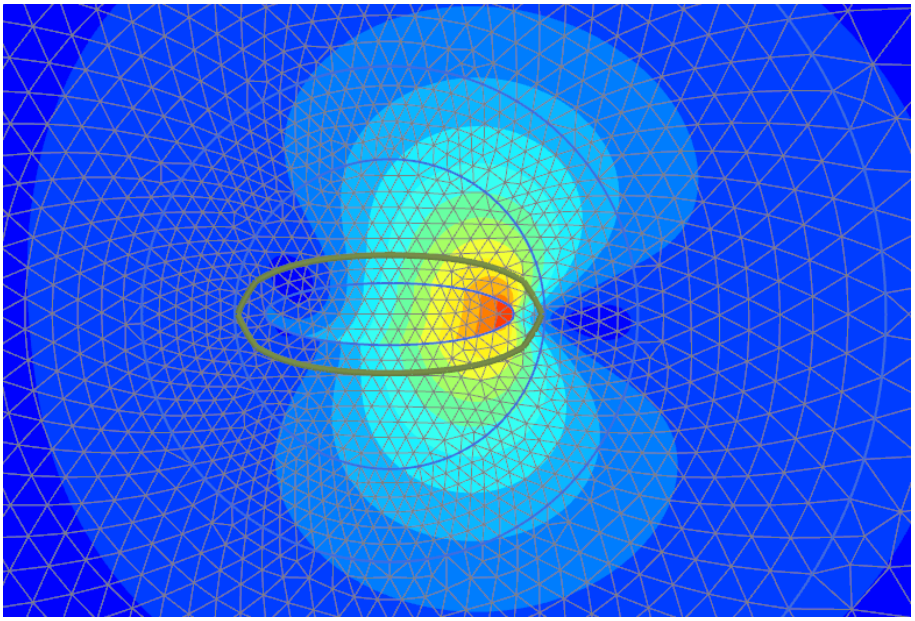

Figure 78 - Total displacements - Ellipsoidal flint h=d/4 - Peak Force 5000kN - Chalk 1

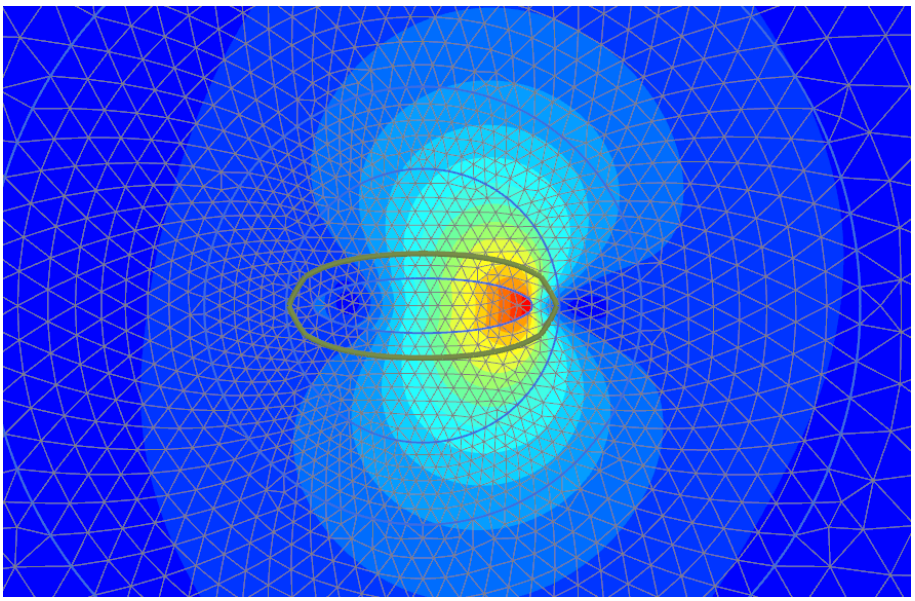

Figure 79 - Total displacements - Ellipsoidal flint h=d/4 - Peak force 5000kN - Chalk 3

6.4.2. FEA data processing

With the aim of finding a relationship between the pile advancement during pile driving and the force that arise at the pile tip due to a potential impact with a flint, the obtained dimensionless quantities have been reported on a semilogarithmic plot (Figure 80).

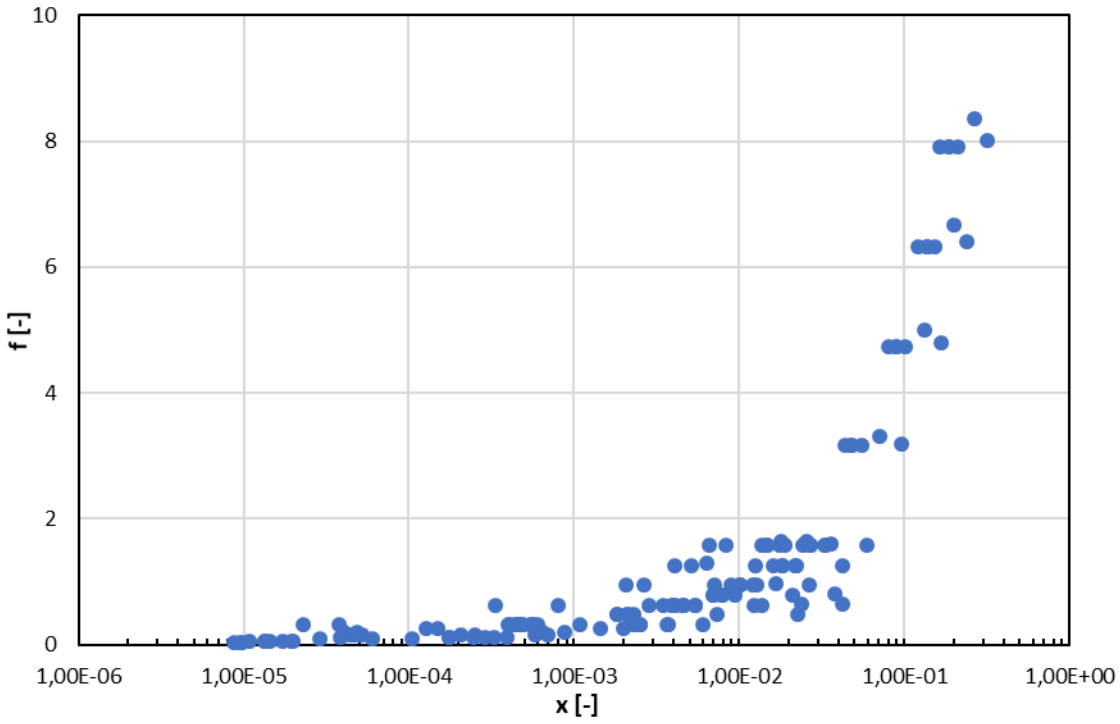

Figure 80 - Results of the dynamic finite element analyses

However, it is possible to notice that many results return displacements less than 1mm, representing an extremely slow advancement rate during pile driving. In fact, as previously described in Section 4.4.1, the API recommendations suggest as a refusal criterion a blow rate of 250 blows per 25cm, corresponding to 1mm per blow.

Thus, being the aim of the data processing of provide a driveability assessment, results characterized by displacements below 1mm have been not considered.

Figure 81 show the new distribution of the results of the dynamic analysis. By comparing the trend of the distribution of the points with the previous plot (Figure 80), a change in the response is now highlighted in correspondence of x=0.04 and f=1.2.

The relationship between the dimensionless quantities f and x can be reasonably represented by means of the following two parameters function on the semi-logarithmic plot:

$$f = k_1 log_{10} x + k_2 \qquad \text{Equation 28}$$

where the two parameter k_1 and k_2 assume different values depending on the value of the normalized displacement.

In particular:

- If x<0.04, the envelope is expressed by k_1 =0.56 and k_2 =2;
- If x>0.04, the force acting on the pile can be expressed through the parameters k_1 =8.6 and k_2 =13.2.

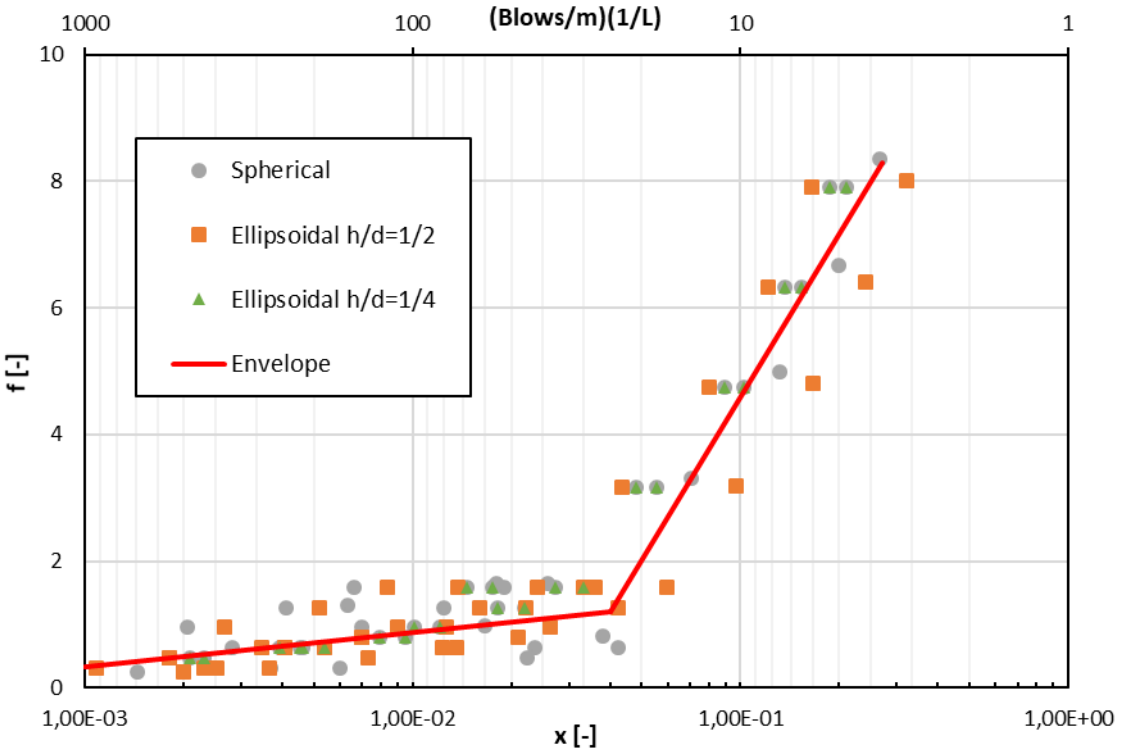

Figure 81 - FEA analyses results envelope

6.4.3. Safe drivability assessment

For large diameter piles (4m-8m), it can be assumed that the presence of the flint has no significant influence on the global resistance of the pile toe. Indeed, being the soil resistance to driving of large monopile mostly governed by the friction along the shaft, an increment of the pile toe resistance due to the presence of an obstruction is not perceptible during pile driving. However, when an obstruction is encountered, the punctual force which arise at the pile-boulder contact point can trigger a local distortion of the pile tip (§4.3). This initial damage subsequently propagates along the pile during the installation, leading to potential premature refusal or lower capacity of the foundation.

Being the driving not affected by the flint presence, the obtained equation (Equation 28) can be used to evaluate the admissible advancement rate which prevents accidental damage at the pile tip.

According to Aldridge et al. (Aldridge, et al., 2005), the force which produce the initiation of the damage of the pile tip can be evaluated as a function of the steel yield stress and the thickness of the pile (§4.4.2), through the following equations:

- $F_{lat} = 1.4\ \sigma_y t^2$, if applied horizontally;
- $F_{axial} = 2.8\ \sigma_y t^2$, for a near-axial force (1/4).

Being the impact point between the pile and the obstruction the main unknown of the whole problem, to provide a safe evaluation of the potential damage, in this study only the lower bound of the peak force has been adopted (i.e. horizontal force).

Thus, for a given pile it is possible to correlate the force that can trigger the local buckling at the pile tip and the maximum displacement per blow by means of the previously obtained relationship (). Finally, through a driveability analysis on GRLWEAP, it is possible to calibrate the hammer energy in order to maintain the evaluated blow/rate where layers of flints are expected.

The procedure for a safe driveability assessment can be summarized by the following steps:

I. for a given pile, known its yield stress σ_y and thickness t^2, it is possible to obtain the minimum force which prevent the local buckling of the pile tip by using the equation proposed by Aldridge et al.:

$$F_{lat} = 1.4\ \sigma_y t^2 \qquad \text{Equation 29}$$

II. given the chalk strength parameters (S_u,, E_u) and the presumable size of the potential encountered flint (d, L), the obtained force can be normalized as follow:

$$f = \frac{F}{\sqrt{S_u E_u} dL} \qquad \text{Equation 30}$$

III. with this force the value of the minimum displacement per blow that can damage the pile if a flint is encountered is obtained by using Equation 28:

$$f = k_1 log_{10} x + k_2$$

IV. once the maximum admissible displacement is known, the minimum blows rate to avoid damage of the pile is evaluated as:

$$blows\ rate\ \left(\frac{blows}{m}\right) < 1/u_y \qquad \text{Equation 31}$$

V. finally, through a driveability analysis, it is possible to evaluate the maximum hammer energy to prevent local buckling during the installation phase, by imposing a blow rate higher than previously obtained value.

7. Conclusions

7.1. Conclusions

In this study a detailed investigation of the pile-boulder interaction has been carried out, principally focused on the behaviour of an embedded flint, frequently encountered in white chalk during pile driving operations, and on the effect of its shape on its response to dynamical loads.

A literary review has been carried out with the purpose of investigating the mechanical behaviour of the materials involved in the research.

Subsequently, pile tip failure has been explored, in order to evaluate the mechanisms at the basis of this complex phenomenon, based on which the numerical models have been developed.

Numerical analyses have been carried out in two different directions.

A first series of static finite element analysis has been performed with the aim of examining the static failure mechanism developed in the soil due to the flint displacement. In this phase, three flint shapes and two different sizes have been analyzed. Since a pile is driven vertically in the soil, the horizontal and vertical forces able to produce a plastic vertical displacement of the obstruction have been evaluated. Being the potential impact point unpredictable, 10 different contact points have been explored. All the analyzed geometries have shown higher resistance for centrally displaced flint; however, the presence of horizontal forces double the risk for pile tip distortion. A comparison of the obtained horizontal forces led to the decision to perform the dynamic numerical analysis by applying the dynamic force to the flint in the center and at half his horizontal axis, representing the latter a good compromise between the maximum horizontal force obtained for each investigated geometry.

In a second phase, dynamical finite element analyses were run, including a parametric study which has been carried out with the aim of evaluating the influence of the factors involved in the phenomenon. Dynamical forces have been applied to each selected flint geometry and the final plastic displacement and the module of the force which arise at the impact point have been evaluated. By examining the obtained results, a relationship between the displacement and the force has been provided. Based on the latter, a safe

driveability assessment is suggested for large diameter pile, for which the encountered obstruction represents only a local problem which does not influence the driving.

Given the flint geometry, the strength and stiffness of the embedding chalk and the peak force that trigger the pile tip buckling, through the obtained equation the maximum blow rate which damage the pile is evaluated. In conclusion, by performing a driveability analysis it is possible (for large pile whose global driveability is not affected by the hit of the flint) to calibrate the hammer energy to be used when flint layers are expected, in order to limit the penetration rate and avoid potential damage of the pile tip.

7.2. Recommendations for further developments

The presented work represents a further development of a previous study conducted on the same subject (Gargarella, 2018), in which only a circular flint shape was considered. However, the obtained results suggest that further improvements should be made in order to create an even more robust model. Moreover, in order to provide results suitable for different hammer-pile-soil systems, the influence of several input parameters should be assessed.

More in details, the following studies are suggested:

- investigation of the influence that pile dimensions (i.e. pile stiffness) have in the phenomenon; different analyses obtained by considering different pile stiffness can lead to a new law suitable for different pile geometries;
- influence of the input load, like input duration or energy; these parameters can significantly modify the dynamical response of the obstruction and therefore its permanent displacement and the force which arise at the pile tip;
- use of a different material model in order to model the hysteretical damping and stiffness decay of the embedding chalk;
- benchmarking against known cases of pile damage induced by flint/boulders and/or against results of laboratory testing.

A deep investigation of the suggested studies could improve the knowledge of this complex phenomenon and a development of driveability analysis methods able to consider the potential presence of obstruction during pile driving operations.

8. References

4C Offshore, 2018. *Global market overview report,* Lowestoft UK: 4C Offshore.

Aldridge, T., Carrington, T. & Kee, N., 2005. *Propagation of pile tip damage during installation.* London, Taylor & Francis Group.

Amorosi, A., Boldini, D. & Elia, G., 2010. Parametric study on seismic ground response by finite element modelling. *Computers and Geotechnics,* 37(4), pp. 515-528.

Anusic, I., Eiksund, G. & Liingard, M., 2016. *Comparison of pile driveability methods based on a case study from an offshore wind farm in North Sea.* Reykjavik, ISSMGE.

API, 2011. *Geotechnical and foundation design consideration.* Washington: American Petroleum Institute.

Athanasopoulos, G. & Pelekis, P., 2000. Ground vibrations from sheetpile driving in urban environment: measurements, analysis and effects on buildings and occupants. *Soil Dynamics And Earthquake Engineering,* 19(5), pp. 371-387.

Bhattacharya, S. & Bolton, M., 2004. *Buckling of piles during earthquake liquefation.* Vancouver, Canadian Association for Earthquake Engineering.

Bhattacharya, S., Carrington, T. & Aldridge, T., 2005. *Buckling considerations in pile design.* London, Taylor & Francis Group.

BVG Associates, G., 2017. *Unleashing Europe's offshore wind potential,* Brussels: Wind Europe.

CFMS, 2018. *Recommandations pour la conception et le calcul des fondations d'éoliennes offshore.* Paris: Comité Francais de Mécanique des Sols et de Géotecnique.

Chatzigiannelis, I., 2009. *Foundation engineering of offshore "jacket" structures.* Orlando, American Society of Civil Engineers.

Cumming, F., 1999. *Machine tunneling in chalk with flint with particular reference to the mechanical properties of flint,* s.l.: Doctoral thesis: University of Brighton.

Erbrich, C., Barbosa-Cruz, E. & Barbour, R., 2010. *Soil-pile interaction during extrusion of an initially deformed pile.* London, Australia, Taylor & Francis.

Gargarella, P., 2018. *Numerical study of flint/boulder behaviour during pile driving.* s.l.:Master degree thesis: Politecnico di Torino.

Goble, G. & Rausche, F., 1999. *Wave Equation Manual.* Cleveland: s.n.

Holeyman, A., 2015. *Boulder-soil-pile dynamic interaction.* London, CRC Press.

Jardine, R. et al., 2018. *Behaviour of piles driven in chalk.* London, ICE Publishing.

Jiang, Z. et al., 2017. Structural reliability analysis of wind turbines: a reviw. *MDPI Energies,* Volume 10.

Kuhlemeyer, R. L. & Lysmer, J., 1973. Finite Element Method Accuracy for Wave Propagation Problems. *Journal of the Soil Mechanics and Foundations Division,* 99(5), pp. 421-424.

Lai, C., Foti, S. & Rota, M., 2013. *Input sismico e stabilità geotecnica dei siti di costruzione.* Pavia: Maggioli Editore.

Lake, L., 1975. *The engineering properties of Chalk with special reference to foundation design and performance.* London: s.n.

Lancellotta, R., 2012. *Geotecnica.* s.l.:Zanichelli.

Lanzo, G., Pagliaroli, A. & D'Elia, B., 2004. *Influenza della modellazione di Rayleigh dello smorzamento viscoso nelle analisi di risposta sismica locale.* Genova, s.n.

Lautridou, J. P., 1986. Porosity and frost susceptibility of flints and chalk: laboratory experiments, comparison of glacial and periglacial surface textureof flint materials and field investigations. In: C. U. Press, a cura di *The scientific study of flint.* Cambridge: s.n., pp. 269-282.

Lawrence, J. & Collier, R., 2017. Engineering geological characterization of flints. *Quaterly Journal of Engineering Geology and Hydrogeology.*

Lawrence, J. & Collins, R., 2017. Engineering characterization of flints. *Quaterly Journal of Engineering Geology and Hydrogeology,* Volume 50, pp. 133-147.

LEANWIND, 2017. *Driving cost reductions in offshore wind,* Cork: LEANWIND.

Lord, J., Clayton, C. & Mortimore, R., 2002. *Engineering in chalk.* London: CIRIA.

Lysmer, J. & Kuhlemeyer, R. L., 1969. Finite Dynamic Model for Infinite Media. *Journal of Engineering Mechanics Division,* Volume 95, pp. 859-878.

Martin, C. & Randolph, M., 2006. Upper-bound analysis of lateral pile capacity in cohesive soil. *Geotechnique,* 56(2), pp. 141-145.

Massarch, K. & Fellenius, B., 2008. *Ground vibrations induced by impact driving.* Arlington, s.n.

Massarsch, K., 1993. Static and dynamic soil displacement caused by pile driving. *Australian Geomechanics Journal*, August, pp. 84-92.

Matthews, M. & Clayton, C., 1993. Influence of intact porosity on the engineering properties of a weak rock. *Geotechnical Engineering of Hard Soils-Soft Rocks,* pp. 693-702.

Mortimore, J., 2011. A chalk revolution: what have we done to the Chalk of England?. *Proceedings of the Geologists' Association,* pp. 232-297.

Mortimore, J. & Wood, C., 1983. *The distribution of the flint in the English Chalk, with particular reference to the "Brandon Flint Series" and the high Turonian flin maximum.* New York, Cambridge University Press, pp. 7-20.

Mortimore, R., 2010. A chalk revolution: what have we done to the Chalk of England?. *Proceedings of the Geologists' Association,* p. 233.

Mortimore, R. & Duperret, A., 2004. Chalk physical properties and cliff instability. *Engineering geology special publications,* Volume 20, pp. 75-88.

Mortimore, R. & Wood, C., 1986. *The distribution of Flint in the English Chalk.* s.l., Conference Paper.

Mortimore, R., Wood, C. & Gallois, R., 2001. British Upper Cretaceous Stratigraphy. *Geological Conservation Review Series,* Volume 23, p. 558.

Musial, W., Butterfield, S. & Boone, A., 2004. *Feasibility of floating platform systems for wind turbines.* United States, National Renewable Energy Lab..

Nichols, G., 2009. *Sedimentology and Stratigraphy.* 2nd ed. Chichester: Wiley-Blackwell.

PLAXIS, 2018. *Plaxis 2D Reference Manual.* s.l.:s.n.

Puig, J., 1973. Problèmes de terrassement dans la craie. *La Craie,* pp. 81-98.

Randolph, M., 2018. Potential damage to steel pipe piles during installation. *IPA News Letter,* March, 3(1), pp. 3-10.

Randolph, M. & Houlsby, G., 1984. The limitating pressure on a circular pile loaded laterally in cohesive soil. *Géotecnique,* 34(613-623), pp. 613-623.

Rausche, F., 2000. *Pile driving equipment: capabilities and properties.* Sao Paulo, s.n.

Roark, R. & Young, W., 1975. *Formulas for stress and strain.* London: McGraw-Hill Book Company.

Smith, E., 1960. Pile-Driving Analysis by the Wave Equation. *Journal of the Engineering Mechanics Division,* Volume 4, p. 86.

Snyder, B. & Kaiser, M., 2008. Ecological and economic cost-benefit analysis of offshore wind energy. *Renewable Energy,* 34(6), pp. 1567-1578.

Structures, F. E. o. O. "., 2009. *Chatzigiannelis, I.*. Orlando, American Society of Civil Engineers.

Stuyts, B. et al., 2017. *A methodology for the probabilistic assessment of pile refusal due to boulder encounter.* London, Society of Underwater Technology.

Wind Europe, 2019. *Offshore wind in Europe - Key trends and statistics 2018,* Brussels: Wind Europe.

Zhang, J. et al., 2010. *Static and dynamic analysis of monopile foundation for offshore wind farm.* Beijing, ISOPE.

Zhou, H., Randolph, F., 2011. Effect of shaft on resistance of a ball penetrometer. *Geotecnique,* pp. 973-981.

9. Appendices

9.1. Appendix A

9.1.1. Static finite element analyses results – Circular Flint

	R_{inter}=1		R_{inter}=0,5		R_{inter}=0,1	
δ/R [-]	F_y [kN/m]	F_x [kN/m]	F_y [kN/m]	F_x [kN/m]	F_y [kN/m]	F_x [kN/m]
0,00	240,0	0,0	217,3	0,0	192,3	0,0
0,17	236,4	41,8	214,0	37,6	189,3	33,3
0,34	225,6	81,9	204,2	74,2	180,7	65,6
0,50	207,9	119,5	188,2	108,3	166,5	95,7
0,64	184,1	151,7	166,7	138,7	147,4	123,0
0,77	156,3	159,8	140,5	153,4	127,7	144,0
0,87	129,5	146,8	114,5	143,2	97,7	156,7
0,94	104,9	134,0	89,1	153,0	69,0	171,1
0,98	82,8	120,1	61,2	166,0	38,0	179,7
1,00	62,8	0,0	31,4	0,0	6,3	0,0

9.1.2. Static finite element analyses results – Ellipsoidal h=d/2

	R_{inter}=1		R_{inter}=0,5		R_{inter}=0,1	
δ/R [-]	F_y [kN/m]	F_x [kN/m]	F_y [kN/m]	F_x [kN/m]	F_y [kN/m]	F_x [kN/m]
0,0	231,9	0,0	221,5	0,0	205,6	0,0
0,1	222,1	38,8	210,9	33,3	194,3	26,9
0,2	203,6	54,4	192,1	45,9	174,6	40,1
0,3	183,2	62,9	171,1	53,4	148,6	51,8
0,4	162,1	67,1	146,1	56,8	124,8	42,0
0,5	140,9	66,7	124,4	50,7	106,3	36,1
0,6	120,2	63,5	106,4	47,5	91,3	33,4
0,7	102,2	57,2	91,5	41,9	79,0	29,9
0,8	87,1	49,1	78,9	33,6	68,7	25,2
0,9	74,3	35,1	68,5	24,1	60,2	15,7
1,0	63,5	0,0	59,9	0,0	53,2	0,0

9.1.3. Static finite element analyses results – Ellipsoidal h=d/4

	R_{inter}=1		R_{inter}=0,5		R_{inter}=0,1	
δ/R [-]	F_y [kN/m]	F_x [kN/m]	F_y [kN/m]	F_x [kN/m]	F_y [kN/m]	F_x [kN/m]
0,0	230,0	0,0	226,2	0,0	216,7	0,0
0,1	210,9	24,1	206,6	19,6	196,5	11,1
0,2	188,7	28,5	184,3	22,1	173,0	8,2
0,3	166,2	28,9	161,8	22,1	150,1	7,7
0,4	143,8	28,0	139,3	21,8	129,5	7,4
0,5	122,6	27,5	119,2	23,0	111,9	7,5
0,6	105,2	26,1	102,7	22,2	97,2	7,5
0,7	91,3	23,2	89,3	20,8	85,3	7,2
0,8	80,0	19,4	78,5	18,3	75,6	6,7
0,9	70,9	14,1	69,6	14,3	67,6	6,0
1,0	63,4	0,0	62,2	0,0	60,8	0,0

9.1.4. Static finite element analyses results with pile

	Circular			Ellipsoidal h=d/2		Ellipsoidal h=d/4	
δ/R [-]	F_y [kN/m]	F_x [kN/m]	δ/R [-]	F_y [kN/m]	F_x [kN/m]	F_y [kN/m]	F_x [kN/m]
0,00	1166,9	0,0	0,0	1153,0	0,0	1100,0	0,0
0,17	1153,6	197,5	0,1	1109,0	163,9	1015,0	20,1
0,34	1110,9	403,9	0,2	1024,7	234,5	901,0	19,5
0,50	1019,9	579,8	0,3	922,3	273,0	784,7	20,6
0,64	900,6	718,7	0,4	816,4	290,4	677,1	30,1
0,77	764,4	760,1	0,5	710,1	286,3	582,6	35,6
0,87	631,8	704,8	0,6	606,0	272,2	504,0	37,6
0,94	509,3	634,0	0,7	514,0	235,5	439,5	36,5
0,98	399,2	446,2	0,8	436,3	188,6	386,2	29,0
1,00	358,8	0,0	0,9	372,5	100,0	344,5	12,8
			1,0	356,8	0,0	317,7	0,0

9.2. Appendix B

9.2.1. Input load - Normalized bottom force

Time [ms]	Bottom Force [kN]	Norm. Load [-]
0,00	0	0,0000
0,06	90	0,0021
0,12	180	0,0041
0,18	288	0,0066
0,24	395	0,0090
0,30	465	0,0106
0,36	536	0,0123
0,42	655	0,0150
0,48	773	0,0177
0,54	963	0,0220
0,61	1153	0,0264
0,67	1444	0,0330
0,73	1734	0,0397
0,79	2160	0,0494
0,85	2585	0,0591
0,91	3187	0,0729
0,97	3788	0,0866
1,03	4607	0,1054
1,09	5426	0,1241
1,15	6501	0,1487
1,21	7577	0,1733
1,27	8940	0,2045
1,33	10303	0,2357
1,39	11966	0,2737
1,45	13630	0,3118
1,51	15580	0,3564
1,57	17531	0,4010
1,63	19723	0,4511
1,69	21914	0,5013
1,75	24259	0,5549
1,82	26604	0,6085
1,88	28973	0,6627
1,94	31343	0,7169
2,00	33571	0,7679
2,06	35800	0,8189
2,12	37698	0,8623
2,18	39596	0,9057
2,24	40972	0,9372
2,30	42348	0,9686
2,36	43033	0,9843

2,42	43718	1,0000
2,48	43602	0,9973
2,54	43485	0,9947
2,60	42538	0,9730
2,66	41592	0,9514
2,72	39893	0,9125
2,78	38195	0,8737
2,84	35957	0,8225
2,90	33719	0,7713
2,96	31193	0,7135
3,03	28666	0,6557
3,09	26082	0,5966
3,15	23497	0,5375
3,21	21171	0,4843
3,27	18845	0,4310
3,33	17012	0,3891
3,39	15179	0,3472
3,45	13929	0,3186
3,51	12679	0,2900
3,57	11935	0,2730
3,63	11191	0,2560
3,69	10762	0,2462
3,75	10334	0,2364
3,81	10008	0,2289
3,87	9683	0,2215
3,93	9300	0,2127
3,99	8918	0,2040
4,05	8392	0,1920
4,11	7866	0,1799
4,17	7167	0,1639
4,24	6467	0,1479
4,30	5585	0,1278
4,36	4703	0,1076
4,42	3631	0,0831
4,48	2559	0,0585
4,54	1905	0,0436
4,60	1250	0,0286
4,66	925	0,0212
4,72	600	0,0137
4,78	450	0,0103
4,84	300	0,0069
4,90	225	0,0051
4,96	150	0,0034
5,02	75	0,0017
5,08	0	0,0000

9.3. Appendix C

9.3.1. Dynamical finite element result – Central impact point

Shape	d [m]	h [m]	E_u [kPa]	S_u [kPa]	F_y [kN]	F_x [kN]	$u_{y,perm}$ [m]	F_R [kN]	$F_{R,norm}$ [-]
Circular	0,2	0,20	1,00E+05	100	1000	0,0	1,47E-02	1000,0	1,58
Circular	0,2	0,20	1,00E+05	100	2000	0,0	4,80E-02	2000,0	3,16
Circular	0,2	0,20	1,00E+05	100	3000	0,0	8,96E-02	3000,0	4,74
Circular	0,2	0,20	1,00E+05	100	4000	0,0	1,37E-01	4000,0	6,32
Circular	0,2	0,20	1,00E+05	100	5000	0,0	1,87E-01	5000,0	7,91
Circular	0,2	0,20	5,00E+05	500	1000	0,0	4,84E-04	1000,0	0,32
Circular	0,2	0,20	5,00E+05	500	2000	0,0	3,92E-03	2000,0	0,63
Circular	0,2	0,20	5,00E+05	500	3000	0,0	1,01E-02	3000,0	0,95
Circular	0,2	0,20	5,00E+05	500	4000	0,0	1,81E-02	4000,0	1,26
Circular	0,2	0,20	5,00E+05	500	5000	0,0	2,72E-02	5000,0	1,58
Circular	0,2	0,20	1,00E+06	1000	1000	0,0	4,97E-05	1000,0	0,16
Circular	0,2	0,20	1,00E+06	1000	2000	0,0	5,60E-04	2000,0	0,32
Circular	0,2	0,20	1,00E+06	1000	3000	0,0	2,10E-03	3000,0	0,47
Circular	0,2	0,20	1,00E+06	1000	4000	0,0	4,63E-03	4000,0	0,63
Circular	0,2	0,20	1,00E+06	1000	5000	0,0	7,94E-03	5000,0	0,79
Ellipsoidal	0,20	0,10	1,00E+05	100	1000	0,0	1,37E-02	1000,0	1,58
Ellipsoidal	0,20	0,10	1,00E+05	100	2000	0,0	4,34E-02	2000,0	3,16
Ellipsoidal	0,20	0,10	1,00E+05	100	3000	0,0	8,00E-02	3000,0	4,74
Ellipsoidal	0,20	0,10	1,00E+05	100	4000	0,0	1,21E-01	4000,0	6,32
Ellipsoidal	0,20	0,10	1,00E+05	100	5000	0,0	1,66E-01	5000,0	7,91
Ellipsoidal	0,20	0,10	5,00E+05	500	1000	0,0	4,05E-04	1000,0	0,32
Ellipsoidal	0,20	0,10	5,00E+05	500	2000	0,0	3,48E-03	2000,0	0,63
Ellipsoidal	0,20	0,10	5,00E+05	500	3000	0,0	8,99E-03	3000,0	0,95
Ellipsoidal	0,20	0,10	5,00E+05	500	4000	0,0	1,61E-02	4000,0	1,26
Ellipsoidal	0,20	0,10	5,00E+05	500	5000	0,0	2,41E-02	5000,0	1,58
Ellipsoidal	0,20	0,10	1,00E+06	1000	1000	0,0	4,47E-05	1000,0	0,16
Ellipsoidal	0,20	0,10	1,00E+06	1000	2000	0,0	4,56E-04	2000,0	0,32
Ellipsoidal	0,20	0,10	1,00E+06	1000	3000	0,0	1,82E-03	3000,0	0,47
Ellipsoidal	0,20	0,10	1,00E+06	1000	4000	0,0	4,07E-03	4000,0	0,63
Ellipsoidal	0,20	0,10	1,00E+06	1000	5000	0,0	7,00E-03	5000,0	0,79
Ellipsoidal	0,20	0,05	1,00E+05	100	1000	0,0	1,75E-02	1000,0	1,58
Ellipsoidal	0,20	0,05	1,00E+05	100	2000	0,0	5,55E-02	2000,0	3,16
Ellipsoidal	0,20	0,05	1,00E+05	100	3000	0,0	1,02E-01	3000,0	4,74
Ellipsoidal	0,20	0,05	1,00E+05	100	4000	0,0	1,54E-01	4000,0	6,32
Ellipsoidal	0,20	0,05	1,00E+05	100	5000	0,0	2,10E-01	5000,0	7,91
Ellipsoidal	0,20	0,05	5,00E+05	500	1000	0,0	4,67E-04	1000,0	0,32
Ellipsoidal	0,20	0,05	5,00E+05	500	2000	0,0	4,54E-03	2000,0	0,63

Ellipsoidal	0,20	0,05	5,00E+05	500	3000	0,0	1,21E-02	3000,0	0,95
Ellipsoidal	0,20	0,05	5,00E+05	500	4000	0,0	2,19E-02	4000,0	1,26
Ellipsoidal	0,20	0,05	5,00E+05	500	5000	0,0	3,31E-02	5000,0	1,58
Ellipsoidal	0,20	0,05	1,00E+06	1000	1000	0,0	4,82E-05	1000,0	0,16
Ellipsoidal	0,20	0,05	1,00E+06	1000	2000	0,0	5,43E-04	2000,0	0,32
Ellipsoidal	0,20	0,05	1,00E+06	1000	3000	0,0	2,31E-03	3000,0	0,47
Ellipsoidal	0,20	0,05	1,00E+06	1000	4000	0,0	5,38E-03	4000,0	0,63
Ellipsoidal	0,20	0,05	1,00E+06	1000	5000	0,0	9,46E-03	5000,0	0,79
Circular	1,00	1,00	1,00E+05	100	1000	0,0	2,29E-05	1000,0	0,32
Circular	1,00	1,00	1,00E+05	100	2000	0,0	3,34E-04	2000,0	0,63
Circular	1,00	1,00	1,00E+05	100	3000	0,0	2,05E-03	3000,0	0,95
Circular	1,00	1,00	1,00E+05	100	4000	0,0	4,10E-03	4000,0	1,26
Circular	1,00	1,00	1,00E+05	100	5000	0,0	6,65E-03	5000,0	1,58
Circular	1,00	1,00	5,00E+05	500	1000	0,0	1,43E-05	1000,0	0,06
Circular	1,00	1,00	5,00E+05	500	3000	0,0	4,07E-05	3000,0	0,19
Circular	1,00	1,00	5,00E+05	500	4000	0,0	1,28E-04	4000,0	0,25
Circular	1,00	1,00	5,00E+05	500	2000	0,0	1,76E-04	2000,0	0,13
Circular	1,00	1,00	5,00E+05	500	5000	0,0	4,03E-04	5000,0	0,32
Circular	1,00	1,00	1,00E+06	1000	1000	0,0	8,43E-06	1000,0	0,03
Circular	1,00	1,00	1,00E+06	1000	2000	0,0	8,43E-06	2000,0	0,06
Circular	1,00	1,00	1,00E+06	1000	3000	0,0	2,55E-05	3000,0	0,09
Circular	1,00	1,00	1,00E+06	1000	4000	0,0	3,43E-05	4000,0	0,13
Circular	1,00	1,00	1,00E+06	1000	5000	0,0	4,22E-05	5000,0	0,16
Ellipsoidal	1,00	0,50	1,00E+05	100	1000	0,0	3,75E-05	1000,0	0,32
Ellipsoidal	1,00	0,50	1,00E+05	100	2000	0,0	8,00E-04	2000,0	0,63
Ellipsoidal	1,00	0,50	1,00E+05	100	3000	0,0	2,66E-03	3000,0	0,95
Ellipsoidal	1,00	0,50	1,00E+05	100	4000	0,0	5,18E-03	4000,0	1,26
Ellipsoidal	1,00	0,50	1,00E+05	100	5000	0,0	8,34E-03	5000,0	1,58
Ellipsoidal	1,00	0,50	5,00E+05	500	1000	0,0	1,34E-05	1000,0	0,06
Ellipsoidal	1,00	0,50	5,00E+05	500	2000	0,0	1,75E-04	2000,0	0,13
Ellipsoidal	1,00	0,50	5,00E+05	500	3000	0,0	4,83E-05	3000,0	0,19
Ellipsoidal	1,00	0,50	5,00E+05	500	4000	0,0	1,50E-04	4000,0	0,25
Ellipsoidal	1,00	0,50	5,00E+05	500	5000	0,0	4,36E-04	5000,0	0,32
Ellipsoidal	1,00	0,50	1,00E+06	1000	1000	0,0	9,54E-06	1000,0	0,03
Ellipsoidal	1,00	0,50	1,00E+06	1000	2000	0,0	1,71E-05	2000,0	0,06
Ellipsoidal	1,00	0,50	1,00E+06	1000	3000	0,0	2,91E-05	3000,0	0,09
Ellipsoidal	1,00	0,50	1,00E+06	1000	4000	0,0	3,82E-05	4000,0	0,13
Ellipsoidal	1,00	0,50	1,00E+06	1000	5000	0,0	5,22E-05	5000,0	0,16

9.3.2. Dynamical finite element analyses results – Lateral impact point

d [m]	h [m]	Shape	E_u [kPa]	S_u [kPa]	F_y [kN]	F_x [kN]	$u_{y,perm}$ [m]	F_R [kN]	$F_{R,norm}$ [-]
0,2	0,20	Circular	1,00E+05	100	1000	271,8	1,81E-02	1036,3	1,64
0,2	0,20	Circular	1,00E+05	100	2000	625,4	7,11E-02	2095,5	3,31
0,2	0,20	Circular	1,00E+05	100	3000	982,2	1,31E-01	3156,7	4,99
0,2	0,20	Circular	1,00E+05	100	4000	1339,7	1,99E-01	4218,4	6,67
0,2	0,20	Circular	1,00E+05	100	5000	1697,5	2,67E-01	5280,3	8,35
0,2	0,20	Circular	5,00E+05	500	1000	47,6	3,70E-03	1001,1	0,32
0,2	0,20	Circular	5,00E+05	500	2000	324,2	2,37E-02	2026,1	0,64
0,2	0,20	Circular	5,00E+05	500	3000	674,8	1,66E-02	3074,9	0,97
0,2	0,20	Circular	5,00E+05	500	4000	1040,3	6,33E-03	4133,1	1,31
0,2	0,20	Circular	5,00E+05	500	5000	1410,7	2,57E-02	5195,2	1,64
0,2	0,20	Circular	1,00E+06	1000	1000	3,4	2,52E-04	1000,0	0,16
0,2	0,20	Circular	1,00E+06	1000	2000	77,8	5,99E-03	2001,5	0,32
0,2	0,20	Circular	1,00E+06	1000	3000	325,2	2,24E-02	3017,6	0,48
0,2	0,20	Circular	1,00E+06	1000	4000	640,1	4,24E-02	4050,9	0,64
0,2	0,20	Circular	1,00E+06	1000	5000	991,1	3,82E-02	5097,3	0,81
0,20	0,10	Ellipsoidal	1,00E+05	100	1000	124,5	3,61E-02	1007,7	1,59
0,20	0,10	Ellipsoidal	1,00E+05	100	2000	288,8	9,67E-02	2020,7	3,20
0,20	0,10	Ellipsoidal	1,00E+05	100	3000	455,2	1,66E-01	3034,3	4,80
0,20	0,10	Ellipsoidal	1,00E+05	100	4000	622,1	2,40E-01	4048,1	6,40
0,20	0,10	Ellipsoidal	1,00E+05	100	5000	789,5	3,20E-01	5061,9	8,00
0,20	0,10	Ellipsoidal	5,00E+05	500	1000	11,5	2,30E-03	1000,1	0,32
0,20	0,10	Ellipsoidal	5,00E+05	500	2000	52,7	1,23E-02	2000,7	0,63
0,20	0,10	Ellipsoidal	5,00E+05	500	3000	107,0	2,63E-02	3001,9	0,95
0,20	0,10	Ellipsoidal	5,00E+05	500	4000	166,5	4,23E-02	4003,5	1,27
0,20	0,10	Ellipsoidal	5,00E+05	500	5000	228,1	5,94E-02	5005,2	1,58
0,20	0,10	Ellipsoidal	1,00E+06	1000	1000	1,9	2,07E-04	1000,0	0,16
0,20	0,10	Ellipsoidal	1,00E+06	1000	2000	12,3	2,53E-03	2000,0	0,32
0,20	0,10	Ellipsoidal	1,00E+06	1000	3000	32,5	7,34E-03	3000,2	0,47
0,20	0,10	Ellipsoidal	1,00E+06	1000	4000	58,0	1,36E-02	4000,4	0,63
0,20	0,10	Ellipsoidal	1,00E+06	1000	5000	87,0	2,10E-02	5000,8	0,79
0,20	0,05	Ellipsoidal	1,00E+05	100	1000	48,8	4,07E-02	1001,2	1,58
0,20	0,05	Ellipsoidal	1,00E+05	100	2000	109,2	1,11E-01	2003,0	3,17
0,20	0,05	Ellipsoidal	1,00E+05	100	3000	170,2	1,92E-01	3004,8	4,75
0,20	0,05	Ellipsoidal	1,00E+05	100	4000	231,3	2,79E-01	4006,7	6,34
0,20	0,05	Ellipsoidal	1,00E+05	100	5000	292,5	3,70E-01	5008,5	7,92
0,20	0,05	Ellipsoidal	5,00E+05	500	1000	5,2	2,36E-03	1000,0	0,32
0,20	0,05	Ellipsoidal	5,00E+05	500	2000	22,8	1,30E-02	2000,1	0,63
0,20	0,05	Ellipsoidal	5,00E+05	500	3000	45,2	2,83E-02	3000,3	0,95
0,20	0,05	Ellipsoidal	5,00E+05	500	4000	69,1	4,61E-02	4000,6	1,27
0,20	0,05	Ellipsoidal	5,00E+05	500	5000	93,1	6,54E-02	5000,9	1,58
0,20	0,05	Ellipsoidal	1,00E+06	1000	1000	1,0	2,11E-04	1000,0	0,16
0,20	0,05	Ellipsoidal	1,00E+06	1000	2000	5,6	2,52E-03	2000,0	0,32
0,20	0,05	Ellipsoidal	1,00E+06	1000	3000	14,3	7,54E-03	3000,0	0,47

0,20	0,05	Ellipsoidal	1,00E+06	1000	4000	25,2	1,43E-02	4000,1	0,63
0,20	0,05	Ellipsoidal	1,00E+06	1000	5000	37,5	2,23E-02	5000,1	0,79
1,00	1,00	Circular	1,00E+05	100	1000	12,0	6,01E-04	1000,1	0,32
1,00	1,00	Circular	1,00E+05	100	2000	36,7	2,95E-03	2000,3	0,63
1,00	1,00	Circular	1,00E+05	100	3000	74,9	7,02E-03	3000,9	0,95
1,00	1,00	Circular	1,00E+05	100	4000	123,4	1,24E-02	4001,9	1,27
1,00	1,00	Circular	1,00E+05	100	5000	179,0	1,90E-02	5003,2	1,58
1,00	1,00	Circular	5,00E+05	500	1000	3,0	1,64E-05	1000,0	0,06
1,00	1,00	Circular	5,00E+05	500	2000	6,5	2,96E-04	2000,0	0,13
1,00	1,00	Circular	5,00E+05	500	3000	12,4	6,48E-04	3000,0	0,19
1,00	1,00	Circular	5,00E+05	500	4000	20,8	1,46E-03	4000,1	0,25
1,00	1,00	Circular	5,00E+05	500	5000	32,0	2,54E-03	5000,1	0,32
1,00	1,00	Circular	1,00E+06	1000	1000	1,7	9,72E-06	1000,0	0,03
1,00	1,00	Circular	1,00E+06	1000	2000	3,3	1,97E-05	2000,0	0,06
1,00	1,00	Circular	1,00E+06	1000	3000	5,2	6,01E-05	3000,0	0,09
1,00	1,00	Circular	1,00E+06	1000	4000	7,8	2,48E-04	4000,0	0,13
1,00	1,00	Circular	1,00E+06	1000	5000	11,5	5,77E-04	5000,0	0,16
1,00	0,50	Ellipsoidal	1,00E+05	100	1000	10,5	1,09E-03	1000,1	0,32
1,00	0,50	Ellipsoidal	1,00E+05	100	2000	33,3	5,40E-03	2000,3	0,63
1,00	0,50	Ellipsoidal	1,00E+05	100	3000	66,9	1,27E-02	3000,7	0,95
1,00	0,50	Ellipsoidal	1,00E+05	100	4000	108,0	2,21E-02	4001,5	1,27
1,00	0,50	Ellipsoidal	1,00E+05	100	5000	154,0	3,32E-02	5002,4	1,58
1,00	0,50	Ellipsoidal	5,00E+05	500	1000	2,3	1,33E-05	1000,0	0,06
1,00	0,50	Ellipsoidal	5,00E+05	500	2000	5,3	3,90E-04	2000,0	0,13
1,00	0,50	Ellipsoidal	5,00E+05	500	3000	9,4	8,71E-04	3000,0	0,19
1,00	0,50	Ellipsoidal	5,00E+05	500	4000	15,3	2,00E-03	4000,0	0,25
1,00	0,50	Ellipsoidal	5,00E+05	500	5000	23,6	3,67E-03	5000,1	0,32
1,00	0,50	Ellipsoidal	5,00E+05	500	1000	4,4	1,38E-05	1000,0	0,06
1,00	0,50	Ellipsoidal	5,00E+05	500	2000	9,8	3,90E-04	2000,0	0,13
1,00	0,50	Ellipsoidal	5,00E+05	500	3000	17,2	8,68E-04	3000,0	0,19
1,00	0,50	Ellipsoidal	5,00E+05	500	4000	27,9	1,99E-03	4000,1	0,25
1,00	0,50	Ellipsoidal	5,00E+05	500	5000	43,0	3,65E-03	5000,2	0,32